Examining Middle-ear and Tectorial Membrane Mechanics using Computational Models

A Dissertation

Presented to

The Academic Faculty

by

Charlsie Lemons

In Partial Fulfillment

of the Requirements for the Degree

Doctor of Philosophy in the

George W. Woodruff School of Mechanical Engineering

Georgia Institute of Technology

May, 2019

Examining Middle-ear and Tectorial Membrane Mechanics using Computational Models

Approved by:

Dr. Julien Meaud
Advisor, Committee Chair
School of Mechanical Engineering
Georgia Institute of Technology

Dr. Kenneth Cunefare
School of Mechanical Engineering
Georgia Institute of Technology

Dr. Alper Erturk
School of Mechanical Engineering
Georgia Institute of Technology

Dr. Karim Sabra
School of Mechanical Engineering
Georgia Institute of Technology

Dr. Wei Sun
Department of Biomedical Engineering
Georgia Institute of Technology

Date Approved: November 30^{th}, 2018

Acknowledgements

First and foremost, I want to wholeheartedly thank my advisor, Dr. Julien Meaud. It has been an honor and an absolute pleasure to be the first PhD student in his lab. Under his guidance, my ability to clearly define a scientific problem, plainly motivate why we care about solving the problem, and outline a path to solving said problem has improved remarkably over the course of my PhD. As a result, I've grown tremendously as a researcher and as an engineer. His patience, enthusiasm, and ability to put forth critique of ideas both kindly and logically are inspiring. Being a part of his lab has genuinely has been an immensely positive experience. I'd also like to thank the rest of my committee (Karim Sabra, Ken Cunefare, Alper Erturk, and Wei Sun). I'm especially grateful for the guidance of Dr. Cunefare. Meeting with him pushed me to re-evaluate how I approached my work which lead to a more scientifically rigorous study.

Next, I'd like to thank the rest of the Meaud group, particularly the current members: Kaikai Che, Thomas Bowling, and Haiqi Wen. The group always asked insightful questions during meetings which pushed me to become a better researcher. It's been a great experience to work with such a hardworking, kind, and intelligent group of individuals. I'd also like to thank Elisa Boatti (a former Postdoc): her help was invaluable in my study on tectorial membrane mechanics.

I'm grateful to my parents who've provided an abundance of love, encouragement, and motivation. They've been unbelievably supportive throughout my entire academic career and for that, I cannot thank them enough. I'd like to dedicate this thesis to the memory of my grandfathers, Wayne Shelton and Charles Lemons. I would not be where I am today without them; both were inspiring, humble, intelligent, and kind men who I will always greatly admire.

Lastly, I would like to thank my best friend and wife, Kira. Kira has provided unconditional love, support, and humor throughout my entire grad school career. She believed in me even when I absolutely did not and has pushed me to be a better, more confident, and more loving person. It's been an amazing journey.

Table of Contents

List of Tables

List of Figures

Summary

The ear acts as a sensitive broadband receiver which transduces sound waves in the ear canal into electrical signals sent to the nervous system. Each of the many small components which comprise the ear are mechanically fine-tuned to detect faint sound throughout a wide range of frequencies. By studying the mechanics of different components of the ear, the mechanisms which allow for such remarkable abilities can be better understood. In this thesis, the mechanics of components of the ears of several species are investigated: specifically, the mouse tectorial membrane (an extracellular matrix located in the inner ear), the chinchilla middle ear, and the bullfrog eardrum are studied. Previous experimental studies have revealed interesting phenomena in these components; this study aims to use computational models to clarify key aspects of the mechanics of these components.

This thesis aims to characterize, for the first time, the anisotropic material properties of the tectorial membranes of wild-type and genetically modified mice at audio frequencies. Additionally, a circuit model of the chinchilla middle ear, absent in literature prior to this study, was developed. Using this model, this thesis aims to evaluate the influence of stiffness, damping, and inertial properties on middle-ear transmission characteristics. Lastly, in this thesis, a mechanical basis for the long group delay observed through the bullfrog eardrum is proposed.

Chapter 1

Introduction

1.1 Introduction to hearing mechanics

The mammalian ear acts as a sensitive, broadband receiver: the human ear, for example, can detect frequencies from approximately 20 Hz to 20 kHz; at 1 kHz, sounds that displace the eardrum one tenth the size of hydrogen molecule can be detected[19]. Together, the nervous system and the mammalian ear act as a frequency analyzer of impressive selectivity[19]. By studying the mechanics of different components of the ear, the mechanisms which allow for such remarkable abilities can be better understood and the treatment and prevention of hearing loss can be improved. The components of the ear examined in this thesis are the mouse tectorial membrane (a component of the inner ear), the chinchilla middle ear, and the bullfrog eardrum.

The mammalian ear is a complex, finely tuned structure which transforms sound in the ear canal into electrical signals sent to the brain. A schematic representation of the mammalian ear is given in Figure 1.1A. In normal hearing, the pinna of the outer ear (labeled in Figure 1.1A) acts a horn collecting sound into the ear canal[19]. As seen in Figure 1.1A, at the end of the ear canal lies the eardrum. Once the sound wave is transformed into mechanical vibration by the eardrum, it is passed on to the ossicular chain through the manubrium of the malleus.

The ossicular chain is connected to the inner ear at the stapes footplate (the footplate of the smallest ossicle, the stapes). The stapes pushes the water-like fluid of the cochlea (located in the inner ear) back and forth. As detailed in Figure 1.1A-B, the cochlea can be described as a series of three ducts, the scala vestibuli, the scala media, and the scala tympani, which are wound into a snail shape. A schematic of a cross-section of the cochlea is given on Figure 1.1B where each of these three ducts are labeled. Vibration of the fluid within the top duct, the scala vestibuli, due to vibration of the stapes footplate causes a pressure difference between the top two ducts (the scala

vesibuli and the scala media) and the bottom duct (the scala tympanic) which in turn, causes the structure separating these ducts, the organ of Corti, to move. The organ of Corti is boxed in red on Figure 1.1B (and shown in more detail in the following chapter on Figure 2.1). Within the organ of Corti are mechanosensory receptors, the inner and outer hair cells. Deflection of these hair cells, caused by relative motion between the basilar and tympanic membranes, opens mechanically gated ion channels which begins the process of sensory transduction and amplification.

1.2 Thesis Overview and Outline

In this thesis, the mechanics of the mouse tectorial membrane, the chinchilla middle ear, and the bullfrog eardrum are investigated in order to better understand each component's role in hearing function. A separate study was conducted for each of these components and each study is detailed in its own chapter. The first study of this thesis, discussed in Chapter 2, aims to characterize the anisotropic material properties of the tectorial membrane of wild-type and genetically modified mice at audio frequencies. Chapter 3 aims to evaluate the influence of inertial, stiffness, and damping properties on the middle ear's ability to transmit of sound. Lastly, in Chapter 4, this thesis proposes a mechanical basis for the long group delay observed through the bullfrog eardrum.

The tectorial membrane (TM) is an extracellular matrix which is directly coupled with the mechanoelectrical receptors responsible for sensory transduction and amplification. As such, the TM is often hypothesized to play a key role in the remarkable sensory abilities of the mammalian cochlea. Genetic studies targeting TM proteins have shown that changes in TM structure dramatically affect cochlear function in mice[20,21]. Precise information about the mechanical properties of the TMs of wild-type and mutant mice at audio frequencies is required to elucidate the role of the TM and to understand how these genetic mutations affect cochlear mechanics. This study aims to determine, for the first time, the anisotropic, viscoelastic material properties of wild-type and transgenic mice within the auditory frequency range and to draw conclusions about how these mutations affect cochlear physiology. To do so, an automated inverse-fitting algorithm was used to find the material properties of finite element models which best capture experimental data provided by our collaborators.

The mammalian middle ear is responsible for the efficient transmission of sound from the ear

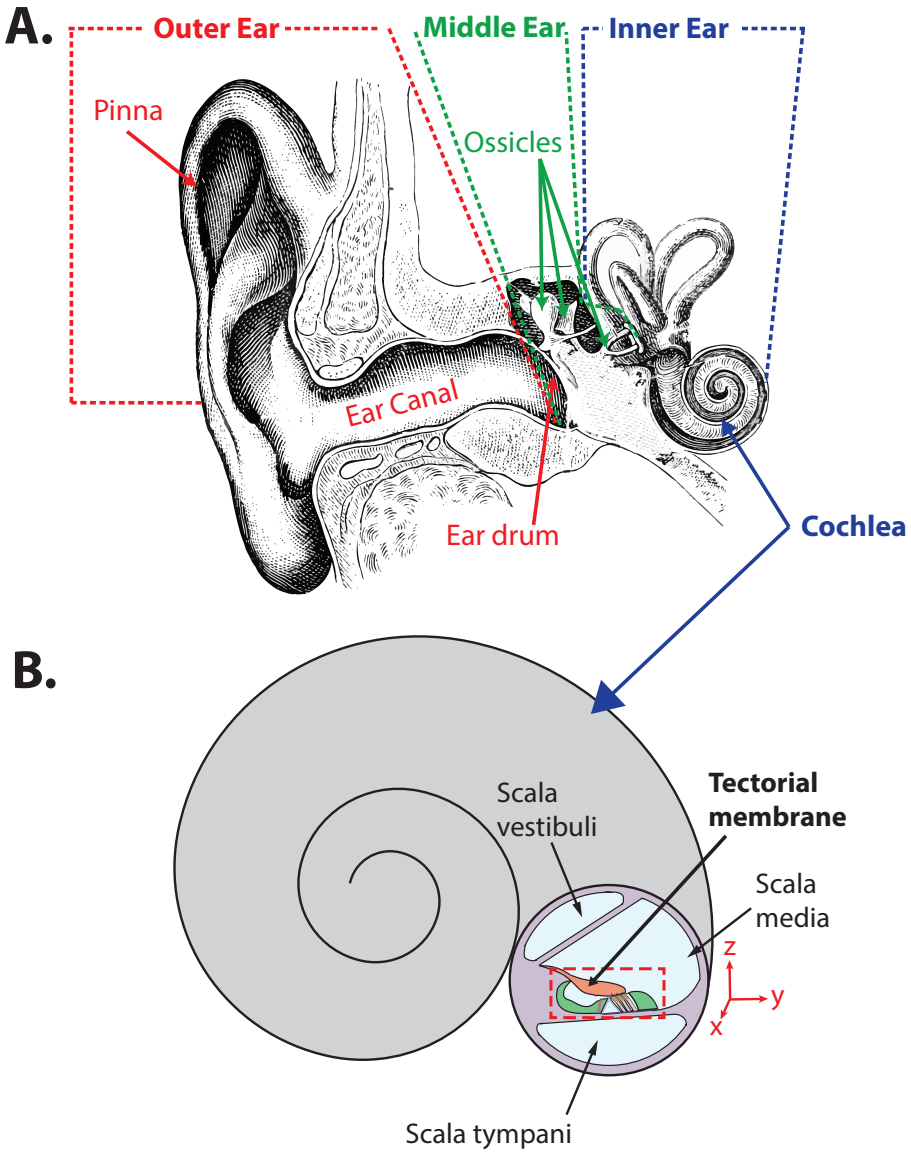

FIGURE 1.1. A. Diagram of the mammalian ear edited from public domain image[2]. In this dissertation, the mammalian middle ear (outlined in green) and tectorial membrane, a component of the inner ear (the inner ear is outlined in blue) are studied. In addition, the bullfrog eardrum is examined, discussed in further detail in later sections. B. Cross-section of the cochlea, a component of the inner ear. The location of the tectorial membrane (TM) within the scala media (which lies between the scala vestibuli and scala tympani) is indicated with red, dashed box (details of the area within the red box are given in Figure 2.1).

canal into the inner ear through a broad range of frequencies. As such, understanding middle-ear transmission characteristics is essential in the study of hearing mechanics. A circuit model of the chinchilla middle ear, absent in literature prior to this study, was developed. Using this model, Chapter 3 aims to evaluate the influence of stiffness, damping, and inertial properties on its

transmission characteristics.

In the aforementioned mammalian middle-ear analysis, the eardrum was found to play a large role in group delay through the middle ear at high frequencies. The eardrum's role in the group delay through the middle ear has been observed to be even more dramatic in the American bullfrog[22,23]. While the surface area of these eardrums is similar to that of humans or cats[17,18,8], the group delay through the bullfrog eardrum is nearly an order of magnitude larger, even when unattached to the rest of the middle ear[23]. A slow, inward traveling wave on the eardrum has been observed on the bullfrog eardrum and has been hypothesized to be the source of this large group delay[23]. However, the underlying mechanics behind this slow, inward traveling wave are not understood and thus, the source of the group delay through the bullfrog eardrum remains unclear. Chapter 4 aims to elucidate the mechanics which make possible the slow, inward traveling wave seen on these eardrums. To do so, the bullfrog eardrum is modeled as a viscoelastic circular membrane with spatially varying thickness.

Chapter 2

Characterizing the anisotropic, viscoelastic material properties of the tectorial membranes of wild-type and $Tectb^{-/-}$ mice

2.1 Chapter overview

In the work presented here, I aim to (1) characterize the anisotropic, viscoelastic material properties of WT TMs at audio frequencies and (2) provide a quantitative understanding of how, precisely, the $Tectb^{-/-}$ mutation (a genetic mutation known to alter the microstructure of the TM) affects the anisotropic material properties of the TM. To do so, an inverse fitting algorithm was implemented to find to material parameters of finite element models of isolated TM segments which best capture the displacement of the TMs measured by our collaborators, Dr. Dennis Freeman's group at MIT. The accuracy and precision of this fitting methodology was characterized to ensure differences seen in material properties between WT and $Tectb^{-/-}$ TMs are due to actual changes in the material properties rather than an artifact of the imprecision or inaccuracy of the algorithm. The statistical significance of the observed changes in the material properties due to the $Tectb^{-/-}$ mutation was evaluated. Additionally, the effects of changes in the TM's material properties on TM motion are analyzed in order to better understand how these changes might affect the role of the TM in vivo.

2.2 Introduction to tectorial membrane mechanics

2.2.1 The role of the tectorial membrane

The mammalian ear's remarkable ability to detect faint sound throughout a wide range of frequencies is largely due to the sensory abilities of the cochlea. Within the cochlea, traveling waves propagate along the basilar membrane (BM)[24]: relative motion between the BM and tectorial membrane causes deflection of the hair bundles attached to the mechanosensory receptors, the inner and outer

hair cells, labeled in Figure 2.1. Both the inner and outer hair cells transduce mechanical energy into electrical signals[25]. The inner hair cells transform mechanical energy into electrical signals which are relayed via the auditory nerve while the outer hair cells are responsible for the amplification of low-level sound that enters the cochlea.

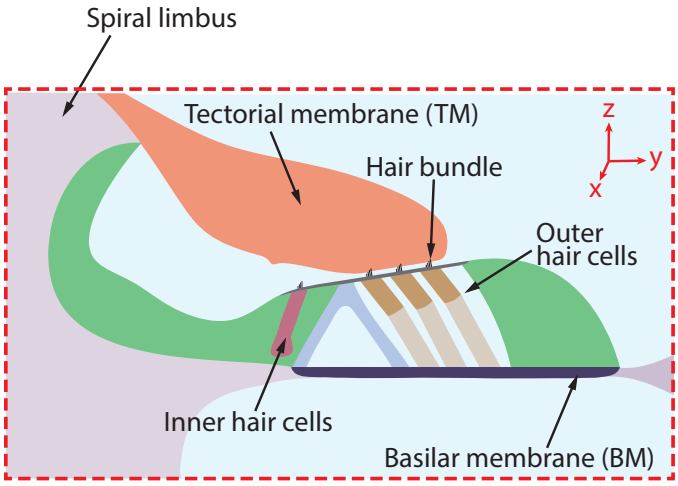

FIGURE 2.1. A schematic of the organ of Corti (the portion of the cochlea boxed in red on Figure 1.1A). The TM, which is attached to the spiral limbus, lies above hair bundles attached to the inner and outer hair cells. Relative motion between the TM and the BM causes deflection of the hair bundles.

As seen in Figure 2.1, the TM overlies the hair bundles attached to the inner and outer hair cells. This strategic anatomic configuration of the TM relative to the hair bundles suggests that the TM plays a key role in cochlear function. Studies working towards the characterization of cochlear physiology in transgenic mice have demonstrated that mutations of the genes that encode TM proteins affect key characteristics of cochlear function, such as the sensitivity and tuning of the BM[26,21] or cochlear stability (some mutant mice emit more spontaneous otoacoustic emissions than wild-type mice[27,28]). Furthermore, recent in vivo measurements of traveling waves on the TM and BM have shown that the TM has a larger dynamic range, has a sharper frequency selectivity, and is tuned to a slightly higher frequency than the BM[29]: these measurements by Lee et al. support the concept that micromechanical interactions within the organ of Corti modulate the stimulus to the inner hair cells and affect the neural code of hearing. Disruption of non-collagenous proteins within the TM due to genetic mutation is a known cause of hereditary hearing loss in humans[30]: thus, characterizing precisely how these genetic mutations affect TM mechanics, and thereby cochlear function, is a crucial step in better understanding human deafness.

2.2.2 Previous measurements of TM mechanical properties

The TM is a soft, gel-like extracellular matrix[31,32,33] containing two groups of components: collagen fibrils and non-collagenous proteins. Collagen fibrils are organized in thick, nearly radially-oriented fibers[34]. The non-collagenous proteins compose a striated-sheet matrix (SSM) surrounding the collagen fibers[35,36,21]. The SSM is composed of several different proteins, including β-tectorin (TECTB)[21], which are structural macromolecules that are thought to contribute to the elastic properties of the TM[3,4]. Due to the presence of collagen fibers, the TM is highly anisotropic: most studies have found that the TM is stiffer in the radial direction than in the longitudinal direction[37,38,39,40] (one study, Ref. 41, found the opposite). Most[38,39,41] reports of anisotropic material properties have been static or quasi-static measurements. However, the TM is highly viscoelastic[42,4,43,3,40,37] and as such, its mechanical properties vary significantly with frequency. Thus, static measurements are limited in their ability to provide information about the role of the TM in hearing mechanics where properties at auditory frequencies are needed. Studies where dynamic anisotropic mechanical properties[40,37] have been reported do not provide the anisotropic material properties of the TM; rather, shear impedance measurements of the TM in the radial and longitudinal directions are given.

In an effort to characterize the dynamic mechanical properties of the TM, Refs. 42, 4, 43, 3 measured the radial displacement of isolated TM segments in response to a harmonic, radial stimulus (as on Figure 2.2A). In all studies, longitudinal propagation of radial motion (where the longitudinal direction is defined as x and the radial direction is defined as y on Figures 1.1B, 2.1, and 2.2B) were observed on the TMs: these measurements were used to extract the viscoelastic mechanical properties of TMs of wild-type (WT) and mutant mice at audio frequencies. To do so, traveling, exponentially decaying waves were fit to the measured displacements. By assuming that the motion of the TM could be described as a shear wave, i.e. that the TM only moves in the radial direction, Refs. 42, 4, 43, 3 were able to analytically relate the wave speeds and space constants of the fit waveforms to the shear modulus and shear viscosity of the TMs.

For these isolated TM segments to move as a shear wave, the width of the TM (its y-direction dimension) must be very large relative to the wavelength. If the TM's width were very small, for example, the TM's motion would be better described as a flexural wave propagating on a viscoelastic

beam. Since the reported wavelengths for these longitudinally propagating shear waves (between 305-360μm for WT TMs at 20kHz[3]) are on the order of the width of the isolated TM segments (which are $\approx 150\mu$m wide), the validity of the assumption that the TM is moving purely in shear is questionable. In the experimental data provided by our collaborators, significant motion in the longitudinal direction due to a harmonic radial input is measured, further demonstrating that this assumption does not adequately describe the motion of the TM. Because the motion becomes much more difficult to model analytically for intermediate widths, particularly for anisotropic structures, a finite element-based approach which takes into consideration the known anisotropy and finite dimensions of the TM is used here to determine the anisotropic, viscoelastic material properties of the TMs of WT and $Tectb^{-/-}$ mutant mice at audio frequencies.

2.2.3 Known properties of $Tectb^{-/-}$ TMs

$Tectb^{-/-}$ mice are transgenic mice that lack functional β-tectorin. In these mice, a complete loss of the striated sheet matrix has been reported[21]. While the $Tectb^{-/-}$ mutation does not directly affect the hair bundles or TM's attachments to the hair bundles or limbal edge, the BM tuning is sharpened by a factor of 2-3 at high frequencies in these mice[21]. In addition, at low frequencies, the BM is about 10 dB less sensitive in these mice than in WT mice[21]. $Tectb^{-/-}$ mutants display slightly greater numbers of spontaneous otoacoustic emissions than in WT mice; these emissions also tend to be at a higher frequency than observed in WT mice[28].

Previous studies have estimated the complex shear modulus of WT and $Tectb^{-/-}$ TMs at audio frequencies[3,4]. In these studies, the shear stiffness of $Tectb^{-/-}$ mice was found to be significantly smaller than the shear stiffness in WT mice. The source of the sharper tuning in these mice has been attributed to weaker coupling of individual cross-sections of the TM in the longitudinal direction reported in these mice[3,44]. Reduced longitudinal coupling could reduce the ability of waves to travel along the TM such that a smaller area of the cochlea (the portion tuned to the input frequency) would be excited in response to an input. However, the anisotropic elastic properties of the TM have not been reported at audio frequencies: as shown in this study, the TM's anisotropic properties greatly affect its motion. Thus, understanding the effect of the $Tectb^{-/-}$ mutation on the TM's anisotropic material properties could help to elucidate the underlying mechanics behind the combined sharper tuning and decreased sensitivity reported in these mice.

2.3 Fitting methodology: overview and implementation

2.3.1 Experimental Methodology of Collaborators

All experiments were conducted by Jonathan B. Sellon and Dennis M. Freeman at MIT. The Optical System Motion analysis was conducted by Jonathan B Sellon, Daniel Filizzola, and Dennis M. Freeman. While the experiments themselves are not my work, it is necessary to explain how the experimental data was obtained in order to best understand the rest of my work outlined in this chapter.

Briefly, the cochleae from five adult $Tectb^{-/-}$ mice and six WT mice were excised using a previously published surgical technique[45]. Basal region TM segments were then suspended between vibrating and stationary supports of a previously published wave chamber device[43], as seen on Figure 2.2A. This device consisted of a vibrating support attached to a piezoelectric actuator (Thorlabs) that delivered oscillatory motions at audio frequencies (10-20 kHz). The stationary support was attached to the underlying glass slide and both supports were coated with $2\mu L$ of tissue adhesive (Cell-Tak) and surrounded with artificial endolymph. The TM was placed into the artificial endolymph bath and attached to the surfaces of the supports.

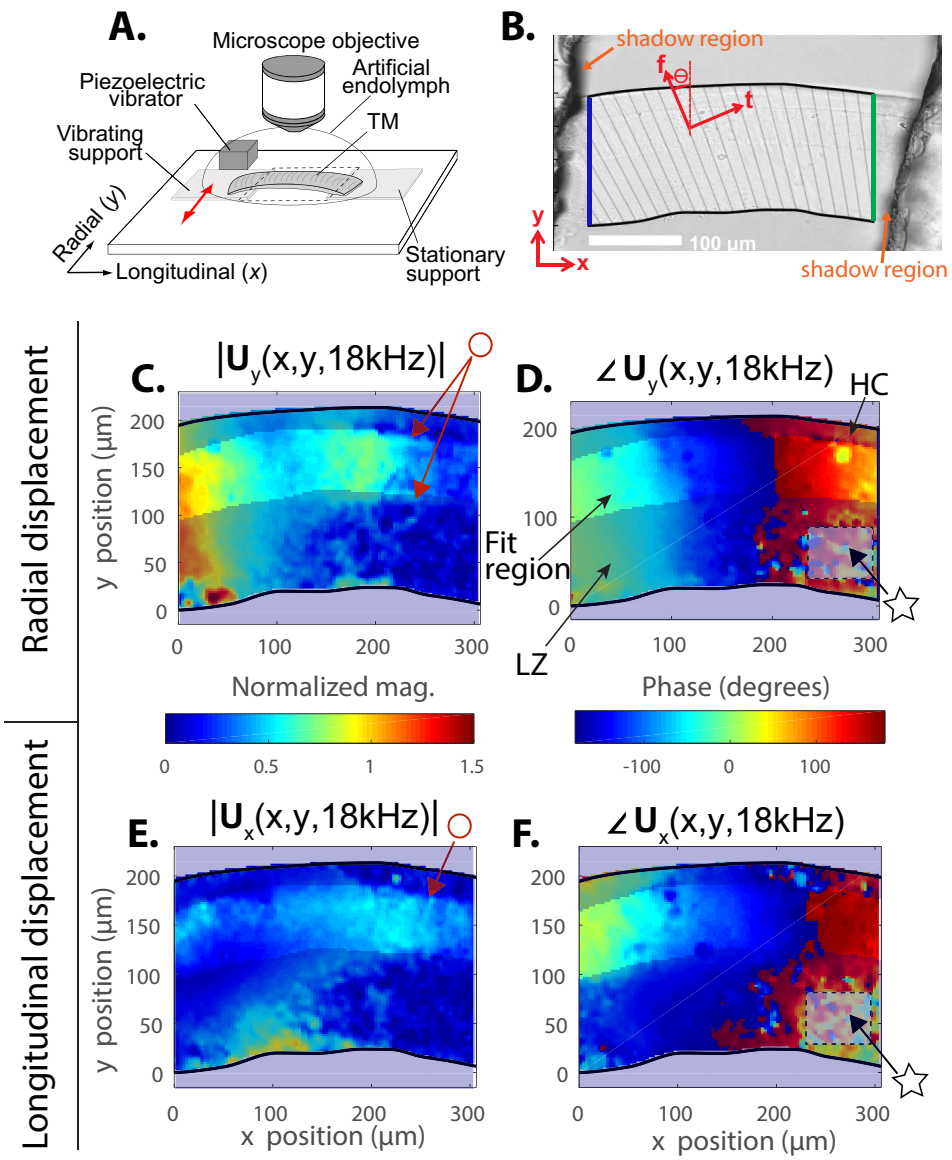

FIGURE 2.2. A. Schematic of experimental set-up. B. Obtaining TM geometry from a snapshot from the experiment. Orientation of collagen fibers is marked in gray: fiber and transverse directions are labeled in red (where $\theta = 15°$). The left and right edges of the model are marked in blue and green, respectively C-E. Magnitude (C, E) and phase (D, F) of experimentally measured radial (C-D) and longitudinal (E-F) motion of one WT TM, WT1, at 18 kHz. The brighter, unshaded region marked in C-E is the region over which the TM models were fit. The upper shaded portion of the TM, labeled HC on panel D, is the hair cell region. The lower portion of the shaded region of the TM, labeled LZ on panel D, is the limbal zone. The arrows labeled with red circles on C and E point to regions on this TM where an unrealistic discontinuity is seen in the data. The boxed regions labeled with stars on D and F highlight regions where noise is clearly visible in the experimental data. The magnitudes in panels A and E are normalized by the average U_y value along the left edge of the TM at 18kHz.

TM motions were generated by stimulating the piezoelectric actuator of the vibrating support and were captured using a computer vision system. The computer vision system is discussed in Ref. 46 and Refs. 43, 3. The steady-state displacement at each point on the TM and at each frequency can be written as,

$$\vec{\mathbf{u}}(x,y,t) = \mathbf{u}_x(x,y,t)\vec{i} + \mathbf{u}_y(x,y,t)\vec{j} \tag{2.1}$$

where a bolded character indicates a complex value, $\vec{i}$ indicates a unit vector in the longitudinal direction, x, $\vec{j}$ indicates a unit vector in the radial direction, y, and $\mathbf{u}_y(x,y,t)$ and $\mathbf{u}_x(x,y,t)$ are the radial and longitudinal displacements, respectively. $\mathbf{u}_x(x,y,t)$ can be written in the following forms:

$$\begin{aligned}
\mathbf{u}_x(x,y,t) &= \mathbf{U}_x(x,y,\omega)e^{i\omega t} \\
&= \left[\Re\left(\mathbf{U}_x(x,y,\omega)\right) + i\Im\left(\mathbf{U}_x(x,y,\omega)\right)\right] e^{i\omega t} \\
&= \left|\mathbf{U}_x(x,y,\omega)\right| e^{i(\omega t + \angle \mathbf{U}_x(x,y,\omega))}
\end{aligned} \tag{2.2}$$

where $\mathbf{U}_x(x,y,\omega)$ is the complex amplitude of the longitudinal displacement, ω is the forcing frequency, $\Re(\bullet)$ and $\Im(\bullet)$ refer to the real and imaginary parts, respectively, $|\bullet|$ indicates the amplitude, and $\angle(\bullet)$ indicates the phase angle. $\mathbf{u}_y(x,y,t)$ can be written using similar expressions.

Our collaborators provided $\mathbf{u}_x(x,y,\omega)$ and $\mathbf{u}_y(x,y,\omega)$ for several WT and mutant TMs: an example of $\mathbf{U}_x(x,y,\omega)$ and $\mathbf{U}_y(x,y,\omega)$ for one WT TM, WT1, at 18kHz is given in Figures 2.2C-F. I use this data in order to find the anisotropic material properties of the TMs of these mice based on the approach detailed in the remainder of this section.

2.3.2 Modeling Isolated TM Segments

In order to characterize the anisotropic, viscoelastic material properties of WT and $Tectb^{-/-}$ mice, I implemented an inverse fitting method to find the material properties which best capture the experimentally captured motion of the isolated TM segments provided by our collaborators. To do so, a finite element model of each TM used in the study was built using Abaqus[47], a commercial software suite for finite element analysis. In these models, the geometry of each TM was taken

directly from snapshots of the TM in the experiments, as marked by a black outline in Figure 2.2B. Since data near the supports tends tends to be noisy, the locations of the left and right edges of the model (marked in blue and green in Figure 2.2B, respectively) were chosen such that they provide the largest area of the TM possible without falling within a zone on the TM snapshot, labeled "shadow region" on Figure 2.2B, where the TM is not clearly visible.

A steady-state direct dynamics simulation was run for each discrete frequency (between 10-20kHz) of the experimental data. The real and imaginary parts of the experimentally measured x and y displacement were input as boundary conditions at the left and right edges of the model. It should be noted that the length of each TM extends beyond what is seen in the experimental data or in the snapshot on Figure 2.2B and the exact amount that the TM extends beyond the boundary is unknown: hence, the displacement is directly input at each edge of the model instead of idealizing the left edge as a pure radial input and the right edge as perfectly fixed.

Since the out-of-plane (z) dimension of the TM is quite small ($\approx 22\mu$m[21]) relative to the x and y dimensions ($\approx 300-400\mu$m long and $\approx 200\mu$m wide), the TM was assumed to be in plane stress. To limit the number of free parameters, the TM was modeled as homogeneous. In addition, since the TM is mostly composed of water, the TM was modeled as incompressible. Due to the presence of collagen fibers which lie nearly in the radial direction[38], a transversely isotropic, viscoelastic material model was used where, as shown in Figure2.2B, the fiber direction was oriented 15° from the radial axis (based on previous measurements of fiber orientation[48]). A standard linear solid viscoelastic model[49] was used to model the viscoelastic behavior in the transverse direction and in shear. Thus the complex Young's modulus in the transverse direction, $\mathbf{E}_t$, and the complex in-plane shear modulus, $\mathbf{G}_{tf}$, are written as,

$$\mathbf{E}_t = \frac{E_{t1} i\omega\eta_{t1}}{E_{t1} + i\omega\eta_{t1}} + E_{t0} \quad \text{and} \quad \mathbf{G}_{tf} = \frac{G_{tf1} i\omega\eta_{s1}}{G_{tf1} + i\omega\eta_{s1}} + G_{tf0} \tag{2.3}$$

where E_{t1} and G_{tf1} are the stiffness in the viscoelastic branch for the Young's modulus and shear modulus, respectively. η_{t1} and η_{s1} are the viscosity in the viscoelastic branch for the Young's modulus and shear modulus, respectively. E_{t0} and G_{tf0} are the long term Young's modulus and shear modulus, respectively, and are measures of the static stiffness of a material. The stiffness of the TM in the fiber direction was modeled using a linear elastic and lossless model such that the

Young's modulus in the fiber direction, E_f, is independent of frequency. With the aforementioned assumptions, seven free parameters remain: E_{t1}, E_{t0}, η_{t1}, G_{tf1}, G_{tf0}, η_{s1}, and E_f.

2.3.3 Fitting Methodology Description

The values of the seven free parameters given in the previous subsection were found for each TM sample using an automated fitting algorithm that minimizes the mean error across the frequency range, ϵ_{avg}, defined as,

$$\epsilon_{avg} = \frac{1}{N_f} \sum_{i=1}^{N_f} \epsilon(\omega_i) \tag{2.4}$$

where N_f is the number of discrete frequencies of the available data (between 10-20kHz) and $\epsilon(\omega_i)$ is the error at frequency ω_i. $\epsilon(\omega_i)$ is defined using the following equation:

$$\epsilon(\omega_i) = \frac{\int_S \left\| \vec{\mathbf{U}}_{FEM}(x,y,\omega_i) - \vec{\mathbf{U}}_{data}(x,y,\omega_i) \right\|^2 dS}{\int_S \left\| \vec{\mathbf{U}}_{data}(x,y,\omega_i) \right\|^2 dS} \tag{2.5}$$

where $\vec{\mathbf{U}}_{FEM}(x,y,\omega_i)$ and $\vec{\mathbf{U}}_{data}(x,y,\omega_i)$ are the complex displacement vectors of the TM model and experimental data, respectively.

In the above equations, the error was calculated over an area S where the data appeared to be the most robust. This area S, labeled "fit region" noted on Figure 2.2D (and again in a later section on Figure 2.7G), corresponds to the area defined as the main body of the TM by Ref. 32. The data within the spiral limbus attachment zone (labeled LZ on Figure 2.2D) was noticeably noisy on several of the TMs due to poor reflection in this region. An example of visible noise within this region can be seen in the boxed area marked with a star on Figures 2.2D and F. In the outer hair cell zone, defined by Ref.[32] and labeled as HC on Figure 2.2B, there appeared physically unrealistic discontinuities in the some of the experimental data sets. One example of a physically unreasonable discontinuity seen in the data is marked with a circle on WT1 data seen on Figures 2.2C and E.

The pattern search algorithm, a derivative-free based numerical optimization method[50], was chosen to minimize ϵ_{avg} for each TM. Multiple, random initial guesses were provided to the algorithm: the best fit was chosen to be the solution with the lowest ϵ_{avg} value. The accuracy and precision of the fitting methodology were evaluated, as discussed in the following section.

Previous reports of the dynamic shear moduli[42,4] of the TM do not describe the frequency dependence of the material properties using a standard linear solid viscoelastic model. Instead, values for the shear storage and loss moduli were given at each frequency. Therefore, in order to properly constrain the model and to compare the results found in this study with previous findings, the values of the real parts of Young's moduli in the transverse and fiber directions, $E_t(\omega) = \Re(E_t^*(\omega))$ and E_f, respectively, the real part of the in-plane shear modulus, $G_{tf}(\omega) = \Re(G_{tf}^*(\omega))$, and the loss tangent values in the transverse direction and in shear, $\tan\delta_t(\omega) = \Im(E_t^*(\omega))/\Re(E_t^*(\omega))$ and $\tan\delta_s = \Im(G_{tf}^*(\omega))/\Re(G_{tf}^*(\omega))$, respectively, are reported as a function of frequency. The parameter space was limited by constraints on these values, given in Table A.2 in Appendix A. The parameter constraints were chosen based on previously reported values from[3,4] and physical considerations based on a micro-mechanics model of a fiber-reinforced material (justification for these constraints is discussed in Appendix A).

2.4 Evaluation of the fitting methodology accuracy and precision

For any inverse fitting method, it is important to understand the accuracy and precision of the algorithm so that conclusions can be made about the fit parameter values. In this section, (1) the fitting algorithm's ability to capture the material parameters of a simulated TM and (2) the range of parameters found for solutions with low error are characterized. By characterizing the (1) accuracy and (2) precision of our fitting methodology, conclusions can be made regarding the differences in the material properties of WT and $Tectb^{-/-}$ TMs.

2.4.1 Evaluation of fitting method accuracy

In order to test the accuracy of the fitting method, the fitting methodology as described in the previous sections was implemented using simulated data where the values of the model parameters are known.

Simulated data was obtained using an idealized TM model, detailed in Figure 2.3, Steps 1 and 4. The material of the simulated TM segment was set equal to a similar material as found for WT1: the material parameters for the simulated are plotted with a blue dotted line on Figure 2.4. As seen on Step 1 of Figure 2.3, the right end of the simulated TM segment was held stationary while

the left end was given a radial, harmonic input from 10-20kHz. To mimic the fact that the TM's movement near its left and right edges was not visible in the experimental data, only the motion of the simulated TM from $x_0 = 100\mu$m to $x_{end} = 400\mu$m was recorded, deemed the "visible data," as shown on Figure 2.3, Step 1.

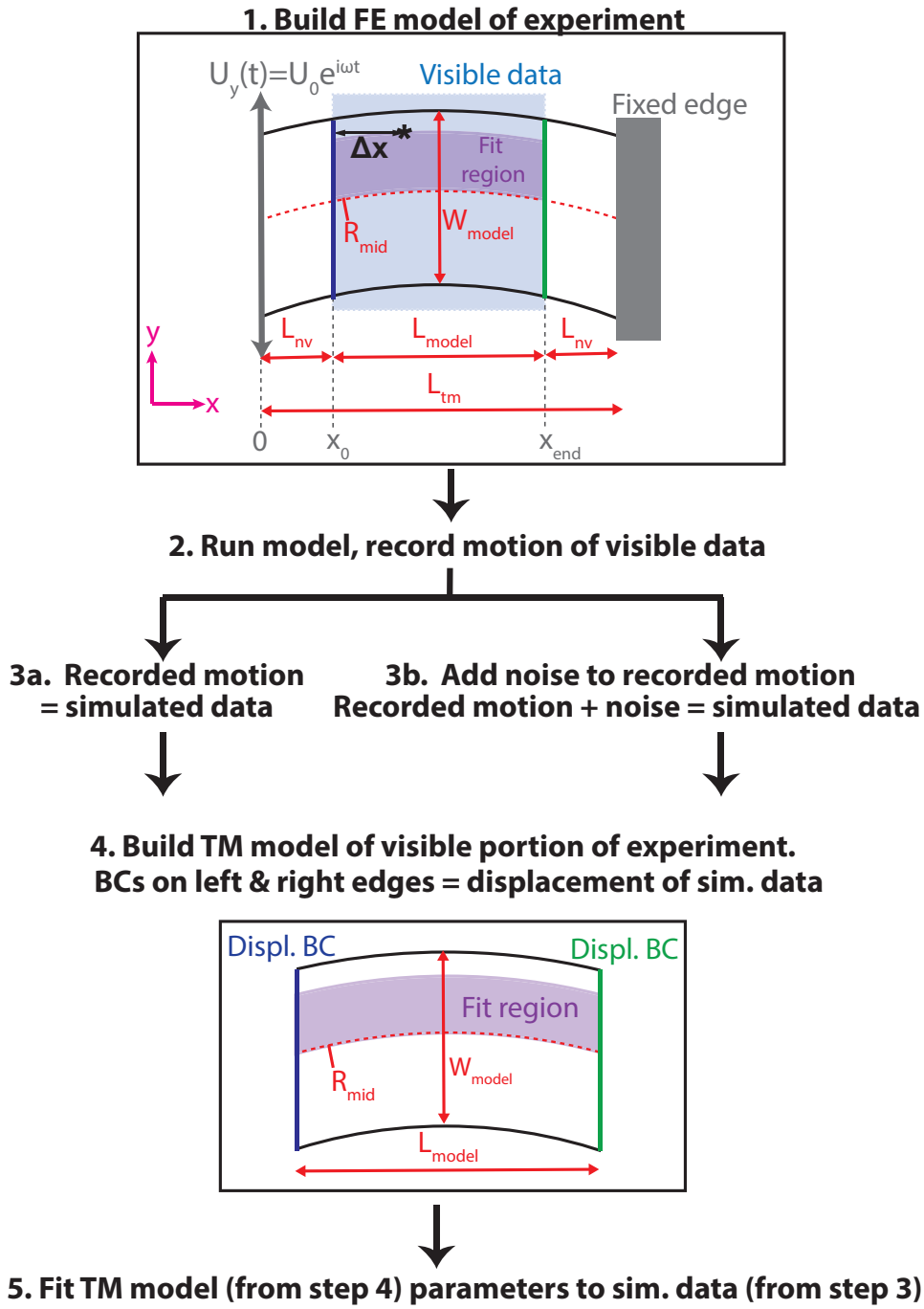

FIGURE 2.3. Steps taken to build simulated data and conduct accuracy study. In Step 1, $L_{tm} = 500\mu$m (where the visible data consists of all TM motion between $x = L_{nv} = 100\mu$m and $x = L_{tm} - L_{nv}$). In Steps 1 and 4, $W_{model} = 173\mu$m (set equal to the width of WT1) and $R_{mid} = 900\mu$m (set equal to the radius of a circle fit to the top of the limbal zone of WT1). In step 4, $L_{model} = 300\mu$m. Note that the model described in Step 1 is used as the finite element model for the parametric study conducted in the main body of the text. The location used to examine the ratio of the longitudinal to radial displacement amplitudes, point P, is marked with a black asterisk in Step 1 where $\Delta x = 100\mu$m.

To understand the effect of noise on the fitting algorithm's ability to find the material parameters of the TM, two different scenarios were tested. In one case, labeled Step 3a in Figure 2.3, the simulated TM's motion over the visible range was used as the simulated data. In the second case, labeled Step 3b in Figure 2.3, normally distributed random values were added to the simulated data from Step 3a such that the signal to noise ratio was similar to that found for the WT1 experimental data (SNR = 14dB). In Step 3b, this combination of the recorded motion plus simulated experimental noise was considered the simulated data.

A TM model with the same width and curvature (R_{mid}) as the simulated TM segment but with length $L_{model} = L_{tm} - 2L_{nv}$ was built, as seen in Figure 2.3, Step 4. On the left and right edges of this model, the displacement from the simulated experiment at x_0 and x_{end} are input as boundary conditions. Step 4 is repeated for the simulated data from Steps 3a (noiseless simulated data) and 3b (noisy simulated data). These models (from Step 4) were fit to data from Steps 3a and 3b using the fitting algorithm discussed in the previous section.

As defined in the previous section, the fitting algorithm minimizes the mean error across the frequency range, ϵ_{avg}, defined in Eq. 2.4; in this study, however, the calculation of $\epsilon(\omega_i)$ is changed such that the simulated data replaced the experimental data,

$$\epsilon(\omega_i) = \frac{\int_S \left\| \vec{\mathbf{U}}_{model}(x,y,\omega_i) - \vec{\mathbf{U}}_{sim}(x,y,\omega_i) \right\|^2 dS}{\int_S \left\| \vec{\mathbf{U}}_{sim}(x,y,\omega_i) \right\|^2 dS} \tag{2.6}$$

where $\vec{\mathbf{U}}_{model}(x,y,\omega)$ is the complex amplitude of the displacement of the TM model (from Step 4) using the material parameters prescribed by the fitting algorithm and $\vec{\mathbf{U}}_{sim}(x,y,\omega)$ is the complex amplitude of the simulated data (from Step 3). For both studies (simulated data with and without noise), 10 random initial guesses were input into the fitting algorithm.

On Figure 2.4, the material parameters of the best fits found with and without noise are plotted against the material parameters of the TM in the simulated experiment. For each parameter P (such as E_t, E_f, etc.), the error between the parameter value obtained for the best fit (the fit with the lowest ϵ_{avg} value), P_{fit}, and the actual parameter of the simulated TM segment, P_{sim}, is calculated as,

$$\mathcal{E}(\omega) = 100 \times \frac{P_{fit}(\omega) - P_{sim}(\omega)}{P_{sim}(\omega)} \tag{2.7}$$

This value is multiplied by 100 in order to give the error as a percent. The maximum values of $\mathcal{E}(\omega)$ found in the study for each material parameter are given in Table 2.1. As seen on Figure 2.4 and Table 2.1, in both the models, the fit properties of the TM model capture the material properties of the simulated TM very well. In both cases, the algorithm overestimates the values of E_f, G_{tf}, and $\tan\delta_t$ and slightly underestimates the values of E_t and $\tan\delta_s$. Excluding E_f, which is overestimated by $\approx 30\%$, the algorithm is able to capture all material parameters within 20% of the their actual values.

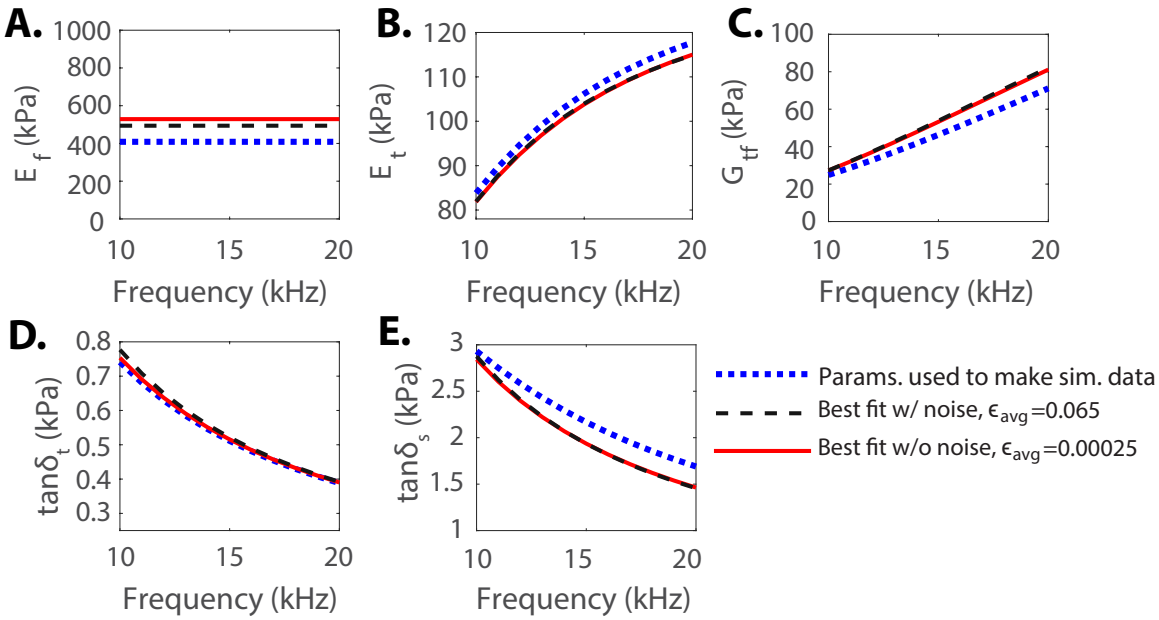

FIGURE 2.4. Comparison of the best fit model parameters (fit to simulated data with and without noise) vs. the actual material parameters of the TM in the simulated experiment. Stiffness properties (E_t, G_{tf}, E_f) are plotted on panels A-C. Damping properties ($\tan\delta_t$ and $\tan\delta_s$) are compared on panels D-E

The main difference between fitting the TM model to simulated data with and without noise is the value of ϵ_{avg}. In the case where the model is fit directly to the recorded motion (no noise is added), $\epsilon_{avg} = 2.5 \times 10^{-4}$. When noise is added to the recorded motion, the error for the best fit TM becomes $\epsilon_{avg} = 0.065$, a 257% increase in ϵ_{avg}. Thus, although noise causes an increase in ϵ_{avg}, it does not appear to inhibit the algorithm's ability to find the material parameters of the TM.

TABLE 2.1. Maximum error between simulated TM material parameters and model best fit parameters, $\mathcal{E}(\omega)$ (defined in Eq. 2.7), found between 10-20kHz. Two studies are compared: in one case, the TM parameters were fit directly to simulated data (no noise was added). In the second case, noise was added to the simulated data such that the signal to noise ratio = 14dB.

	Max. Parameter Error, $\mathcal{E}(\omega)$ (%)	
Parameter	No noise (Step 3a)	With noise (Step 3b)
E_f	+29	+21
E_t	-2.3	-2.4
G_{tf}	+15	+16
$\tan\delta_t$	+1.7	+4.9
$\tan\delta_s$	-13	-14

2.4.2 Evaluation of fitting method precision

In addition to testing the accuracy of the fitting method, the algorithm's ability to find precise results was assessed. If the fitting algorithm is converging towards a single global minimum, little variation is expected among solutions with low error. However, if there are many local minima, large variation in the parameters obtained using fitting algorithm with multiple initial guesses would be expected since many combinations of parameters would produce low error. Occasionally, the fitting algorithm converged to a local minimum with large error relative to the other solutions: these local minima were discarded in the current study by keeping only the solutions with low error defined as,

$$\epsilon_{avg}^{pass} < \epsilon_{avg}^{min} + \Delta\epsilon \tag{2.8}$$

where ϵ_{avg}^{pass} is the average error value for the solution in question, ϵ_{avg}^{min} is the best fit for the TM examined, and $\Delta\epsilon$ is the cutoff criteria, set equal to 0.03. The value of $\Delta\epsilon$ was chosen by examining the results of the initial guesses fit to the simulated data described in the previous subsection: the largest $\Delta\epsilon$ which disallowed solutions that produced a parameter error (excluding E_f) of greater than 50% was chosen.

Two representative examples (one sample for wild-type mice, WT1, and one for $Tectb^{-/-}$ mice, TB1) are plotted in Figure 2.5. For each of these TMs, 20 different, random initial guesses were provided to the fitting algorithm. For WT1, 13 initial guesses produce solutions whose ϵ_{avg} values meet the cutoff criteria; for TB1, 16 trials pass the given criteria. Although there is some variation

in the parameter results found for WT1, no overlap in E_t or G_{tf} is found between these two representative TMs. For all TMs, although not shown here, no overlap for passing solutions is found for E_t and only slight overlap is seen at high frequencies for G_{tf}. Significant overlap in results are found for damping parameters. Although large variation in E_f results are found, all TMs are found to be significantly anisotropic. Since for each TM, solutions with low error are found to have similar parameters, it appears that the algorithm approaches a true global minimum for each TM. Furthermore, since for all solutions with low error, very little or no overlap in E_t and G_{tf} is found between phenotypes, it appears that differences found in stiffness values for each phenotypes are due to significant changes in the material properties resulting from the $Tectb^{-/-}$ mutation, rather than an artifact of the imprecision of the fitting algorithm.

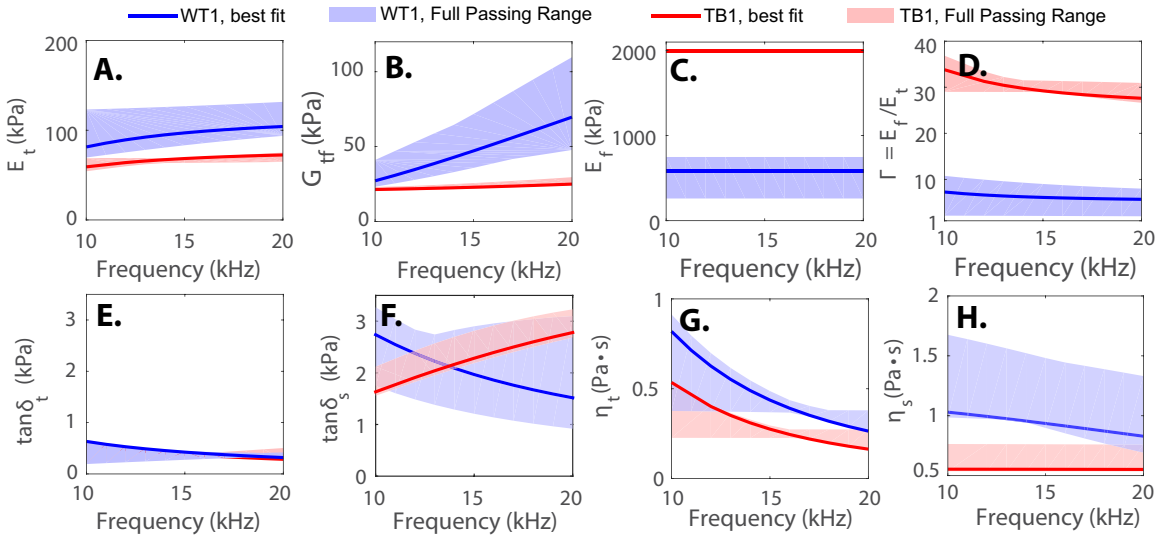

FIGURE 2.5. Range of material properties found for low-error solutions of WT1 and TB1 fits: solutions with error higher than $\epsilon_{avg}^{min} + 0.03$ are eliminated from consideration. 20 initial guesses are input for each phenotype. 13 pass for WT1, 16 pass for TB1. A solid line indicates the solution with ϵ_{avg}^{min}; shading indicates the full range of passing solutions. Stiffness properties (E_t, G_{tf}, E_f, $\Gamma = E_f/E_t$) are plotted on panels A-D. Damping properties ($\tan\delta_t$, $\tan\delta_s$, η_t, η_s) are compared on panels E-H.

2.5 Results

2.5.1 Spatial variation of radial and longitudinal TM motions in WT and $Tectb^{-/-}$ mice

In this subsection, the experimentally captured motion of WT and $Tectb^{-/-}$ mice provided by our collaborators is discussed. While the experiments are not my work, an analysis of the motion is included in order to better understand why my approach to modeling the TMs was necessary. The experimentally captured longitudinal and radial motions over the entire TM area at 18kHz for one TM of each phenotype are shown on Figure 2.6. For each TM, the magnitude of the motion has been normalized by the average magnitude of $\mathbf{U}_y$ along its left edge.

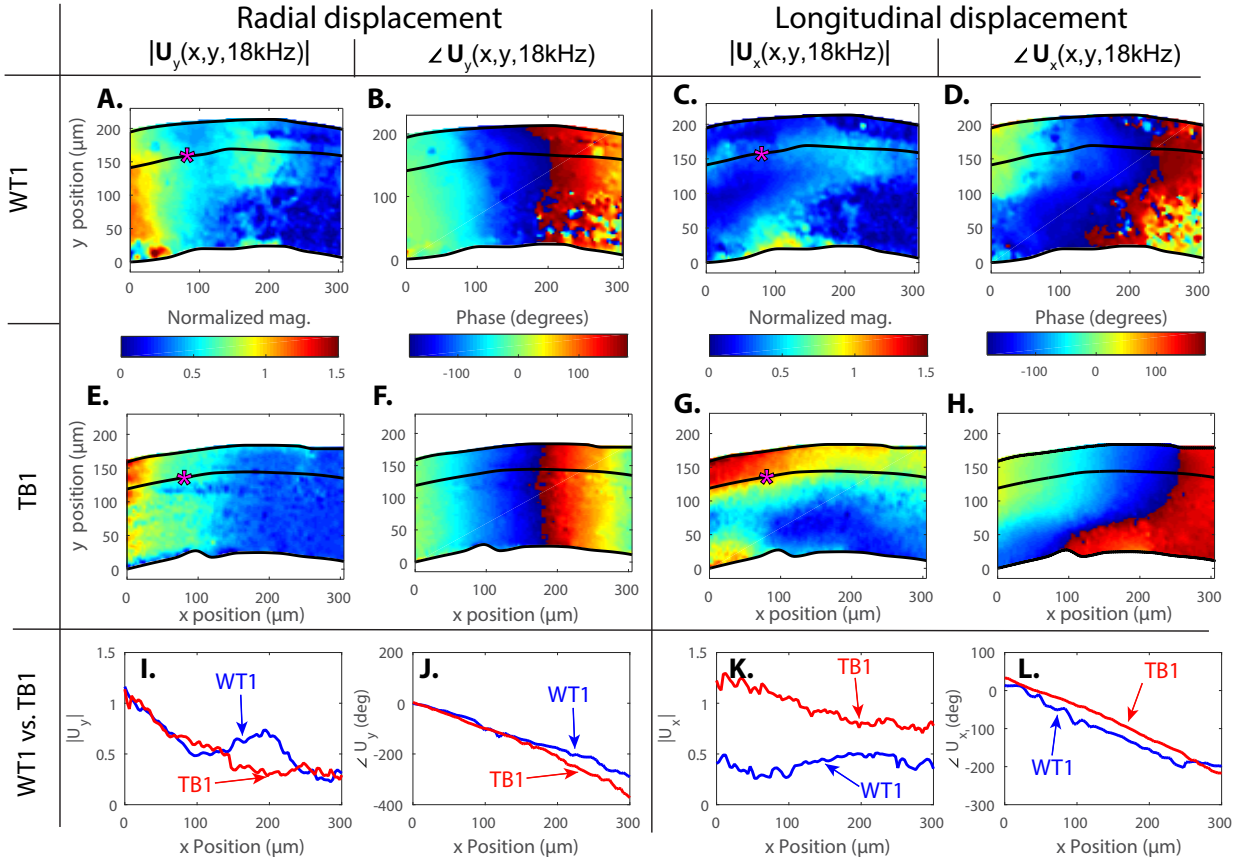

FIGURE 2.6. Experimentally captured motion over TM area for one WT TM (WT1) (A-D) and one $Tectb^{-/-}$ TM (TB1) (E-H). The displacement along one line is plotted in panels I-L. All displacements are normalized to the mean of $|\mathbf{U}_y(0, y, \omega_i)|$. The magenta asterisks on Panels A, C, G, and H indicates the point, P, chosen to examine the ratio of $|\mathbf{U}_x|$ to $|\mathbf{U}_y|$ discussed in the Results section.

For both TMs, $\mathbf{U}_y$ is nearly uniform in the radial direction and can be characterized as a longitudinally propagating plane wave with decaying amplitude. Thus, looking at the radial motion down one line (marked by a solid, black line on panels A-D), plotted on panels E and F, can provide a clearer picture of the wave propagation characteristics, as was done in Refs. 43, 3, 42, 4. Specifically, on Figure 2.6I, it can be seen that the radial motion of the $Tectb^{-/-}$ TM tends to decay faster than that of the WT TM. This is particularly apparent at $200\mu m$ where $|\mathbf{U}_y|$ is nearly twice as high for the WT TM as for the $Tectb^{-/-}$ TM. In addition, as seen in Figure 2.6J, the phase tends to have a steeper slope in the $Tectb^{-/-}$ TM. If boundary effects are minimal, the quick decay and steep slope of $|\mathbf{U}_y|$ would be indicative of a smaller space constant and slower wave speed, respectively. Since, however, the wavelength is on the order of the TM length, a more detailed analysis of wave characteristics is required, as discussed in a later section.

While the radial displacement, $\mathbf{U}_y$, is approximately uniform in the radial direction, the longitudinal displacement, $\mathbf{U}_x$, plotted on Figures 2.6C-D and G-H, depends on both the longitudinal and radial positions. Not only is $\mathbf{U}_x$ highly spatially dependent, it is also of significant magnitude: $|\mathbf{U}_x|$ is as large as half of the average $|\mathbf{U}_y|$ along the left edge for the WT TM and of equal or greater magnitude than $|\mathbf{U}_y|$ along the left edge for the $Tectb^{-/-}$ TM, as seen on Figure 2.6K. In addition, over the length of the TM segments, the longitudinal motion tends to decay only slightly on the $Tectb^{-/-}$ TM and remains nearly constant in magnitude on the WT TM. Interestingly, the amplitude of $\mathbf{U}_x$ relative to the radial displacement at the left edge is significantly higher in TB1 than in WT1.

In previous studies[43,3,42,4], the motion of an isolated TM segment due to a harmonic, radial input was modeled as a decaying shear wave. However, in a shear wave, the TM moves only in the radial direction. The significant magnitude of the longitudinal-direction displacement relative to the radial-direction displacement indicates that TM motion cannot be adequately described as a shear wave.

With the addition of longitudinal-direction data, a model of the TM can be adequately constrained such that an inverse fitting method can be employed to find the anisotropic material properties of the TM, as discussed in the next section. This is in part why no previous reports of anisotropic material properties exist within the auditory frequency range: very few groups have the ability to make these measurements and prior to this study, none had published an experimental

data set sufficient to constrain the parameters of an anisotropic model.

2.5.2 Transversely isotropic fit model captures experimental motion in both radial and longitudinal directions

In the previous section, the amplitude and phase of the experimental data for WT1 and TB1 are given in order to best visualize the differences in longitudinal wave propagation between the two phenotypes. However, since the fitting algorithm tries to minimize the complex residual between the real and imaginary parts of the data and the model motion, in this section, the real and imaginary parts of the experimental data for WT1 are compared to that of the model best fit, seen on Figure 2.7, in order to evaluate the capacity of the model to capture the experimental data.

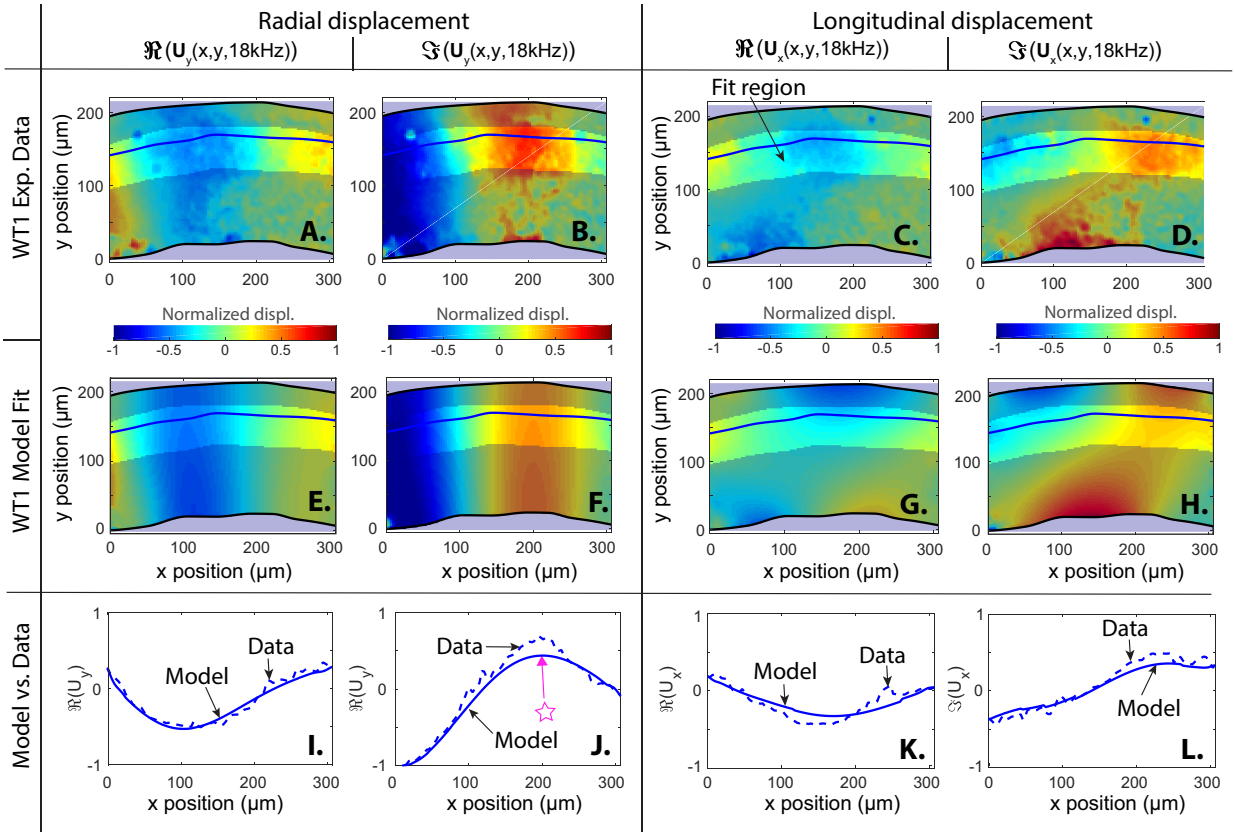

FIGURE 2.7. Experimentally captured motion for WT1(A-D) over TM area compared with WT1 model results (E-H) at 18kHz. On each plot, the highlighted area labeled "Fit region" on panel C, is the region used to calculate the solution fitness. I-L: Model results (solid line) vs. experimental data (dashed line) along one line (marked on A-H). Overall fit error for WT1 is $\epsilon_{avg} = 0.10$; the error at 18kHz for WT1 is $\epsilon(18\text{kHz})=0.06$.

Using a transversely isotropic material model, for WT1, the overall fit error value, ϵ_{avg} was

0.10. For both the longitudinal and radial displacements, the model captures features seen in the experimental data, such as the peak in the imaginary part of the radial motion at 200μm (marked with a star on Figure 2.7F) very well. Notably, the model is able to predict features seen in the experiments outside of the fitting region (the non-highlighted region on Figures 2.6A-B and G-J), such as the concentration of longitudinal motion at the top and bottom edges of the TM, indicating that the area chosen for the fitting algorithm is sufficient to constrain the parameters enough to capture the full data set.

2.5.3 Anisotropic material model necessary to capture experimental motion

To understand the necessity of using an anisotropic material model, the fitting procedure was repeated for each TM using an isotropic material model: the resulting error values for each TM are compared on Figure 2.8. As seen on Figure 2.8A, the error found by using an isotropic model is higher than the error found using a transversely isotropic model ($\Delta\epsilon = \epsilon_{avg}^{TI} - \epsilon_{avg}^{isotropic}$) by a median value of 0.06 for WT TMs and by a median value of 0.14 for $Tectb^{-/-}$ TMs. The inability of an isotropic model to capture the experimentally measured motion is illustrated by plotting the results for the isotropic and transversely isotropic best fits for WT1 (at 20kHz). As seen on Figure 2.8, for WT1, the isotropic model is able to fit the radial direction motion (panels A and B), but fails to capture the experimentally measured displacement in the longitudinal direction (panels C and D) whereas the transversely isotropic model is able to better capture the experimentally measured motion in both the longitudinal and radial directions.

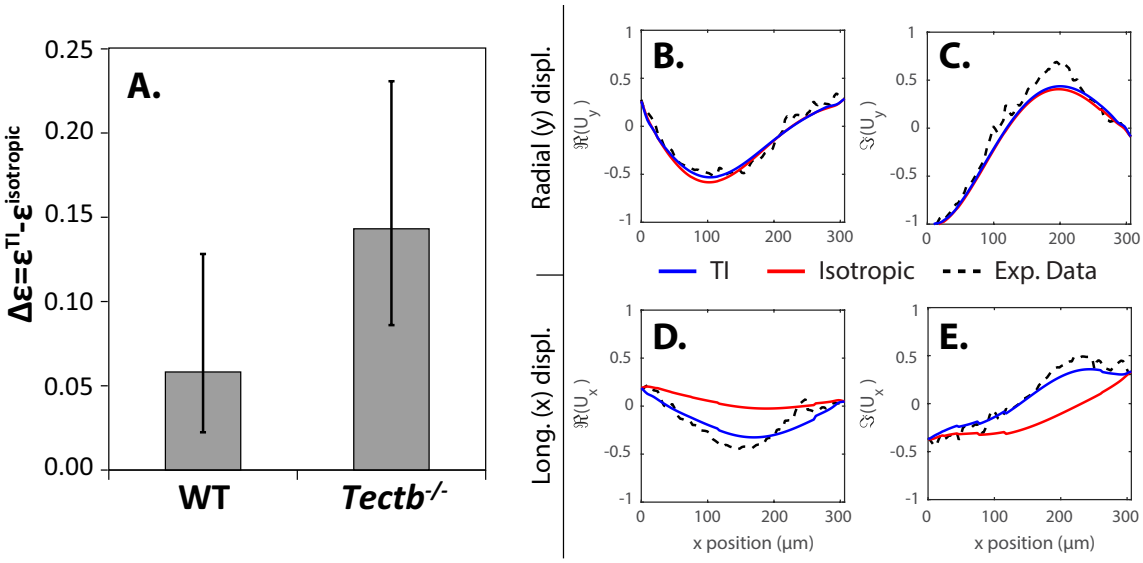

FIGURE 2.8. A. Median improvement in error due to introduction of anisotropy, $\Delta\epsilon = \epsilon^{TI} - \epsilon^{isotropic}$ where error bars represent the interquartile range found for each phenotype. B-E. Best fit displacement magnitude (A, C) and phase (B,D) results for WT1 when fit with a transversely isotropic (TI) model (in blue) and with an isotropic material model (in red) at 20kHz (where $\epsilon^{TI}_{WT1}(20kHz) = 0.09$ and $\epsilon^{isotropic}_{WT1}(20kHz) = 0.35$).

2.5.4 Significant differences in anisotropic material properties are found between the TMs of WT and $Tectb^{-/-}$ mice

The fitting procedure described in Methods Section was applied to multiple WT (n=6) and $Tectb^{-/-}$ (n=5) TMs to determine if statistically significant changes in anisotropic material properties due to the $Tectb^{-/-}$ mutation can be observed. The resulting transversely isotropic, viscoelastic material properties for WT and $Tectb^{-/-}$ TMs are plotted on Figures 2.9 and 2.10 where on each figure, the median values found for each phenotype are plotted with solid lines and the shaded area indicates the interquartile range found for each phenotype at each frequency. Reported values for the complex shear modulus from Sellon et al.[3] and Jones et al.[4] are also plotted on these figures; however, consideration of these values is reserved for the Discussion.

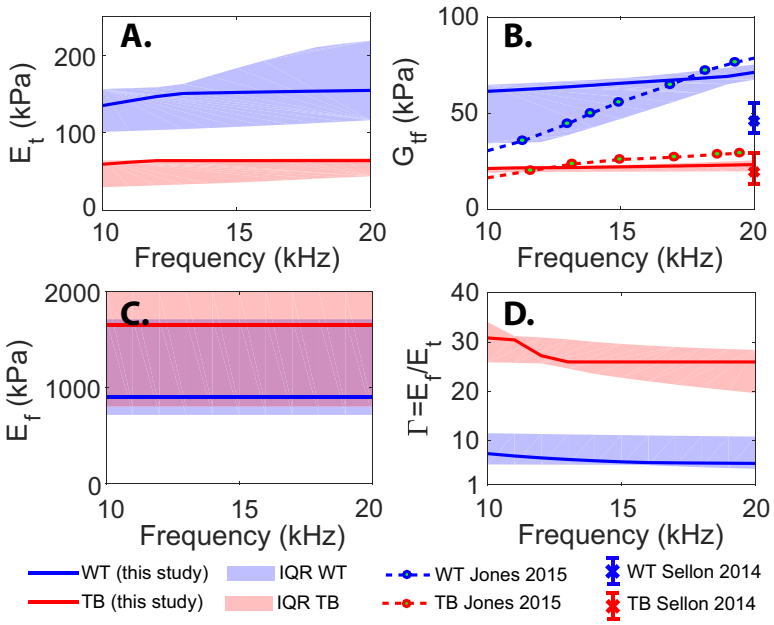

FIGURE 2.9. Effect of $Tectb^{-/-}$ mutation on anisotropic stiffness properties: the Young's moduli in the transverse (A) and fiber (C) directions, the in-plane shear moduli (B), and the anisotropy ratio (D). Median anisotropic storage moduli values found for WT (n=6) and $Tectb^{-/-}$ (n=5) mice TMs are plotted using solid lines. Shading indicates the interquartile range of material properties found in this study for each phenotype. Anisotropic material parameters from this study are compared to previously reported shear parameters from Sellon et al.[3] (only at 20kHz) and Jones et al.[4]. Error bars on Sellon et al.[3] data indicate the interquartile range. The interquartile range is not given for the Jones 2015[4] data and is therefore not shown here.

The largest difference between WT and $Tectb^{-/-}$ TMs was found to be the significant loss of stiffness in the transverse direction, E_t, and in shear G_{tf}, seen on panels B and C, respectively: this decrease in stiffness due to the $Tectb^{-/-}$ mutation was significant over the entire frequency range explored in this study. The statistical significance of these parameters is explored further in Appendix A. Briefly, the 95% confidence intervals of these two parameters do not overlap in any portion of the frequency range and a two-sample t-test conducted on the material properties of WT and $Tectb^{-/-}$ TMs suggests the null hypotheses stating $\bar{E}_t^{WT}(\omega_i) < \bar{E}_t^{Tectb^{-/-}}(\omega_i)$, $\bar{E}_t^{WT}(\omega_i) = \bar{E}_t^{Tectb^{-/-}}(\omega_i)$, $\bar{G}_{tf}^{WT}(\omega_i) < \bar{G}_{tf}^{Tectb^{-/-}}(\omega_i)$, and $\bar{G}_{tf}^{WT}(\omega_i) = \bar{G}_{tf}^{Tectb^{-/-}}(\omega_i)$ (where $\bar{(\bullet)}$ indicates a mean value) can be rejected at all frequencies ω_i explored in this study (at a 5% significance level).

The loss of stiffness in shear due to the $Tectb^{-/-}$ mutation found in this study is consistent with previously reported[3,4] findings, although the assumptions made to obtain these previously reported values are questionable, as mentioned previously. In addition, for $Tectb^{-/-}$ TMs, E_t and G_{tf} tend to be relatively constant across the explored frequency range, increasing by only 7.8% and 9.5%,

respectively, from 10 to 20 kHz. For WT TMs, however, E_t and G_{tf} increase by 14% and 16%, respectfully, from 10 to 20kHz.

As seen in Figure 2.9A, the interquartile ranges found for E_f for WT and $Tectb^{-/-}$ share considerable overlap: thus, a significant difference in the values of E_f between the two phenotypes is unable to be detected. It should be noted that the algorithm finds E_f values for two $Tectb^{-/-}$ TMs that hit the upper bound set for E_f (2000 kPa). The motion of the TM appears to be relatively independent of the value of E_f provided that the ratio of E_f to E_t is sufficiently large, as discussed in the following subsection. As such, the inability of the algorithm to find a precise value of E_f does not hinder its ability to find values for the other material parameters, as discussed in Appendix A. In all $Tectb^{-/-}$ TMs and in the majority of WT TMs, the TM is found to be significantly anisotropic (the anisotropy ratio, $\Gamma(\omega) = E_f/E_t(\omega)$ is significantly larger than 1 from 10-20kHz), as shown on Figure 2.9D. Furthermore, $\Gamma(\omega)$ is consistently higher in $Tectb^{-/-}$ TMs than in WT TMs.

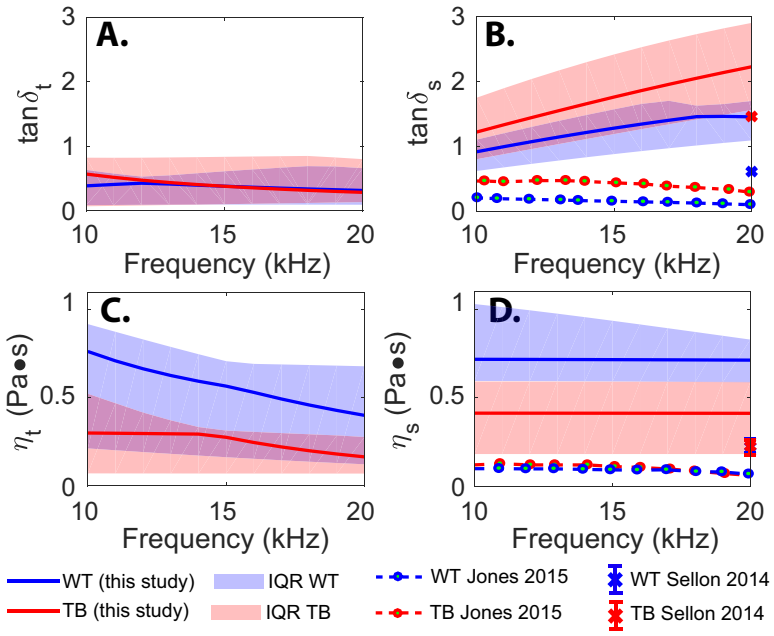

FIGURE 2.10. Effect of $Tectb^{-/-}$ mutation on anisotropic damping properties: the loss tangent in the transverse direction (A), the loss tangent in shear (C), the transverse direction viscosity (C), and the shear viscosity (D). Median material loss tangent (A-B) and viscosity (C-D) values found for WT (n=6) and $Tectb^{-/-}$ (n=5) mice TMs are plotted with solid lines. Shading indicates the interquartile range of material properties found in this study for each phenotype. Anisotropic material parameters from this study are compared to previously reported shear parameters from[3] (only at 20kHz) and[4]. Error bars on Sellon et al.[3] data indicate the interquartile range: note the loss tangent values are calculated using the median shear modulus and shear viscosity and were not published. Thus, interquartile ranges for the Sellon et al. loss tangents are not given. The interquartile range is not given for the Jones et al.[4] data.

The damping of a viscoelastic material can be characterized by several different measures. For example, Ghaffari et al.[43] and Sellon et al.[3] reported the shear viscosity of the TM, $\eta_s(\omega)$. The viscosity in shear and in the transverse direction at a given frequency are related to the shear and transverse loss tangents by Eqs. 2.9.

$$\eta_s(\omega) = (G_{tf}(\omega) \times \tan\delta_s(\omega))/\omega \quad \text{and} \quad \eta_t(\omega) = (E_t(\omega) \times \tan\delta_t(\omega))/\omega \tag{2.9}$$

In this study, both the loss tangent and the viscosity in shear and in the transverse direction, shown on Figures 2.10A-D, are reported. A significant difference in the loss tangents due to the $Tectb^{-/-}$ mutation is unable to be detected. A small decrease in the shear viscosity, η_s, is observed due to the $Tectb^{-/-}$ mutation (a median decrease of 50%). For both WT and $Tectb^{-/-}$ TMs, the loss tangent in shear, $\tan\delta_s$, tends to be significantly higher than that in the transverse direction, $\tan\delta_t$: the

fiber direction was assumed lossless ($\tan\delta_f = 0$).

2.5.5 Alteration of mechanical properties due to $Tectb^{-/-}$ mutation significantly changes TM motion

The aim of this section is to characterize how the $Tectb^{-/-}$ mutation affects the radial and longitudinal motion of isolated TM segments. Although a shear wave is too simplistic to fully describe the motion of the TM, the amplitude and phase of the radial displacement, $\mathbf{u}_y(x,y,t)$, can be used to determine the wave speed c and space constant σ of a longitudinally-propagating wave of decaying amplitude, as was done in previous studies[3,4]. Because of the presence of a reverse traveling wave due to reflection at the apical edge of the TM, the radial displacement can be written as:

$$\mathbf{u}_y(x,t) = \left(\mathbf{U}_f e^{-i\mathbf{k}x} + \mathbf{U}_r e^{i\mathbf{k}x}\right) e^{i\omega t} \tag{2.10}$$

where $\mathbf{k}$ is the complex wave number which can be expressed as,

$$\mathbf{k}(\omega) = \omega/c - i/\sigma \tag{2.11}$$

In Eq. 2.10, $\mathbf{U}_f$ and $\mathbf{U}_r$ are the amplitudes of the forward-traveling and reverse-traveling waves, respectively, and are found from the boundary conditions at the basal and apical edges of the TM.

On Figures 2.11A-B, the median values of c and σ calculated by fitting the radial displacement measurements in this study using Eq. 2.10 are compared to previous reports of c and σ at 20kHz from Refs. 3, 4. One outlier, WT9 (whose value for σ was two standard deviations above the mean σ value found for WT TMs), was removed from this analysis. As seen in Figure 2.11A-B, in all studies, a decrease in c and a large reduction in σ due to the $Tectb^{-/-}$ mutation are observed. The smaller value found for σ in $Tectb^{-/-}$ TMs indicates that the radial motion decays at a faster rate in these TMs than in WT TMs. While similar values for σ were found here and in Ref. 3, Jones et al.[4] found significantly larger space constants for both phenotypes. The large σ values reported by Jones et al. could be because they do not consider the finite length of the TM in their analysis: reverse-traveling waves due to a reflection at the apical edge might artificially inflate their reported values of σ.

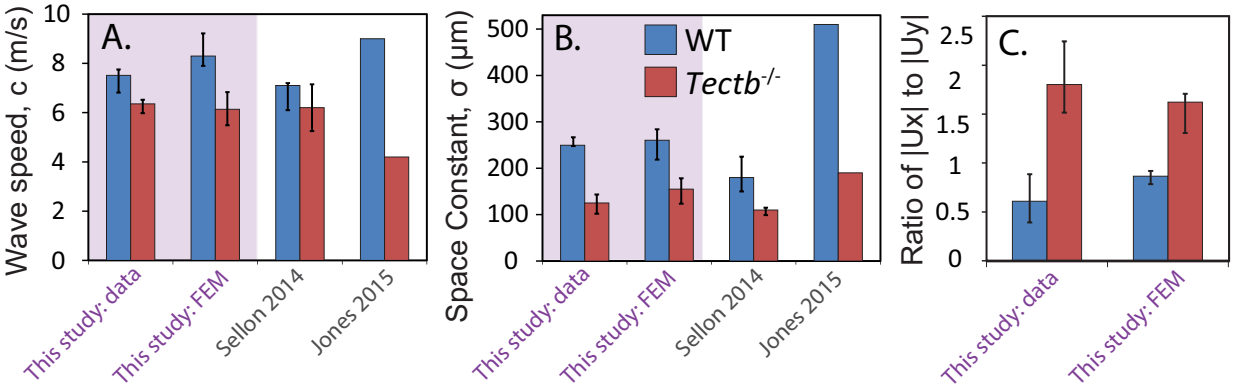

FIGURE 2.11. Analysis of TM motion at 20kHz. A-C. Comparison of median TM wave speeds, space constants, and ratios of longitudinal to radial displacement found between phenotypes along a line 40μm above the bottom of the fit region (where the fit region is defined on Figure 2.7C and the lines for TB1 and WT1 are seen on Figures 2.6A-H). The error bars indicate the interquartile range. The A. wave speeds, c, and B. space constants, σ, found in this study are compared with previously reported values from Sellon et al.[3] and Jones et al.[4] at 20kHz. The values from our study are found by fitting Eq. 2.10 to [1] the experimental measurements of radial displacement and to [2] the resulting radial motion of a finite element model (described in Figure 2.3) after inserting the material properties found for each TM in this study. C. The ratio of the amplitudes of the longitudinal and radial displacements at a point P. For the experimental data, this point is shown with a magenta asterisk on Figure 2.7A, C, G, and H). For the finite element model, this point is marked with a black asterisk on Step 1 of Figure 2.3

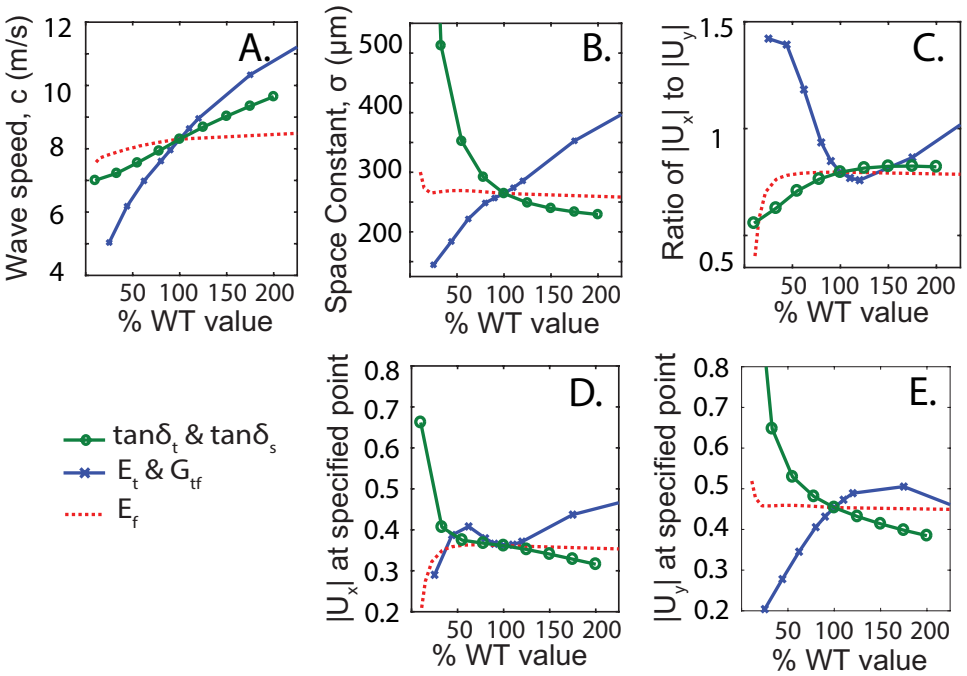

FIGURE 2.12. A parametric study of TM motion is conducted by varying the material parameters of a finite element model described in Step 1 of Figure 2.3. In all cases, the parameter is varied from the median WT value. The A. wave speed and B. space constant due to changes in material properties are compared. C. Changes in ratio of the amplitudes of the longitudinal displacement to the radial displacement at a point marked with a black asterisk on Step 1 of Figure 2.3 are plotted. D. and E. Changes in the amplitudes of the longitudinal and radial displacements, $|\mathbf{U}_x|$ and $|\mathbf{U}_y|$, at the aforementioned point are plotted.

As observed in Figure 2.6, the ratio of the magnitude of longitudinal displacement, $|\mathbf{U}_x|$, to the magnitude of the radial displacement, $|\mathbf{U}_y|$, tends to be higher for the TB1 TM than the WT1 TM. To determine whether there is a systematic difference between $|\mathbf{U}_x|/|\mathbf{U}_y|$ for WT and $Tectb^{-/-}$ TMs, this ratio was computed for all TMs (excluding WT9) at $\Delta x = 80\mu$m from the left edge of the data along a line 40μm from the bottom of the fit area (where the fit area is defined on Figure 2.7C): on Figures 2.7A, C, G, and H, this point is marked with a magenta asterisk. This location was chosen because the difference between the WT and $Tectb^{-/-}$ TMs was the clearest at that point. The results, shown in Figure 2.11C, demonstrate that at this location, $|\mathbf{U}_x|/|\mathbf{U}_y|$ is significantly higher in $Tectb^{-/-}$ TMs than in WT TMs.

To identify which individual parameters of the TM are responsible for the changes in TM motion observed in $Tectb^{-/-}$ TMs, a parametric study of TM motion was conducted using a finite element model of the TM (described in Step 1 of Figure 2.3). The geometry and boundary conditions of this model are fixed; however, the material properties were varied according to the results given in Figures 2.9 and 2.10. As seen in Figure 2.11, by changing the TM properties from the WT values to the $Tectb^{-/-}$ values, the finite element model is able to capture the differences in c, σ, and the ratio of longitudinal to radial displacement due to the $Tectb^{-/-}$ mutation. Note that the $|\mathbf{U}_x|/|\mathbf{U}_y|$ ratio was, for this model, calculated at a point $\Delta x = 100\mu$m from the edge of the "visible" data, marked with a black asterisk on Step 1 of Figure 2.3. Like in the experimental data, this location was chosen because the difference between the WT and $Tectb^{-/-}$ TMs was the clearest at that point.

A parameter sensitivity study was then conducted with the finite element model to determine the influence of the transverse and shear stiffnesses, E_t and G_{tf} (properties largely controlled by the properties of the TM matrix, detailed in the Discussion), the fiber direction stiffness, E_f, and the damping parameters ($\tan\delta_t$ and $\tan\delta_s$) on TM motion. For each TM parameter, the baseline value was set to the median value obtained for WT TMs. By decreasing E_t and G_{tf} from their baseline values to levels found in this study for $Tectb^{-/-}$ TMs (approximately $\approx 40\%$ of the WT value), c and σ are significantly reduced, as seen in Figures 2.11A-B : the reduction of E_t and G_{tf} seen in $Tectb^{-/-}$ TMs appears to be the main source of the reduction in σ and c observed on $Tectb^{-/-}$ TMs. Additionally, as seen on Figure 2.12C, by reducing E_t and G_{tf}, the ratio of longitudinal to radial displacement is dramatically increased. This is due to a large drop in amplitude of the

radial motion, as seen on Figure 2.12E, as the longitudinal displacement amplitude is only slightly reduced. In other words, while the reduction of E_t and G_{tf} due to the $Tectb^{-/-}$ mutation causes the radial motion to be attenuated much more quickly than in WT TMs, this attenuation is not nearly as dramatic in the longitudinal direction. As a result, the ratio of $|\mathbf{U}_x|$ to $|\mathbf{U}_y|$ is much higher in $Tectb^{-/-}$ TMs.

The stiffness in the fiber direction, E_f does not seem to significantly affect c or σ. However, as seen in Figure 2.12C-D, if E_f is reduced any lower than $\approx 50\%$ of the median WT value (nearing an anisotropy ratio $\Gamma = E_f/E_t = 1$), the ratio of $|\mathbf{U}_x|$ to $|\mathbf{U}_y|$ decreases sharply due to a significant reduction in $|\mathbf{U}_x|$. This helps to explain why, as discussed in a previous subsection, an anisotropic material model is needed to capture both the longitudinal and radial motion seen in the experimental data and why the algorithm struggles to capture the precise value of E_f while consistently finding $E_f >> E_t$.

As seen in Figure 2.12A-B, adjusting the value of the two loss tangents, $\tan\delta_t$ and $\tan\delta_s$, significantly affects σ while only slightly altering reducing c. Additionally, as seen in Figure 2.12D-C, by decreasing the damping, $|\mathbf{U}_y|$ increases more than $|\mathbf{U}_x|$ and thus the ratio of $|\mathbf{U}_x|$ to $|\mathbf{U}_y|$ is decreased.

2.5.6 Fiber orientation and TM width play significant role in TM motion

In addition to investigating the influence of each material property on TM motion, the effects of the TM's width and fiber orientation on its motion were evaluated, as seen in Figure 2.13. As in the previous section, a parameter sensitivity study was conducted where the values of the TM's width, W_{model}, and fiber orientation, θ, are varied from a baseline value. The baseline value for W_{model} was set equal to the median width found for WT TMs, $W_{model} = 173\mu m$: W_{model} is described on Step 1 of Figure 2.3. The baseline value for θ was set equal to the fiber orientation used in all models in this study, $\theta = 15°$ (based on measurements of fiber orientation in the mouse given in Ref. 48): θ is defined on Figure 2.2B.

While the $Tectb^{-/-}$ mutation is not known to significantly affect the fiber orientation or geometry of the TM, the fiber orientation and width of the TM varies significantly between species. In humans, for example, the TM is $\approx 250\%$ wider than in the mouse and the fibers are oriented $35°$ from the radial direction, a value $\approx 200\%$ larger than in mice[48]. In previous studies, similar

wave speeds and space constants were observed on isolated, basal segments of mouse and human TMs[51,48]. Since the wave speeds and space constants between the two species were similar, using the approach outlined in Ref. 3, the TM shear moduli and shear viscosities for these two species were found to be of similar value[52]. Without knowing how the width and fiber orientation each affect the motion of the TM, however, it is difficult to know whether the conclusions about the material properties of the human TM can be conclusively drawn based only on measurements of c and σ.

While the orientation of the fibers, θ, does not seem to significantly affect the wave speed, c, the width of the TM, W_{model}, does seem to affect the value found for c (albeit in a non-monotonic manner). Increasing the fiber angle from 50% of θ used in this study to 220%, σ increases by 44%; contrarily, increasing the TM width from that of the median WT value does not significantly change σ. Thus, if the material properties of mouse and human basal TM segments were the same, it would be expected that c for human TMs would be $\approx 25\%$ higher (due to the larger width of human TMs) and σ would be $\approx 35\%$ higher (due to the difference in fiber orientation between these two species) than the values found for mice TMs.

Furthermore, as demonstrated in this study, TMs are highly anisotropic at audio frequencies. The values of all anisotropic material properties influence the ratio of the longitudinal to radial motion. From Figures 2.13C-E, it can be seen that θ and W_{model} also significantly affect the ratio of $|\mathbf{U}_x|$to $|\mathbf{U}_y|$. Therefore, if the material properties of the human TM were equal to that of the mouse TM, it would be expected that $|\mathbf{U}_x|/|\mathbf{U}_y|$ would be significantly lower than that seen in the mouse. However, the longitudinal motion on isolated human TM segments has not been published. Were this data to be published, a similar fitting methodology as was done here would be suggested in order to characterize the anisotropic material properties of human TMs at audio frequencies.

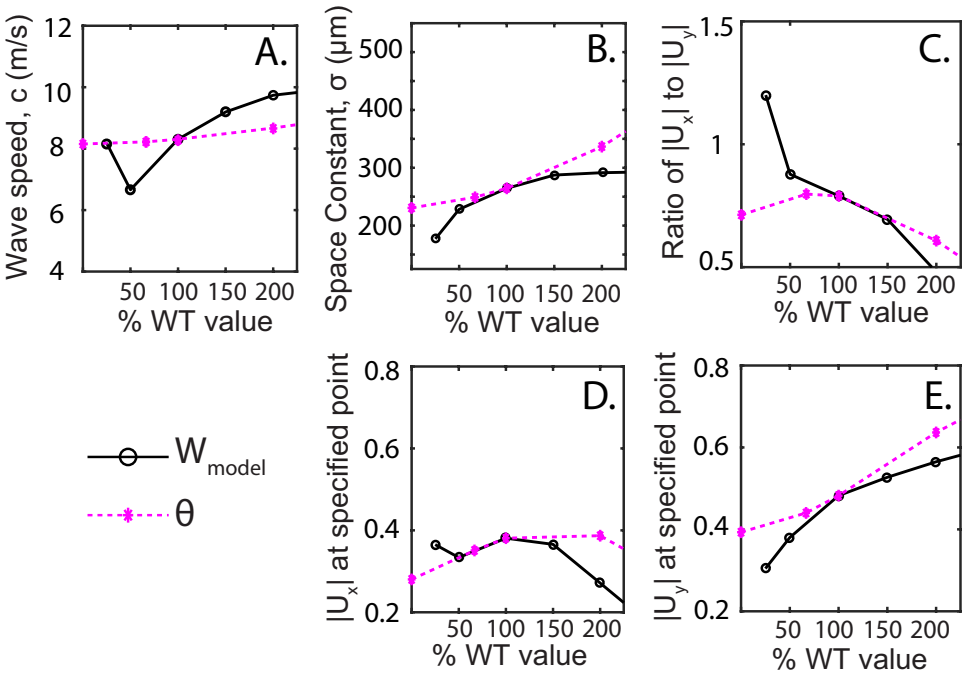

FIGURE 2.13. A parametric study of TM motion is conducted by varying the width, W_{model} (defined in Figure 2.3, Step 1), and fiber orientation, θ (defined on Figure 2.2B) of a finite element model described in Step 1 of Figure 2.3. In both cases, the parameter is varied from the median WT value. The A. wave speed and B. space constant due to changes in fiber orientation and TM width are compared. C. Changes in ratio of the amplitudes of the longitudinal displacement to the radial displacement at a point marked with a black asterisk on Step 1 of Figure 2.3. D. and E., changes in the amplitudes of the longitudinal and radial displacements, $|\mathbf{U}_x|$ and $|\mathbf{U}_y|$, at the aforementioned point, respectively, due to changes in TM width and fiber orientation are compared.

2.6 Discussion

2.6.1 Only longitudinal displacement of TM is radially-dependent

As seen on Figures 2.6A-D and 2.7A-D, for both WT and $Tectb^{-/-}$ TMs, the radial direction motion is nearly radially uniform: this was found to be the case in all TMs at all frequencies examined here. This radially uniform radial motion would be advantageous physiologically as OHCs within one longitudinal cross-section would be excited in phase by the TM: cooperation of OHCs within one longitudinal cross-section might be needed to maximize the efficiency of cochlear amplification.

Contrarily, as seen on Figures 2.6G-J and 2.7G-J, the longitudinal direction motion is highly spatially dependent in both the longitudinal and radial directions. This highly spatially dependent motion is influenced significantly by the anisotropy and finite width of the TM. Although significant longitudinal motion has been detected on other components of the organ of Corti[53,54], it remains

to be seen if significant longitudinal vibration of the TM is observed in vivo given that the TM is attached to the spiral limbus and outer hair cell hair bundles, as seen in Figure 2.1. Progress in optical coherence tomography (OCT) recording techniques have made TM vibration measurements in the radial and transverse (z) directions possible[29]. Similar techniques could potentially be used to observe in vivo measurements of longitudinal TM vibration. These measurements could determine if TM motion in the longitudinal direction is significant. However, even if longitudinal motion is not present in vivo, the in vitro longitudinal motion that was used in this study provides key information about the intrinsic, anisotropic mechanical properties of the TM.

2.6.2 Comparison of material properties found in this study vs. previously reported values

In this section, the material properties found in this study are compared to those reported previously in order to assess whether the values found here are reasonable and to test the validity of previously reported dynamic material properties based on the assumption of shear wave propagation.

While no measurements of the anisotropic elastic moduli of the mouse TM have been reported, using static Atomic Force Microscopy measurements, Gavara and Chadwick[38] found an anisotropy ratio, $\Gamma = E_f/E_t$, of 7 in isolated basal segments of the gerbil TM. In WT TMs at audio frequencies, we found very similar values, ranging from ≈ 7 at 10kHz to ≈ 5 at 20kHz. Although the mouse TM is about 5-8 times stiffer than in the gerbil TM[33,55], this increase in stiffness does not appear to be limited to one direction as the anisotropy ratio is similar in these two species. Gu et al.[40] measured the longitudinal and radial shear impedance, $\mathbf{Z}_R$ and $\mathbf{Z}_L$, between 0.01 and 1 kHz for apical, mouse TM segments: they found $|\mathbf{Z}_R|/|\mathbf{Z}_L|$ to be between 1-8.3 at 0.01kHz and 3.7-11.7 at 1kHz. Although shear impedance measurements cannot be directly compared to estimates of the anisotropic elastic moduli, this observation is similar to our finding that the WT TM is significantly stiffer in the fiber direction than in the transverse direction.

Since the TM is highly viscoelastic[33,4], its material properties are frequency-dependent such that comparison of the TM material properties found here to other estimates found at audio frequencies[3,4] is the most meaningful. Sellon et al. and Jones et al.[3,4] used identical (in Ref. 3) or similar (in Ref. 4) experimental set-ups as seen on Figure 2.2A. However, in both of these studies, only the radial displacement along one line was reported. In these studies, to determine the material properties of

the TM, the finite width of the TM was neglected and the TM was assumed to move only in the radial direction. These assumptions are clearly not valid, since we observe significant longitudinal motion of the TM (shown on Figures 2.6G and I). Thus, the validity of the values found in Refs. 3, 4 is examined by comparing them to the material properties found in this work which capture the experimental motion in both directions. Note that in Refs. 3, 4, only the values of the shear modulus and damping in shear were reported, plotted in Figure 2.9B and Figures 2.10B and D.

At high frequencies (near 20kHz), for both phenotypes, Jones et al.[4] found very similar shear stiffness values as found here for G_{tf}. Sellon et. al[3] found similar G_{tf} values as found here for $Tectb^{-/-}$ mice, but underestimate G_{tf} in WT mice by a factor of ≈ 1.5. As in this study, Jones et al.[4], found that G_{tf} in WT TMs increases significantly with frequency; however, this frequency-dependent stiffening is markedly less dramatic in $Tectb^{-/-}$ TMs, as found here. Both previous studies[3,4] found lower loss tangent values than the values reported here. The significantly lower loss tangent values found by Jones et al. are likely due to (1) the consideration of the viscous boundary layer in their model (which our model lacks), and perhaps more significantly, (2) the assumption of infinite TM length (since the wavelengths are on the order of the TM length, boundary effects are non-negligible such that estimating the space constant by fitting the amplitude data using a single exponential can result in inaccurate values).

Thus, although the finite width of the TM was not considered by Sellon et al. or Jones et al., these previous studies[3,4] provide reasonable, but incomplete, measures of TM material properties. Since the TM is highly anisotropic, the motion of the TM cannot be fully described using shear properties alone: knowledge of the viscoelastic properties in the fiber and transverse directions is also needed.

2.6.3 Absence of the SSM largely alters TM transverse and shear stiffness

The TM is composed of radially oriented collagen fibers embedded in sheets of noncollagenous matrix with a striated appearance[21,35]. A total loss of this major structural component of the TM, the SSM, is reported in TMs of $Tectb^{-/-}$ mutant mice[21]. Changes in the mechanical properties of the TM due to alterations to the SSM can be understood by using a micromechanics approach to simplistically model the TM as a continuous fiber-reinforced composite material. Using this approach, E_f, E_t, and G_{tf} can be expressed in terms of the moduli and volume fractions of the

fiber and the matrix using the rule of mixtures[56]:

$$E_f^{MM} = E_{col}V_{col} + E_{mat}V_{mat} \quad , \quad E_t^{MM} = \frac{E_{col}E_{mat}}{E_{col}V_{mat} + E_{mat}V_{col}}$$
$$\text{and} \quad G_{tf}^{MM} = \frac{G_{col}G_{mat}}{G_{col}V_{mat} + G_M V_{col}} \tag{2.12}$$

where MM indicates a value found using a micromechanics approach, V_{col} and V_{mat} are the volume fractions of the collagen fibers and the matrix, respectively, E_{col} and E_{mat} are the Young's moduli of the collagen fibers and the matrix, respectively, and G_{col} and G_{mat} are the shear moduli of the collagen fibers and the matrix, respectively. If it is assumed that the total volume of the fibers is much less than that of the matrix, $V_{col} << V_{mat}$, and that the stiffness of the fibers is much greater than that of the matrix, $E_{col} >> E_{mat}$ and $G_{col} >> G_{mat}$, then Eq. 2.12 becomes

$$E_f^{MM} \approx E_{col}V_{col} \quad , \quad E_t^{MM} \approx E_{mat}/V_{mat} \quad \text{and} \quad G_{tf}^{MM} \approx G_{mat}/V_{mat} \tag{2.13}$$

Thus, if disruption of the SSM changes of the properties of the matrix, E_{mat} and G_{mat}, without affecting the volume fraction of the collagen fibers, from Eq. 2.13, it becomes clear that E_t and G_{tf} would be significantly altered, as observed in this study (and in previous studies[4,3] for the shear stiffness). As seen on Figures 2.9A-B, at 20kHz, a median 57% reduction in transverse direction stiffness and a median 67% reduction in shear stiffness was found: the similarity of these values implies that G_{mat} and E_{mat} might be reduced by a similar amount. On the other hand, since E_{col} is on the order of 1 GPa[57,58], the value of E_f is dominated by the stiffness of the fibers and is not significantly affected by an alteration in matrix properties. As mentioned in the Results Section, although the fitting algorithm struggles to find the precise value of E_f, the results of this study do not indicate that the $Tectb^{-/-}$ mutation reduces stiffness in the fiber direction.

2.6.4 Implications of changes in TM material properties on cochlear physiology

Disruption of the SSM due to the $Tectb^{-/-}$ mutation has been found to sharpen the tuning of the BM in response to a low-level pure tone and of neural masking curves[21]. In this study, alteration of the SSM was found to greatly reduce the stiffness of TM in shear and in the transverse direction, which would reduce TM longitudinal coupling. A reduced spread of excitation in consequence to

weaker TM longitudinal coupling could be partially responsible for the enhanced tuning reported in $Tectb^{-/-}$ mice[21,3,4]. Indeed, Meaud and Grosh[44] showed that a cochlear model with a locally reacting TM model exhibits sharper tuning than a model with longitudinal coupling. However, in addition to its effect on cochlear tuning, Russell et al. reported that the $Tectb^{-/-}$ mutant mice also have reduced cochlear sensitivity. This is in contrast with the theoretical study conducted by Meaud and Grosh[44] who predicted that this sharper tuning is associated with higher sensitivity.

Perhaps, the large reduction in E_t plays a role in the reduced sensitivity in $Tectb^{-/-}$ mutants: this large reduction in E_t might allow OHC and IHC hair bundles to deflect more easily in the longitudinal direction. Longitudinal-direction deflection of hair bundles would be inefficient given that OHC channels hair bundle mechano-electric transduction channels open due to a radially-oriented stimulation of hair bundles[59]. Additionally, a slight increase in $\tan\delta_s$ due to the $Tectb^{-/-}$ mutation was found. Reduced longitudinal coupling due to lower G_{tf} and slightly higher damping in $Tectb^{-/-}$ mutants may, when combined, be responsible for the sharper tuning and reduced sensitivity reported in $Tectb^{-/-}$ mice. $Tectb^{-/-}$ mice tend to produce more spontaneous otoacoustic emissions than observed in WT mice[28]. The increased longitudinal motion of the TMs in these mice might contribute to the additional spontaneous otoacoustic emissions.

2.7 Summary of Contributions & Conclusions

In this study, for the first time, the anisotropic, viscoelastic material properties of wild-type and transgenic mice were reported at auditory frequencies. These material properties were found using an inverse fitting algorithm which sought the material parameters of finite element models which best capture experimentally measured displacements of isolated TM segments provided by our collaborators. The accuracy and precision of the fitting algorithm were assessed: the differences in the material properties seen between phenotypes were found to be due to actual changes in the material properties of these TMs rather than an artifact of the fitting algorithm. The inverse fitting algorithm was repeated on the TMs of several WT and $Tectb^{-/-}$ mice: doing so, I was able to uncover statistically significant changes in the anisotropic, dynamic material properties of the TM due to the $Tectb^{-/-}$ mutation. Finally, a parameter study was conducted in order to determine the influence of the TM's material parameters, width, and fiber orientation on its motion. The results

of this analysis suggest that at auditory frequencies, the material properties of the TMs of humans are different than in mice. A study which considers the finite width and anisotropy of the TM, as was done in this thesis, is needed to quantify these differences in material properties.

Knowledge of the material properties of the TM are necessary in order to elucidate the role of the TM in cochlear mechanics: these properties give insight into how genetic mutation affects the mechanical properties of the TM. In a future study, these material properties could be inserted into computational models of the cochlea which would allow (1) for more realistic modeling of the TM and (2) the consequences of the $Tectb^{-/-}$ mutation on cochlear mechanics to be evaluated. Additionally, the inverse fitting algorithm could be applied to experimental measurements of isolated TM segments of other genetically modified mice (such as the $Tecta^{Y1870C/+}$ mutation[20]) or of other species should the data become available.

Chapter 3

Influence of middle-ear properties on its ability to transmit sound

3.1 Chapter overview

In this chapter, I aim to (1) develop a circuit model of the chinchilla middle ear by modifying the topology and parameter values of existing mammalian middle-ear models and to (2) use this model to examine the effects of inertial, stiffness, and damping properties on the middle ear's ability to transmit sound. While a significant amount of experimental data on the chinchilla middle ear had been published, no circuit model of the chinchilla middle ear existed in literature prior to this model (and only one other model, a finite element model[60], of the chinchilla middle ear was available at the time the model described in this chapter was published in a journal article[61]). The simplicity of the model allowed for direct relation of the model parameters to features in the experimental data using analytical expressions. Doing so, I was able to use reported values of the transmission matrix parameters in order to evaluate differences in ossicular joint stiffness across several mammalian species.

3.2 Introduction to middle-ear mechanics

3.2.1 Overview of middle ear physiology

The mammalian middle ear allows acoustic energy to be efficiently transferred from the ear canal to the inner ear through a broad range of frequencies. At the end of the ear canal lies the eardrum, the first component of the middle ear. As seen on Figure 3.1A-B, the eardrum is directly coupled with the malleus, the first of the three bones which comprise the ossicular chain. In normal hearing, sound travels through the ear canal where it vibrates the eardrum which in turn causes the ossicular chain to move. The ossicular chain and connecting joints and ligaments which comprise the middle ear are enclosed in an air-filled cavity called the middle ear cavity, as seen in Figure 3.1C. After

traveling through the ossicular chain, the stapes footplate vibrates the water-like fluid within the inner ear.

In this chapter, sound traveling from the ear canal into the inner ear will be referred to as traveling in the "forward" direction. Sound can also be generated by the inner ear itself; these sounds are called otoacoustic emissions (OAEs)[62]. OAEs travel from the inner ear, through the ossicular chain and the eardrum, and into the ear canal where they are measured: this direction will be referred to as the "reverse direction."

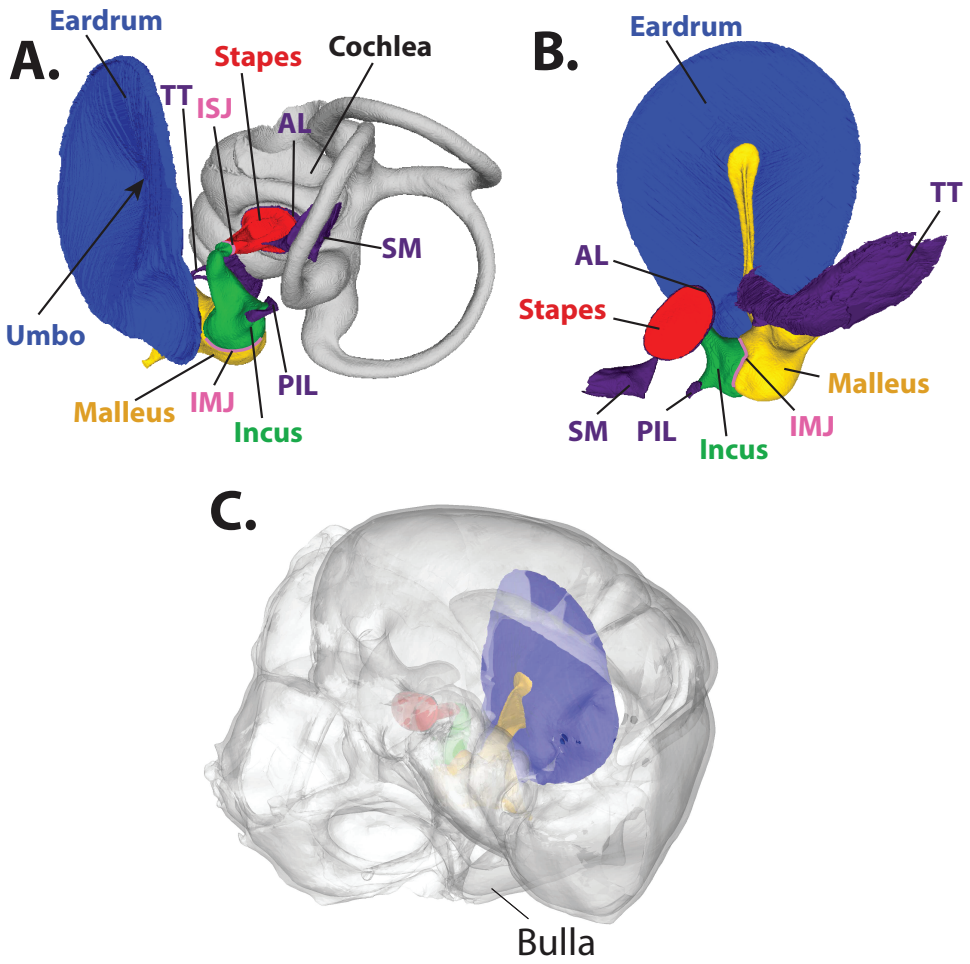

FIGURE 3.1. Depiction of the mammalian middle ear (from a publicly available 3D scan of a gerbil middle ear[5]). A. Front view of the middle ear attached to the cochlea. B. Rear view of the middle ear. In both A and B, the eardrum is noted in blue: on A, the location of the umbo is noted (which is the center, most inverted portion of the mammalian eardrum). Each ossicle is depicted with a single color: the malleus is yellow, the incus is green, and the stapes is red. The incudomalleolar joint (IMJ) and incudostapedial joint (ISJ) are both noted in magenta. Tendons and muscles are colored purple: "TT" is the tensor tympani muscle, "AL" is the annular ligament, "SM" is the stapedius muscle, and "PIL" is the posterior incudal ligament. C. The eardrum and ossicular chain situated within the air-filled middle-ear cavity (the cavity formed from the bony wall surrounding the middle ear, the bulla).

3.2.2 Background: middle-ear modeling

In an effort to better understand middle-ear mechanics, circuit and finite-element models of human, cat, and rodent middle ears have been previously developed, as reviewed in Ref. 63. Circuit models have well-known limitations. For example, they cannot represent three-dimensional ossicular motion at high frequencies[64] or complex vibration patterns of the eardrum[65,66]. However, while

circuit models generally have trouble representing higher order motion, they have value as concise representations of experimentally observed phenomena and are sufficient in relating inputs and outputs of the middle ear[63].

The simplicity of circuit models allows for insight into the effects of each component of the middle ear with little computational cost, especially when compared to finite-element models. In practice, this means circuit models can be easily coupled with computational models of the cochlea in order to directly compare experimental measurements of OAEs in the ear canal with model simulations[1,67]. Additionally, the simplicity of circuit models makes it possible to derive analytical expressions which directly relate the model parameters to transfer function measurements. Hence, with circuit models, measurements of the inputs and outputs of the middle ear provide more information than just the transmission properties of the middle ear: they allow for insight into the stiffness, damping, and inertial properties of individual bones, joints, and ligaments of the middle ear.

3.2.3 Chinchillas and hearing mechanics

The chinchilla is a well-studied species, in part because chinchillas and humans share similar hearing ranges[68] (the hearing range of the chinchilla extends from 50 Hz to 33 kHz[69]) and eardrum dimensions[68,70]. As such, numerous measurements of sound transmission through the chinchilla middle ear have been published[9,11,12,13,71,14,10]. However, before the development of the circuit model discussed in this chapter and a finite element model by Wang et al.[60] in 2016, no models of the chinchilla middle ear had been published. With the addition of these models, the underlying mechanics behind the experimentally measured middle ear motion can be better understood.

3.2.4 Background: characterization of middle-ear function via two-port transmission matrix

The middle ear plays a role in the transmission of acoustic energy in both the forward and reverse directions. Hence, in order to properly validate a middle-ear model, an experimental data set that fully characterizes the relationship between the inputs and outputs of the middle ear in both directions is needed. In this subsection, characterization of the inputs and outputs the middle ear by a two-port transmission matrix (as was done by Ref. 16 for the human middle ear, Ref. 15 for the cat middle ear, and Ref. 10 for the chinchilla middle ear) is discussed. This method of

characterization is used in the following sections to relate the parameters of my circuit model of the chinchilla middle ear to features seen in experimental data.

The middle ear can be characterized as a two-port system with one port in the ear canal and the other at the stapes footplate[72] (as seen in Figure 3.2). This two-port system can be represented with a two-port transmission matrix in which four matrix parameters, A, B, C, and D, relate the inputs and outputs of the middle ear and allow for characterization of the middle-ear independent of the influence of the termination loads. The relationship between the inputs and outputs of the two-port system can be written as

$$\begin{Bmatrix} P_{ed} \\ U_{ed} \end{Bmatrix} = \begin{bmatrix} A & B \\ C & D \end{bmatrix} \begin{Bmatrix} P_s \\ U_s \end{Bmatrix} \tag{3.1}$$

where P_{ed} and U_{ed} are the pressure and volume velocity in the ear canal at the eardrum, respectively; P_s and U_s are the pressure and volume velocity at the stapes footplate, respectively; and A, B, C, and D are the two-port transmission matrix elements[73].

These two-port matrix parameters can be estimated by measuring the pressure and the volume velocity in the ear canal and the volume velocity at the stapes footplate (and by assuming reciprocity) in two different cochlear conditions: (1) with a fixed stapes and (2) with a drained cochlea, as was done for the chinchilla in Ref. 10. By examining Eq. (3.1), it is seen A, B, C, and D can be physically interpreted in the following manner[16,10]:

$$\begin{aligned} A &= \frac{P_{ed}}{P_s}\Big|_{\text{Fixed stapes}} \\ B &= \frac{P_{ed}}{U_s}\Big|_{\text{Drained cochlea}} \\ C &= \frac{U_{ed}}{P_s}\Big|_{\text{Fixed stapes}} \\ D &= \frac{U_{ed}}{U_s}\Big|_{\text{Drained cochlea}} \end{aligned} \tag{3.2}$$

where it is assumed that the fixed stapes condition and drained cochlea condition approximate $U_s = 0$ and $P_s = 0$, respectively.

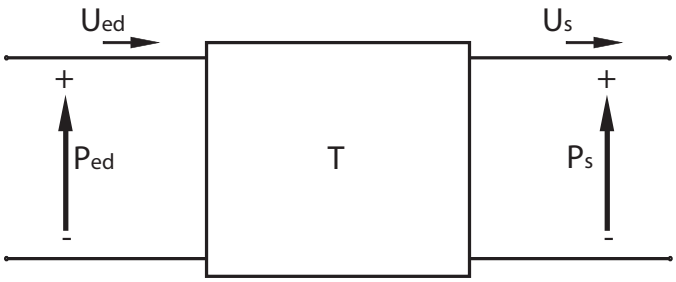

FIGURE 3.2. A two-port representation of the middle ear where P_{ed} is the pressure at the eardrum on the side of the ear canal, U_{ed} is the volume velocity of the eardrum, T represents the two-port middle-ear system (with parameters A, B, C, and D), U_s is the volume velocity of the stapes, and P_s is the pressure at the stapes footplate within the inner ear.

3.2.5 Background: Middle-ear forward pressure transfer function

While the A, B, C, and D matrix parameters provide a description of middle-ear function that is independent of termination loads, a more common measurement of middle-ear transmission is the forward pressure transfer function, G_{MEf}, defined as,

$$G_{MEf} = \frac{\overrightarrow{P_s}}{\overrightarrow{P_{ed}}} \tag{3.3}$$

where the rightward arrows indicate that the value is measured in the forward direction (i.e., when the middle ear is driven by pressure in the ear canal). The forward pressure transfer function is a useful measure of middle-ear sound transmission since in normal hearing, sound travels from the ear canal into the cochlea. As such, several groups have measured G_{MEf} for the chinchilla middle ear[9,11,12,13,71,14]: in this study, these measurements are compared to the model predictions of G_{MEf}. Note however, the forward-pressure transfer function, G_{MEf}, does not fully characterize middle ear function: to do so, G_{MEf} must be combined with additional measurements of the middle ear in the reverse direction (such as the reverse pressure transfer function or the reverse middle-ear impedance, discussed further in Ref. 61).

3.3 Modeling the chinchilla middle ear

Each component of the chinchilla middle ear was modeled by (1) selecting a previously published model of the middle-ear component of another mammalian species whose topology best represents that of the chinchilla middle ear and by (2) altering features of these models in order to best

represent known properties of the chinchilla middle ear and to be able to reproduce features seen in experimental data of the chinchilla middle ear. In this section, the selection of these models is discussed and a description of each component model is provided. Modification of model parameters is discussed in the following section.

3.3.1 Chinchilla middle-ear model: overview

A block diagram of the entire ear as modeled in this section is seen in Figure 3.3. The transformers represent the transition from the acoustic to the mechanical domain (or vice versa) within the ear. Each block represents a component of the ear: the middle-ear model consists of the middle-ear cavity (MEC), eardrum (ED), and ossicular chain (OC) models. Additionally, the input pressure and the termination impedance in the forward direction are shown. As seen in Figure 3.3, the input for the forward direction is the pressure in the ear canal and the termination load is the cochlear input impedance, Z_c. Z_c is given by:

$$Z_c = \frac{\overrightarrow{P_s}}{\overrightarrow{U_s}} \tag{3.4}$$

As in Eq. 3.3, rightward arrows indicate that the value is measured in the forward direction.

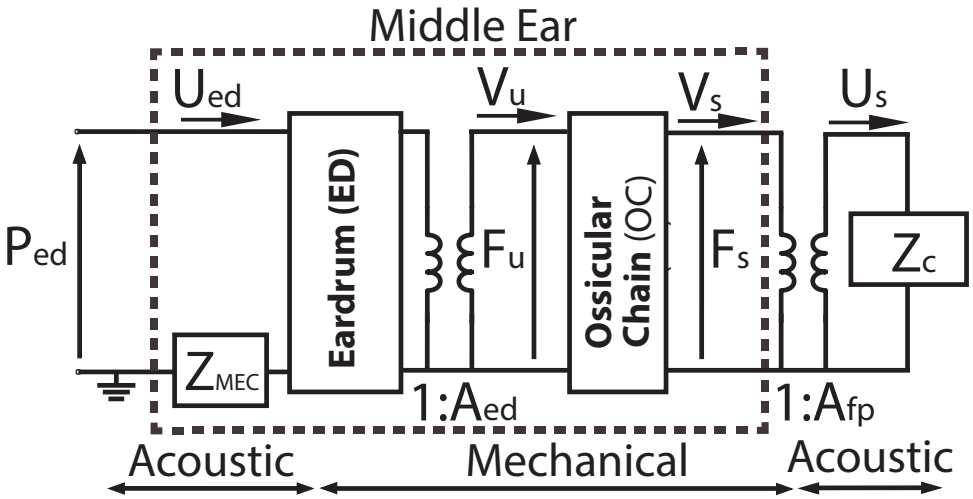

FIGURE 3.3. A block diagram of lumped parameter model of the middle ear. Here, P_{ed} and U_{ed} are the pressure and volume velocity in the ear canal (at the eardrum), respectively, Z_{MEC} is the impedance of the middle-ear cavity, F_u and V_u are the force and velocity at the umbo, respectively, F_s and V_s are the force and velocity at the stapes footplate, respectively, Z_c is the cochlear input impedance (as in Figure 11 of Ref. 21), U_s is the volume velocity at the stapes footplate, and A_{ed} and A_{fp} are the cross-sectional areas of the eardrum and stapes footplate, respectively.

3.3.2 Modeling the ossicular chain

The ossicular chain (the OC block in Figure 3.3) represents the lumped parameter model shown in Figure 3.4. The model of the ossicular chain is depicted as a simple electric circuit: force is represented as voltage and velocity is represented as current. Resistors, inductors and capacitors represent mechanical resistances, masses, and stiffnesses, respectively.

In the chinchilla middle ear, the malleus and incus are believed to be tightly fused[64,74]; in other words, the incudomalleolar joint (the magenta joint noted on Figures 3.1A-B) is thought to be extremely stiff. Thus, a model where the incus and malleus are modeled as a single lumped mass (as in Ref. 67), rather than a model that incorporates the flexibility of the incudomalleolar joint (such as the human model from Ref. 18 or the cat model from Ref. 8) was chosen. Thus, in Figure 3.4, M_m represents the rotational and translational inertia associated with this fused malleus-incus mass.

M_m is attached to a fixed point by a spring and a dashpot, K_m and C_m, which represent the stiffness and damping of the ligaments and muscle which support the malleus and incus (the tensor tympani muscle and the posterior incudal ligament, noted in purple on Figures 3.1A-B). K_{isj} and C_{isj} represent the stiffness and damping associated with the incudostapedial joint (the joint which connects the incus and stapes, noted in magenta on Figure 3.1A). Note that the mechanical advantage of the middle ear is represented as a transformer with a turns ratio of N_{lr}; the turns ratio, N_{lr}, represents the ratio of malleus velocity to incus velocity.

The stapes is the final bone of the ossicular chain which pushes the fluid within the cochlea: it can be seen in red on Figures 3.1A-B. Since the stapes primarily translates in a piston-like motion[75], M_s represents the actual mass of the stapes bone of the chinchilla. The stapes is connected to the bulla by the annular ligament and is supported by the stapedius muscle (both of which are noted in purple on Figures 3.1A-B); note the main source of stiffness and damping on the stapes is due to the annular ligament. The stiffness and damping associated with the annular ligament and stapedius muscle are represented by a spring and dashphot, K_{al} and R_{al}.

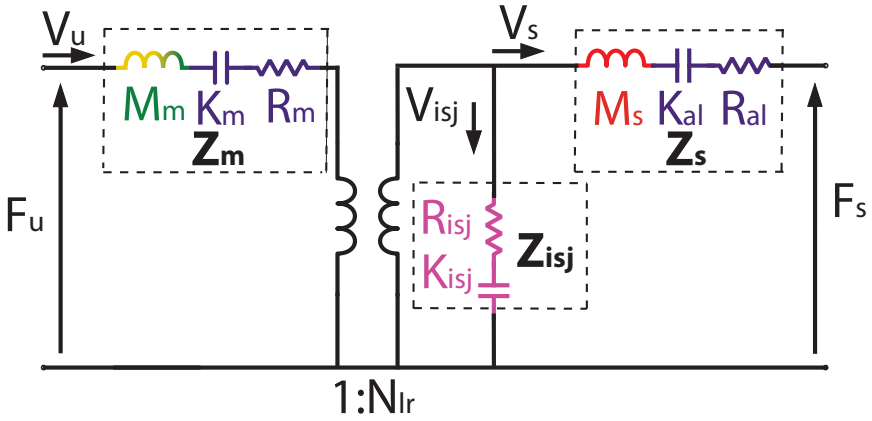

FIGURE 3.4. The ossicular chain model used in this study. Note all impedances in this model are mechanical impedances. In this model, the malleus and incus are fused, i.e. IMJ noted in Figure 3.1A-B is very stiff. V indicates a velocity; N_{lr} is the lever ratio of the middle ear; M, K, and R indicate lumped mass, stiffness, and resistance parameters, respectively; subscripts m, isj, s, and al indicate parameters belonging to the malleus, incudostapedial joint, stapes, and annular ligament, respectively; and Z indicates a mechanical impedance. Note that the color scheme used in this figure is the same as in Figure 3.1: as such, the fused malleus and incus mass is colored green and yellow. Additionally, the stiffness and damping associated with muscle and ligaments are colored purple while the stiffness and damping associated with the incudostapedial joint is colored magenta. The stapes mass is colored red.

3.3.3 Modeling the middle-ear cavity (MEC)

The load due to the middle-ear cavity (MEC) (represented as the Z_{MEC} block in Figure 3.3) is significant in the chinchilla middle ear[7]. The middle ear cavity is the space enclosed by the bulla, seen on Figure 3.1C. Opening the bulla, as was done in the experimental data used to fit the model parameters, can cause several changes in the response of the middle ear[6]. One notable effect of opening the bulla is the introduction of small resonances which can be seen in the experimental data[6,10]. Songer and Rosowski[6] used a simple model of cavity resonance to explain this observed phenomenon where the air within the cavity was modeled as an acoustic compliance, K_{cav}, and the mass of the air within the neck of the cavity was modeled as an acoustic mass, M_{hole}. A similar model of the load due to the middle ear was chosen in this study, given in Figure 3.5. In this study, however, the radiation resistance of the open hole in the bulla (as in Ref. 8), R_{hole}, is also included. Note that this model was chosen in order to best represent the condition of the middle ear in the experimental data, rather than the middle-ear cavity in its natural state.

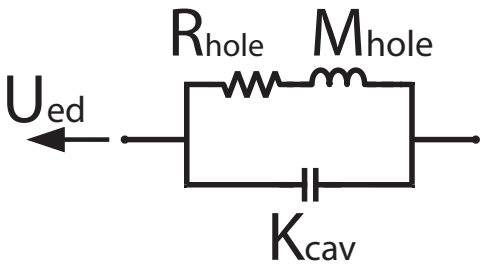

FIGURE 3.5. Model of the chinchilla middle-ear cavity where the bulla has been opened with a small hole (all impedances in this model are acoustic impedances). Here, U_{ed} is the volume velocity of the eardrum; K_{cav} is the stiffness due to the air in the main middle-ear cavity[6]; M_{hole} is the effective acoustic mass of the open hole in the bulla[6,7]; R_{hole} is the radiation resistance of the open hole in the bulla[8].

3.3.4 Modeling the eardrum

Two different models of the eardrum are considered. In one model, the eardrum is modeled as a one-dimensional cylindrical lossless acoustic transmission line with characteristic impedance Z_{ed} and a propagation delay T_{ed}, as in Refs. 8, 18. The transmission line model can be represented in terms of a two-port matrix as in Ref. 8,

$$\begin{Bmatrix} P_{ed} \\ U_{ed} \end{Bmatrix} = \begin{bmatrix} \cos(\omega T_{ed})/A_{ed} & iZ_{ed}A_{ed}\sin(\omega T_{ed}) \\ iZ_{ed}^{-1}\sin(\omega T_{ed})/A_{ed} & A_{ed}\cos(\omega T_{ed}) \end{bmatrix} \begin{Bmatrix} F_u \\ V_u \end{Bmatrix} \tag{3.5}$$

where F_u and V_u are the force and velocity of the umbo. The middle-ear model with the transmission line model of the eardrum (referred to as "the TL model" in the remainder of this thesis), best captures certain effects of the eardrum on normal sound transmission. However, at low frequencies, the additional complexity introduced by this model is often unnecessary to model the mechanics of the system, and thus another model, in which the eardrum is modeled as a rigid mass lumped with the mass of the malleus and incus, was also considered (this model is referred to as "the noTL model"). Two sets of parameters are given: one set of parameters for the TL model, and one set for the noTL model.

3.3.5 Cochlear Input Impedance

While the focus of this study was to model middle-ear mechanics, termination impedances are needed so that the model can be compared to most existing experimental data. In the forward direction, the termination impedance is the cochlear input impedance. The cochlear input impedance, Z_c from Ref. 9, found by directly measuring the pressure in the scala vestibuli and the velocity of the stapes, was coupled directly with the chinchilla ear models.

3.4 Fitting model parameters to experimental data

In the previous section, the selection and modification of previously published models which best represent the topology of the chinchilla middle ear is discussed. In each of these models, the model parameters must be adjusted to represent known properties of the chinchilla middle ear and to best capture experimental data for the chinchilla middle ear. Some alterations to model parameters are based on known differences between the chinchilla middle ear and the previously published model: for example, the mass of the stapes in chinchillas is different than that of the human and can be directly input into a lumped parameter model of the human ossicular chain from Ref. 67. For other parameters, the differences between species are unclear. Finding the values of these parameters is not trivial as there are 11 total free parameters for the noTL model and 13 for the TL model (the mass of the stapes, M_s and the area of the stapes footplate A_{fp} are based on physiological values and are considered known). It was found that some form of fitting methodology was required in order to find the values of these values of the parameters of the model which allow the model to reproduce the features seen in experimental data for the chinchilla middle ear.

In this section, I develop manual procedures for finding parameter values for the noTL and the TL middle-ear models. An automated error minimization algorithm was not used to fit the parameters: as in a previous paper[18], manual fitting procedures were chosen because they allowed the models to be fit to specific qualitative features of the data rather than obtaining an overall quantitative fit. Furthermore, the developed manual procedures make it possible to gain insight into the role of the different components of the model. This is particularly true for the noTL Model Fitting procedure, where analytical expressions relating model parameters to features captured in the experimental data can be derived.

To help readability of the following sections, a description of each parameter discussed in this section is provided in Table 3.1.

TABLE 3.1. Description of each parameter discussed in Section 3.4.

A_{ed}	Effective area of the eardrum (barrier between ear canal and middle ear)
A_{fp}	Effective area of the stapes footplate (barrier between middle ear and inner ear)
N_{lr}	Lever ratio of the middle ear
M_m	Mass representing the inertial effects of the fused malleus and incus
K_m	Stiffness of ligaments & muscle which connect M_m to bullar wall
R_m	Damping associated with ligaments & muscle which connect M_m to bullar wall
K_{isj}	Stiffness of incudostapedial joint (joint which connects incus to stapes)
R_{isj}	Damping associated with incudostapedial joint (joint which connects incus to stapes)
M_s	Mass of the stapes (final bone in ossicular chain)
K_{al}	Stiffness of ligaments & muscle which connect M_s to bullar wall (dominated by annular ligament)
R_{al}	Damping associated with ligaments & muscle which connect M_s to bullar wall (dominated by annular ligament)
M_{hole}	Effective acoustic mass due to the hole in the bulla
K_{cav}	Effective stiffness due to the air in the main middle-ear cavity
R_{hole}	Radiation resistance of the open hole in the bulla
T_{ed}	Propagation delay of the TL model of the eardrum
Z_{ed}	Characteristic impedance of the TL model of the eardrum

3.4.1 noTL Model Fitting procedure

A method for fitting parameters of the noTL model to experimental two-port transmission matrix parameter data from Ref. 10 is described in this section; this simple, manual fitting procedure could be used to develop similarly structured lumped parameter models of the middle ear for other mammals. When fitting models, it is generally preferable to use direct experimental measurements. However, two-port transmission matrix parameter data, while obtained indirectly (as was done in Ref. 10), allows for characterization of the middle ear independent of influence from the termination loads[72]. Because ear canal and cochlear loads vary by species and by experimental set-up, it is desirable to fit a middle-ear model to a set of data that excludes these influences. Additionally, simple expressions for A, B, C, and D in terms of lumped parameter model elements can be found in the case of the noTL model: these simple expressions make it possible to adjust the lumped parameter elements in a straightforward manner to improve the fit between the model and experimental data.

Before fitting model parameters, A_{ed}, A_{fp}, and N_{lr} were fixed to constant, real values. The value used for N_{lr} (3.7) is similar to measured and computational results of the anatomical lever

ratio (where N_{lr} is defined as the ratio of the length of the malleus lever arm to the length of the incus lever arm): N_{lr} = 2.84, 3.66 and 3.76 in Refs. 68, 76, and 60, respectively. The value for A_{ed} ($A_{ed} = 80mm^2$) was chosen so that at frequencies between 170 and 1,200 Hz, the effective area (defined here as the ratio of the volume velocity in the ear canal to the velocity of the umbo, U_{ec}/V_u) in the noTL model was similar to the ratio of the value of U_{ec}/V_u (shown in Figure 6.18 in Ref. 74) which was calculated based on measurements from Refs. 77, 78. This value is slightly larger than the measured value of the chinchilla pars tensa area reported by Vrettakos et al.[68] to be 60.44 mm^2; however, in several species including the chinchilla, the effective area is larger than the anatomical area of the eardrum[74]. Within the frequency range for which the value of A_{ed} was chosen, 170-1,200 Hz, the ear canal volume velocity to umbo velocity ratio magnitude calculated from experimental data is relatively flat; because the effective area of the noTL model is real and frequency independent while the actual effective eardrum area is complex and frequency dependent[74], the noTL model can only represent the eardrum effective area well at these frequencies (170-1,200 Hz). In the TL model, however, the ratio U_{ec}/V_u is complex and varies with frequency at frequencies above 1.2 kHz: the value of A_{ed} in Eq. (3.5) for the TL model was chosen to be equal to the value of A_{ed} chosen for the noTL model. The value for A_{fp} (in both models) was chosen to be equal to the value of the stapes footplate area in the chinchilla as reported by Vrettakos et al.[68].

After fixing the values of A_{ed}, A_{fp}, and N_{lr} as scalars, the model is simultaneously fit to both the two-port matrix parameters and their transformed values. The transformed values of A, B, C, and D are defined by the following equation:

$$\begin{Bmatrix} P_{ed} \\ U_{ed} \end{Bmatrix} = \begin{bmatrix} A_T & B_T \\ C_T & D_T \end{bmatrix} \begin{Bmatrix} P_{sT} \\ U_{sT} \end{Bmatrix} \tag{3.6}$$

where P_{sT} and U_{sT} are the "transformed" effective pressure and volume velocity at the stapes footplate. As defined by O'Connor and Puria[18], these transformed values correspond to the values that are obtained when the effect of the transformers seen in Figure 3.3 are absorbed by the parameters, as shown in Figure B.1 in Appendix B (the relationships between the untransformed variables and the transformed variables are given in the caption of Figure B.1).

The transformed two-port transmission matrix parameters can be expressed as a function of

the impedances of the noTL lumped parameter model. The procedure for relating the transformed two-port transmission matrix parameters, A_T, B_T, C_T, and D_T, to lumped parameter elements is detailed in Appendix B and the resulting equations are seen below:

$$\begin{aligned} A_T &= \frac{Z_{mT} + Z_{MEC}}{Z_{isjT}} + 1 \\ B_T &= \frac{(Z_{mT} + Z_{MEC})Z_{sT}}{Z_{isjT}} + Z_{mT} + Z_{MEC} + Z_{sT} \\ C_T &= \frac{1}{Z_{isjT}} \\ D_T &= \frac{Z_{sT}}{Z_{isjT}} + 1 \end{aligned} \tag{3.7}$$

where, as in Figure B.1, a T in the subscript denotes a "transformed" parameter.

The expressions for A_T, B_T, C_T, and D_T in Eq. (3.7) provide the basis for the noTL fitting procedure. Before beginning the procedure, the ossicular chain stiffness parameter values were set to that of a model of the guinea pig middle ear that I had developed previously to couple with a model of the inner ear[1]. The values for the damping parameters were all initially set to the value used in Ref. 1 for the annular ligament damping parameter. The mass parameter values for the combined malleus/incus and for the stapes were set equal to, respectively, 80% and 100% of the mass values reported for the chinchilla ossicular chain in Ref. 70. The specific amount of 80% of the actual malleus/incus mass is arbitrary. However, Puria and Steele[64] noted that in several published circuit models, the malleus and incus mass parameter values are smaller than their corresponding measured masses; this disparity was attributed to the fact that the actual physiological motions of the ossicles tend to be rotational rather than translational, particularly at higher frequencies[64]. The initial values for the MEC parameters are discussed in further detail in Ref. 61; briefly, they are based on known quantities of the volume of the middle-ear cavity and size of the middle-ear cavity hole.

Using these initial parameters, steps were taken to fit the noTL model which are listed in the procedure given below. In order to follow the procedure, it is helpful to look at Figure 3.7 which is shown with the model results in Section 3.5.

1. In Eq. (3.7), if the effective area of the eardrum is assumed constant and real, it can be

seen that C_T depends only on the incudostapedial joint impedance, Z_{isjT}. Before fitting other parameters, the value of K_{isj} was adjusted such that the model's resulting C magnitude matches the magnitude of the C data at low frequencies

2. In the noTL model, D_T depends only on Z_{isjT} and the stapes and annular ligament impedance, Z_{sT}. Since a value for K_{isj} was chosen in step 1 of the procedure, the value of the annular ligament stiffness, K_{al}, was adjusted so that the model's resulting D magnitude matches the magnitude of the D data below 1 kHz

3. At this step, the effect of the MEC is ignored by setting $Z_{MEC} = 0$. With this assumption, B_T is only a function of Z_{isjT}, Z_{sT}, and the malleus impedance, Z_{mT}. Since values were found for K_{isj} and K_{al} in steps 1 and 2, the value of the malleus stiffness, K_m, was adjusted to improve the model fit data for B_T at low frequencies. A_T could potentially have been used to find a value for K_m, but using B_T was preferred because the values of B reported in Ref. 10 only required two measurements (of the ear canal pressure and stapes velocity) whereas A was found indirectly using a large number of measurements and required an assumption of reciprocity. It was found that there was a trade-off between adjusting K_m so that

   (a) the model results best match the magnitude of the B data at low frequencies (between 100 and 300 Hz)

   (b) the frequency of the minimum in the model's B magnitude matches the frequency of minimum in the magnitude of B (400 Hz)

   K_m was chosen to be equal to the average value found with the two different fitting methods listed above.

4. While still ignoring the effect of the MEC, the values of the three ossicular damping parameters (R_m, R_{isj}, and R_{al}) were adjusted (while maintaining $R_m = R_{isj} = R_{al}$) so that the model matched the depth of minimum of the B magnitude data at 400 Hz

5. At this step, the MEC is taken into account and the value of the MEC mass parameter, M_{hole}, was adjusted to fit the frequency of the peak in the B magnitude data at 2.5 kHz.

6. By adjusting the MEC resistance, R_{hole}, it was found that there was a trade-off between adjusting R_{hole} so that the model results best match

   (a) the height of the peak in B magnitude data at 2.5 kHz

   (b) the depth of the notch in B phase data at 2.6 kHz

   R_{hole} was chosen to be equal to the average value found by adjusting R_{hole} to match each of the features listed above.

The parameter values after each step are listed in Table 3.2. The resulting model fits are given in the Results Section.

3.4.2 TL Model Fitting procedure

While the noTL model is simple to fit and works well at low frequencies, a more complex model of the eardrum (the TL model described in Section 3.3) was found to be necessary in order to improve the model's high frequency forward pressure transfer function, G_{MEf}, phase results. The addition of the TL model of the eardrum adds significant complexity to the expressions for A_T, B_T, C_T, and D_T; furthermore, experimental data for the two-port transmission matrix parameters only extends to 8 kHz. Hence, a different fitting procedure was developed for the TL model. The TL model parameters were adjusted using experimental measurements of G_{MEf} from Ref. 9: these measurements were taken at frequencies between 62.5 Hz and 28.5 kHz which is similar to the hearing range of the chinchilla[69].

Before beginning the procedure, all middle ear cavity and ossicular chain parameters excluding the malleus mass were set to the noTL model parameter values. The eardrum delay, T_{ed}, was initially set equal to the delay found for a cat TL model[8]. The malleus mass parameter value was reduced to 10% of the value of the malleus mass found for the noTL model. As in the noTL model, the specific amount of 10% of the noTL model malleus mass value is arbitrary: however, as was found in previous models with a TL model of the eardrum[8,18], a small malleus mass parameter was needed in order to reduce reflections in the model simulations at high frequencies.

In a circuit model of the cat middle ear with a lossless transmission line model of the eardrum, Puria and Allen noted that a carefully selected stiffness element may be placed after each mass

element such that a section of a "matched" transmission line is formed by the two elements[8]. In the model described in this paper, the transformed combined malleus and incus mass, M_{mT}, has a corresponding transformed shunt stiffness of K_{isjT}; as in Ref. 8, these two elements may be viewed as one segment of a lumped parameter transmission line. In order to reduce reflections due to impedance mismatch between the eardrum and the ossicular chain, the characteristic impedance of the eardrum, Z_{ed}, was initially set equal to the local characteristic impedance of M_{mT} and K_{isjT}, $Z_{char}^{OC} = \sqrt{M_{mT}K_{isjT}}$.

Using the initial parameters described in the proceeding two paragraphs, the following steps (shown in Figure 3.6) were taken to fit the TL model:

1. Adjust T_{ed} so that that the frequency of the sharp peak in the model response (marked with a magenta arrow labeled "+" in Figure 3.6A) matches the frequency of the peak in G_{MEf} magnitude data at 22.6 kHz (marked with a blue arrow labeled "o" in Figure 3.6A).

2. Increase Z_{ed} so that at frequencies between 2-10 kHz, the model's G_{MEf} magnitude results lie within the 95% confidence interval of the data and re-adjust T_{ed} such that the high frequency peak in model's G_{MEf} magnitude matches the frequency of the peak in the data at 22.6 kHz (marked with a blue arrow labeled "o" in Figure 3.6A).

3. Adjust M_{hole} so that the frequency of the notch in the model's G_{MEf} magnitude matches the frequency of the notch in the G_{MEf} magnitude data at 2.5 kHz and R_{hole} so that the model's G_{MEf} magnitude results match the magnitude of the notch in the G_{MEf} data at 2.5 kHz. The notch in the G_{MEf} magnitude data at 2.5 kHz is noted with a green arrow labeled "x". After M_{hole} and R_{hole} are chosen, re-adjust T_{ed} to match the frequency of the peak in G_{MEf} magnitude at 22.6 kHz

4. It was found that R_m influences both (1) the height of the high frequency peak in the G_{MEf} magnitude (highlighted in step 1 with a magenta arrow in Figure 3.6A) and (2) the drop in the G_{MEf} phase found between 20-22 kHz (noted with an orange arrow labeled "*" in Figure 3.6B). Adjusting R_m such that the model results exactly match the G_{MEf} phase at high frequencies while simultaneously remaining within the 95% confidence intervals of the G_{MEf} experimental measurements was found to be impossible. Thus, R_m was chosen to be equal to

the average of the value found with the following methods:

(a) Increase R_m to reduce the model's high frequency peak in the G_{MEf} magnitude so that the results lie within the 95% confidence interval of the data

(b) Adjust R_m so that the model results best match the G_{MEf} phase data between 20-22 kHz

The parameter values after each step are listed in Table 3.3.

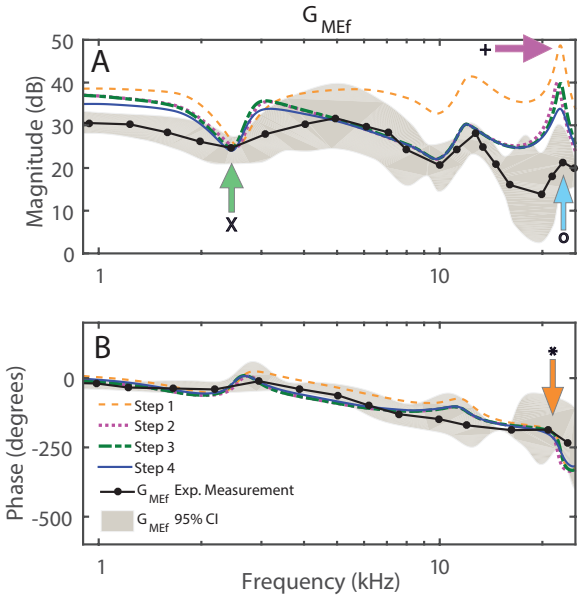

FIGURE 3.6. Chinchilla TL model results after each step in the TL model fitting procedure versus experimental G_{MEf} measurements[9]. The 95% confidence intervals of these measurements are plotted in gray. Arrows indicate notable features in the G_{MEf} model results and measurements that were used to adjust the TL model parameters (described in more detail in the TL model fitting procedure).

3.5 Middle-ear circuit model: results

In this section, the model predictions for (1) A, B, C and D and (2) the forward pressure transfer function (the pressure gain at the stapes footplate from pressure input in the ear canal), $G_{MEf} = P_s/P_{ed}$, are given. Since the TL model was fit to forward pressure transfer function data, its A, B, C and D results can be used to validate the model. Similarly, since the noTL model was fit to experimental data for B, C and D, both its forward pressure transfer function and A results can

be used to validate the model. Both models are compared against with additional data sets in Ref. 61.

3.5.1 Model predictions of A, B, C, and D

Figure 3.7 displays the model simulations for both middle-ear models (the TL model and the noTL model) compared to the experimental data for A, B, C and D from Ref. 10. Neither middle-ear model was fit directly to A experimental data. Still, both models are able to capture several notable characteristics seen in the A data (panels A and E in Figure 3.7): the markedly flat magnitude and phase in A at frequencies below 1 kHz, the notch in the A magnitude data (marked with a red arrow labeled "*" in Figure 3.7A) and corresponding peak in the A phase data at 2 kHz, the peak in the A magnitude data (marked with a blue arrow labeled "+" in Figure 3.7A) and corresponding notch in the A phase data at 2.5 kHz, and, qualitatively, the notch in the A magnitude data marked with a green arrow labeled "o" in Figure 3.7A. However, the frequency of the notch (marked with a green arrow labeled "o") in the A magnitude predicted by each model (3.1 kHz and 3.5 kHz in the noTL and eardrum models, respectively) is lower than the frequency of the notch seen in the data (3.8 kHz); furthermore, the notch in the data is deeper than what is predicted by either of the models. Additionally, as seen in Figure 3.7E, both models predict a flat response in the phase at frequencies above 4 kHz while the A phase data begins to decrease at frequencies above 4 kHz. However, despite these discrepancies at high frequencies, overall, both models fit the magnitude and phase of A quite well at frequencies below 3 kHz.

The noTL model represents both the magnitude and phase of the B data better than the TL model throughout the frequency range of the data (panels B and F in Figure 3.7); this is expected since the noTL model parameters were specifically adjusted to fit this data while the TL model parameters were re-adjusted to improve the agreement between simulations and experimental data for G_{MEf} at high frequencies. The noTL model predicts a minimum in the B magnitude at 440 Hz and the TL model predicts a B magnitude minimum at 540 Hz: a minimum in the B magnitude data is seen at 400 Hz (marked with an orange arrow in Figure 3.7B). Thus, while noTL model better captures the frequency of this minimum seen in the experimental data, the values predicted by both models for the frequency of this minimum are reasonable. The noTL model is able to match the depth of the minimum in the B magnitude data much better than the TL model. This is due

to the extra damping in R_m needed in the TL model in order to damp out peaks in predicted value of G_{MEf} which are caused by an impedance mismatch between the transmission line model for the eardrum and the ossicular chain. There is a peak in the A and B experimental data and the model results at around 2.5 kHz (marked with a blue arrow labeled "+" in Figure 3.7A and a black arrow labeled with a square in Figure 3.7B). As mentioned previously, the peak in the experimental data at this frequency was attributed to an anti-resonance produced by open holes in the bulla: in both models, matching these features seen in the data required a middle-ear cavity model.

At low frequencies, both models match the C magnitude data very well (Figure 3.7C). However, at frequencies above 2 kHz, the models predict a continued increase in magnitude while the experimental data begins to decrease. As in the data, the magnitude of D remains relatively flat below 3.5 kHz in both models (Figure 3.7D). As seen in Figure 3.7H, the experimental phase for D rises sharply at high frequencies: while the TL model begins to increase at around 10 kHz, neither model is able capture the trend seen in the high frequency phase data for D.

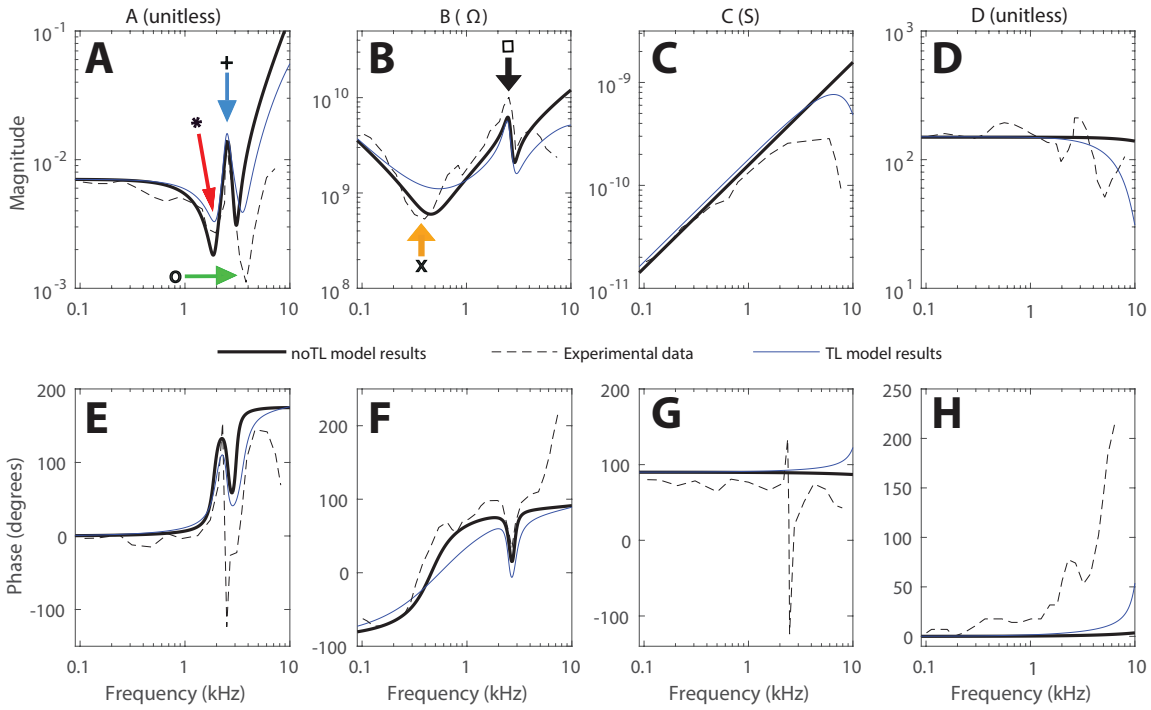

FIGURE 3.7. Chinchilla middle-ear model results versus experimental A, B, C, and D magnitude and phase data. The magnitudes for each two-port parameter are given in the upper sub-figures, A-D, and the phases are given in the lower sub-figures, E-H. The TL model is plotted with thin blue lines. The noTL model is plotted with thicker black lines. Dashed lines indicate experimental data[10].

3.5.2 Model predictions of G_{MEf}

Measurements of the forward pressure transfer function, G_{MEf}, in the chinchilla middle ear have been reported by multiple groups and published in several different papers[9,11,12,13,71,14]. In addition, G_{MEf} can be calculated using experimental data for the velocity transfer function (the velocity of the stapes relative to the pressure in the ear canal) from Ref. 10 and experimental measurements of Z_c from Ref. 9. Results for the TL and noTL models are compared to these calculated G_{MEf} data and to several experimental G_{MEf} measurements[9,11,12,13,14].

Qualitatively, all experimental G_{MEf} data sets compared are relatively consistent[14]. The magnitude of all G_{MEf} data sets compared increases with frequency up until it reaches a maximum at frequencies between 250-600 Hz. There is a notch in the magnitude data (and corresponding peak in the phase data) at approximately 2.3-2.8 kHz for all data sets except the Decory et al. 1990 measurements. At frequencies higher than 10 kHz, both the magnitude and the phase data decrease with increasing frequency. Overall, all available experimental data for G_{MEf} suggest that the chinchilla middle ear behaves as a broadly tuned bandpass filter. There are, however, quantitative differences as large as 27 dB in the amplitude between some of the data sets that tend to increase the pressure by 20 to 40 dB across most of the frequency range. In particular, at most frequencies, the G_{MEf} magnitude reported in Ref. 12 is approximately 10-20 dB lower than the magnitudes of the other G_{MEf} data sets. Chhan et al. speculate that this difference might be due to their placement of the scala vestibuli sensor[12].

Both the TL and noTL middle-ear models match the experimental data well throughout the majority of the frequency range. At frequencies between 100 Hz and 15 kHz, the G_{MEf} magnitude results from both models agree with the G_{MEf} magnitudes measured by Refs. 9, 13, 14 and the calculated G_{MEf} data[10,9] . At frequencies above 15 kHz, the noTL G_{MEf} magnitude results resemble the G_{MEf} magnitudes measured by Refs. 14, 9, 11. However, while the TL model is able to capture the frequency of the 22.6 kHz peak seen in magnitude of the Slama et al. 2010 G_{MEf} measurements, quantitatively, it does not match the magnitude of the G_{MEf} data well at high frequencies. The noTL model is not able to match the G_{MEf} phase data at frequencies above 10 kHz whereas the TL model phase predictions better fit the data.

Despite discrepancies between the data and the models at high frequencies, both models match

the data well at frequencies lower than 15 kHz and capture several notable characteristics seen in the G_{MEf} data. In the magnitude results from both models, a maximum is seen which resembles the maximum seen in the G_{MEf} magnitude data at frequencies between 250-600 Hz: the TL model's maximum occurs at a higher frequency (approximately 900 Hz) and the noTL model predicts a maximum at approximately 400 Hz. Both models' magnitude results reproduce the notch in the data seen at frequencies between 2.3 and 2.6 kHz. In the model, the notch is due to resonance between the compliance of the air in the MEC and the bulla hole since this notch disappears with the impedance of the MEC is set to zero. Magnitude results from both models capture the notch at 10 kHz and peak at 12 kHz seen in the magnitude of the Slama et al. data[9]. Additionally, the phase results from both models include a peak at 2.6 kHz similar to the peak seen in the G_{MEf} phase data at frequencies between 2.3 and 2.8 kHz.

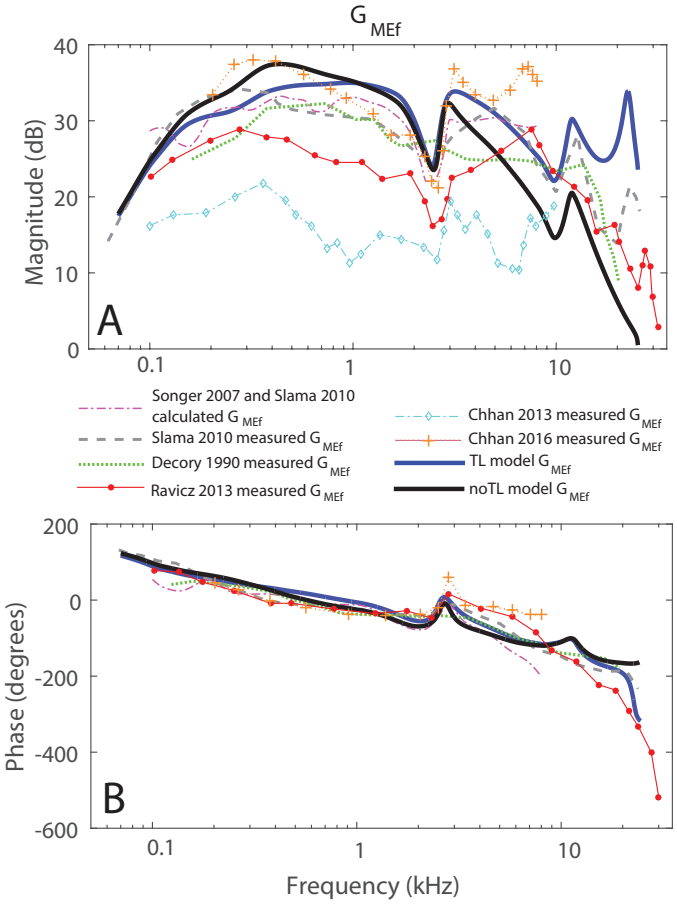

FIGURE 3.8. Chinchilla model versus experimental data for G_{MEf}. A. G_{MEf} Magnitude. B. G_{MEf} phase. Solid lines represent model predictions. Other other line types represent G_{MEf} data[10,9,11,12,13,14].

TABLE 3.2. NoTL model parameter values at each step in the fitting procedure. In the steps column, initial parameters are labeled as step "0" and "All" signifies that a parameter value remains the same throughout the fitting procedure. All parameter values are in MKS mechanical units (kg for mass parameters, N/m for stiffness parameters, and $N-s/m$ for damping parameters) unless noted with an "a" in the superscript in which case the parameter values are in MKS acoustical units (kg/m^4 for the mass parameter, N/m^5 for the stiffness parameter, and $N-s/m^5$ for the damping parameter). Parameters are defined in Figure 3.4

Parameter	**Steps**	**Parameter Value**
M_m	All	8.89×10^{-6}
K_m	0-2	30
	3-6	88
R_m	0-3	4.0×10^{-4}
	4-6	0.02
K_{isj}	0	340
	2-6	2.34×10^4
R_{isj}	0-3	0.03
	4-6	0.02
M_s	All	4.35×10^{-7}
K_{al}	0-1	5
	2-6	10
R_{al}	All	0.02
M_{hole}	0-4	246
	5-6	268
R_{hole}	0-5	1.60×10^6
	6	6.12×10^5
K_{cav}	All	7.00×10^{10}

3.6 Discussion

3.6.1 Strengths and limitations of the noTL and TL models and fitting procedures

In this chapter, two models of the chinchilla middle-ear, the TL and the noTL model, each with a separate set of fitting procedures and model parameter values, were presented. Both are provided since there are advantages to each model under different circumstances. The strengths and weaknesses of each model are discussed in this section in order to help a researcher who wishes to use one of the two models choose the better of the two models for their situation.

TABLE 3.3. TL model parameter values at each step in the fitting procedure. In the steps column, initial parameters are labeled as step "0." and "All" signifies that a parameter value remains the same throughout the fitting procedure. All parameter values are in MKS mechanical units (kg for mass parameters, N/m for stiffness parameters, and $N-s/m$ for damping parameters) unless noted with an "a" in the superscript in which case the parameter values are in MKS acoustical units (s for the delay parameter, kg/m^4 for the mass parameter, N/m^5 for the stiffness parameter, and $N-s/m^5$ for the damping and impedance parameters). T_{ed} and Z_{ed} are the eardrum delay and characteristic impedance, respectively. Ossicular chain and middle ear cavity parameters are defined in Figure 3.4

Parameter	**Steps**	**Parameter Value**
M_m	All	8.89×10^{-7}
K_m	All	88
R_m	0-3	0.02
	4	0.04
K_{isj}	All	23400
R_{isj}	All	0.02
M_s	All	4.35×10^{-7}
K_{al}	All	10
R_{al}	All	0.02
M_{hole}	0-2	268
	3-4	284
R_{hole}	0-2	6.12×10^5
	3-4	6.49×10^5
K_{cav}	All	7.0×10^{10}
T_{ed}	0	3.57×10^{-5}
	1	1.39×10^{-5}
	2	1.95×10^{-5}
	3-4	1.90×10^{-5}
Z^a_{ed}	0-1	6.09×10^6
	2-4	3.65×10^7

The simplest of these two models is the noTL model: in this model, the eardrum is modeled as a rigid mass lumped with the incus and malleus masses. The two-port transmission matrix parameter equations for the noTL model make it relatively straightforward to fit the parameters to experimental A, B, C, and D data and to analyze each parameter's effect on the model's response. As detailed in Ref. 61, at frequencies below 10 kHz, the noTL model fits experimental data for the forward and reverse transfer functions of the middle ear quite well in multiple conditions for the termination loads.

At frequencies above 19 kHz, the phase of the forward pressure transfer function experimental measurements[9,14] decreases with frequency: using the simple noTL model, it was impossible to match this trend in the data. The inability of the noTL model to match the G_{MEf} experimental phase data at high frequencies could be due to the use of a simplistic ossicular chain model: although the malleus and incus are tightly fused in the chinchilla middle ear, it is possible that there is relative motion between the two bones at high frequencies similar to the flexibility of the malleo-incudo articulation observed in the guinea pig[79] (whose malleus and incus are also tightly fused[80]). Alternatively, the rotation of these bones could be more complex at high frequencies. These more complicated vibrational responses of the ossicular chain were not considered in this study. In order to improve the predictions for phase of G_{MEf} at high frequencies, a second model which included a lossless TL model of the eardrum (as in Refs. 8, 18) was developed; its parameters were adjusted using available measurements for the forward pressure transfer function at high frequencies.

The TL model has several advantages over the noTL model: the TL model is able to capture the trend of the forward pressure transfer function phase data at high frequencies, can represent the propagation delay in the sound traveling through the eardrum, and allows for constructive or destructive interference within the eardrum[18]. However, while the TL model better captures the phase of G_{MEf} experimental measurements at high frequencies, it does not capture the magnitude very well. This is likely due to the assumption of impedance matching: a TL transmission line model of the eardrum perfectly matched to the ossicular chain transmission line would result in a flat, broadband G_{MEf} magnitude response, unlike the experimental G_{MEf} magnitude data which decreases sharply at high frequencies. However, if the impedance mismatch at the eardrum is too high, the TL model produces large peaks in the G_{MEf} magnitude. The inability of the TL model to simultaneously match both the amplitude and phase of the forward pressure transfer functions

at high frequencies might be due the fact that the TL model simplifies many aspects of eardrum motion. The complex motion of eardrum vibration has been studied since the 1970s[81] and has been the focus of active research in recent years[65,66]: while many finite element models have been developed in an effort to simulate and study eardrum motion, such models were not used in this study in the interest of simplicity. In order to match both the phase and magnitude of the G_{MEf} data for the chinchilla at frequencies higher than 16 kHz, a more realistic model of the eardrum that captures its complex motion at high frequencies[65,66] might be needed.

With the introduction of the TL model of the eardrum, the expressions for A, B, C, and D in terms of model elements become quite complex making the model more difficult than the noTL model to analyze. Additionally, at low frequencies, the noTL model fits the majority of the experimental data better than the TL model. Because each model has its own set of strengths and weaknesses as discussed above, both models were included in this chapter. If using the model at high frequencies, particularly if using the model in a situation where the group delay through the middle ear is important, it is recommended that the TL model is used. Otherwise, at low to mid-range frequencies, the noTL model works well in representing the input and output relationships of the chinchilla middle ear in normal hearing conditions.

The experimental data for A, B, C, and D[10] includes features (particularly at high frequencies) that neither the noTL model nor the TL model are able to match. By examining Eqs. 3.7 and adjusting parameters, the general shape of the model's A, B, C, and D response can be found and it becomes apparent which features of the data are able to be represented in the model results. Certain features of the data that the noTL and TL models are not able to represent, such as the maximum in the D magnitude at 3 kHz or the phase discontinuity in the C data at 2.5 kHz, could be due to aspects of middle-ear function that the models cannot capture. A middle-ear model that allows for relative motion between the incus and malleus at high frequencies, more complex rotational motion of the ossicles at high frequencies, or that captures modal motion of the eardrum might be able to match these features.

3.6.2 Importance of the existence of multiple experimental data sets for middle-ear mechanics

In this chapter, a simple procedure for fitting the chinchilla middle-ear model to experimental data for A, B, C, and D matrix parameters was outlined. This procedure can be extended to fit 2-DOF lumped parameter middle-ear models for other mammals; however, in order to use this procedure, a full set of experimental data for the inputs and outputs of the middle ear is needed. While A, B, C, and D matrix parameters were found by measuring P_{ed}, U_{ed}, and U_s in various cochlear conditions in Ref. 10, the matrix parameters can also be determined by measuring G_{MEf}, G_{MEr}, Z_{MEr}, and the termination impedances in both directions[72,16]. Finding the two-port transmission matrix parameters by draining the cochlea and fixing the stapes fully characterizes the middle ear's input and output relationship with relatively few measurements—if this experimental data existed for other animals, middle-ear models for these animals could be developed relatively quickly. For example, there is not as much experimental data for the gerbil or mouse middle ears, making the middle-ear model development for these animals difficult. Additionally, measurements of A, B, C, and D matrix parameters using the methods described in Ref. 10 could be used to calculate G_{MEf}, G_{MEr}, Z_{MEr}, and Z_{me}; these calculated results could compared against measurements of G_{MEf}, G_{MEr}, Z_{MEr}, and Z_{me}. By comparing these two sets of data (each found through different experimental methods), both experimental results could be verified; problems and inconsistencies with the measurements, if present in the data, could potentially be identified.

3.6.3 Comparison of chinchilla, guinea pig, cat, and human middle-ear transformed two-port transmission matrices

In the previous section, expressions were given which analytically relate the chinchilla middle-ear circuit model parameters to two-port transmission matrix parameters, A, B, C, and D. Since experimental data for A, B, C, and D exist for multiple species, this section aims to employ the foregoing analytical expressions for A, B, C, and D to extract information about the compliance of the ossicular joints of these species.

The transformed two-port transmission matrix elements are defined in Eq. 3.6: this definition assumes that the effective area of the eardrum and the lever ratio remain real and constant

throughout the frequency range. This is a simplification of middle-ear function, particularly at high frequencies. Thus, the most insightful components of any A_T, B_T, C_T, and D_T comparison will be from low frequency examination.

On Figures 3.9A-H, A_T, B_T, C_T, and D_T results for the chinchilla TL model are compared with Meaud and Lemons' model[1] of the guinea pig middle ear coupled with a TL model of the eardrum (detailed in Appendix B), O'Connor and Puria's model of the human middle ear[18], and Puria and Allen's model of the cat middle ear[8]. Chinchilla[10], human[16], and cat[15] experimental A_T, B_T, C_T, and D_T data are shown in on Figures 3.9I-P. The A_{ed}, A_{fp}, and N_{lr} values used for each species are given in Table 3.4. Comparing the model results for A_T, B_T, C_T, and D_T on Figures 3.9A-H with experimental data on Figures 3.9I-P, it is seen that the models are generally consistent with experimental data. For these four species, A_T, B_T, C_T, and D_T are qualitatively similar: for all species compared, the A_T magnitudes remain relatively flat before decreasing to a minimum between 1 and 5 kHz and subsequently increasing sharply with frequency, the B_T magnitudes decrease to a minimum between 400 Hz and 1 kHz, the C_T magnitudes have relatively constant slope (on the logarithmic plot) at low frequencies, and the D_T magnitudes decrease to a minimum between 2 and 11 kHz before increasing sharply with frequency.

While A_T, B_T, C_T, and D_T are qualitatively similar between species, there are quantitative differences in the numerical results; the amplitudes of A_T, B_T, C_T and D_T tend to be higher in humans than in other species while the amplitude of C_T tends to be lower in the guinea pig than in other species. Differences in the amplitude values can be interpreted physically by examining Eqs. 3.7 where expressions relating A_T, B_T, C_T and D_T to the noTL model's lumped parameter elements are given. While these expressions were not developed for the TL model, at low frequencies, the response of the model is stiffness-dominated and the effects of the eardrum are negligible: thus, the following discussion will be limited to frequencies below 1 kHz where these expressions are sufficient to characterize the TL model.

Since the guinea pig and chinchilla middle-ear models used in this discussion share the same topology, Eqs. 3.7 can be directly applied to the chinchilla and guinea pig TL models at low frequencies. In these two species, the malleus and incus are tightly fused[68,80,64] and the incus and malleus are modeled as a single lumped mass. The chinchilla and guinea pig middle-ear models compared in this section will be referred to as two-degrees of freedom (2-DOF) models where the degrees of free-

dom correspond to the velocities of the two lumped masses (the combined incus/malleus mass and the stapes mass). The cat[8] and human[18] middle-ear models used in this comparison incorporate the flexibility of the incudomalleolar joint[82,83] in these species: these two models include both the incudostapedial joint stiffness, K_{isj}, and the incudomalleolar joint stiffness, K_{imj}. The human and the cat models compared here will be referred to as 3-DOF models where the degrees of freedom correspond to the velocities of the three lumped masses (the malleus, incus, and stapes masses).

The full A_T, B_T, C_T, and D_T expressions for the 3-DOF cat[8] and human[18] models are significantly more complex than the expressions given in Eqs. 3.7: if the numerical values of K_{isjT} and K_{imjT} are similar in a 3-DOF system, the 2-DOF equations in Eqs. 3.7 will provide little insight into the mechanics of the system. However, for both the cat and the human models in this comparison, the K_{imjT} values are an order of magnitude smaller than the K_{isjT} values which suggests that it is possible to approximate each as a 2-DOF system where the incus and stapes are assumed to be fused. For these approximate 2-DOF systems, the joint stiffness that has the biggest influence on the flexibility of the ossicular chain is the incudomalleolar joint stiffness. Hence, in the rest of this section, a transformed joint stiffness, K_{jT}, is discussed. K_{jT} refers to K_{imjT} in the case of the human and cat models; K_{jT} refers to K_{isjT} in the case of the chinchilla and guinea pig models. Using this notation, Eqs. 3.7 can be generalized to the approximate 2-DOF cat and human models by replacing K_{isjT} by K_{jT}.

Examining Eq. 3.7, it can be seen that for the 2-DOF and approximate 2-DOF models discussed above, at frequencies below 1 kHz, the magnitude of C_T is a function of K_{jT}. Examining the model C_T magnitudes in Figure 3.9C, the value of K_{jT} is expected to be the largest for the guinea pig followed by values for the cat, chinchilla, and the human, respectively. However, comparing K_{jT} values for the these species shows that the cat model does not match this prediction. This could indicate that the cat model cannot be approximated as a 2-DOF system even at low frequencies, or possibly, that the eardrum plays a strong role at these frequencies: in either of these scenarios, the simple equation for C_T (for a 2-DOF system neglecting the effects of the eardrum) does not hold.

In the 2-DOF models of the chinchilla and guinea pig and in the approximate 2-DOF models of the human and cat, Eq. 3.7 shows that at frequencies below 1 kHz (where effects of the MEC model are negligible), the magnitudes of A_T and D_T are functions of K_{mT}/K_{jT} and K_{alT}/K_{jT}, respectively. Since, at these frequencies, the human model A_T (in Figure 3.9A) and D_T (in Figure

3.9D) magnitudes are much larger than the cat, guinea pig, and chinchilla model magnitudes, it is expected that K_{mT}/K_{jT} and K_{alT}/K_{jT} are closer to one in the humans than in the other species. The model parameters match these predictions: (1) K_{mT}/K_{jT} is equal to 0.59 in the human while it is equal to 0.02, 0.05, and 0.05, for cat, guinea pig, and chinchilla, respectively, and (2) the K_{alT}/K_{jT} ratio is equal to 0.68 in the human while it is much smaller in the guinea cat, guinea pig and chinchilla (0.03, 0.01, and 0.0004, respectively).

The large low frequency A_T and D_T magnitudes seen for the human are consistent with Nakajima et al.'s suggestion that there is considerable flexibility within the human ossicular chain between the stapes and the umbo[84]. Although Nakajima et al. estimate that the incudostapedial joint is the more compliant of the two ossicular joints[84] whereas the incudomalleolar joint is the more compliant of the two joints in O'Connor and Puria's model[18], the ratio of the annular ligament stiffness to the smallest joint stiffness value estimated by Nakajima et al.[84], $K_{al}/K_{isj} = 0.49$ (found using relative values of the ossicular compliances given in Eq. 4 of Ref. 84), is similar to the ratio of the annular ligament stiffness to the smallest joint stiffness value found in the human model[18], $K_{al}/K_{imj} = 0.68$. Discrepancies in the determination in the more compliant ossicular joint between these two studies may be due to differences in topology between the model used to estimate ossicular stiffnesses in Ref. 84 and the human middle-ear model in Ref. 18.

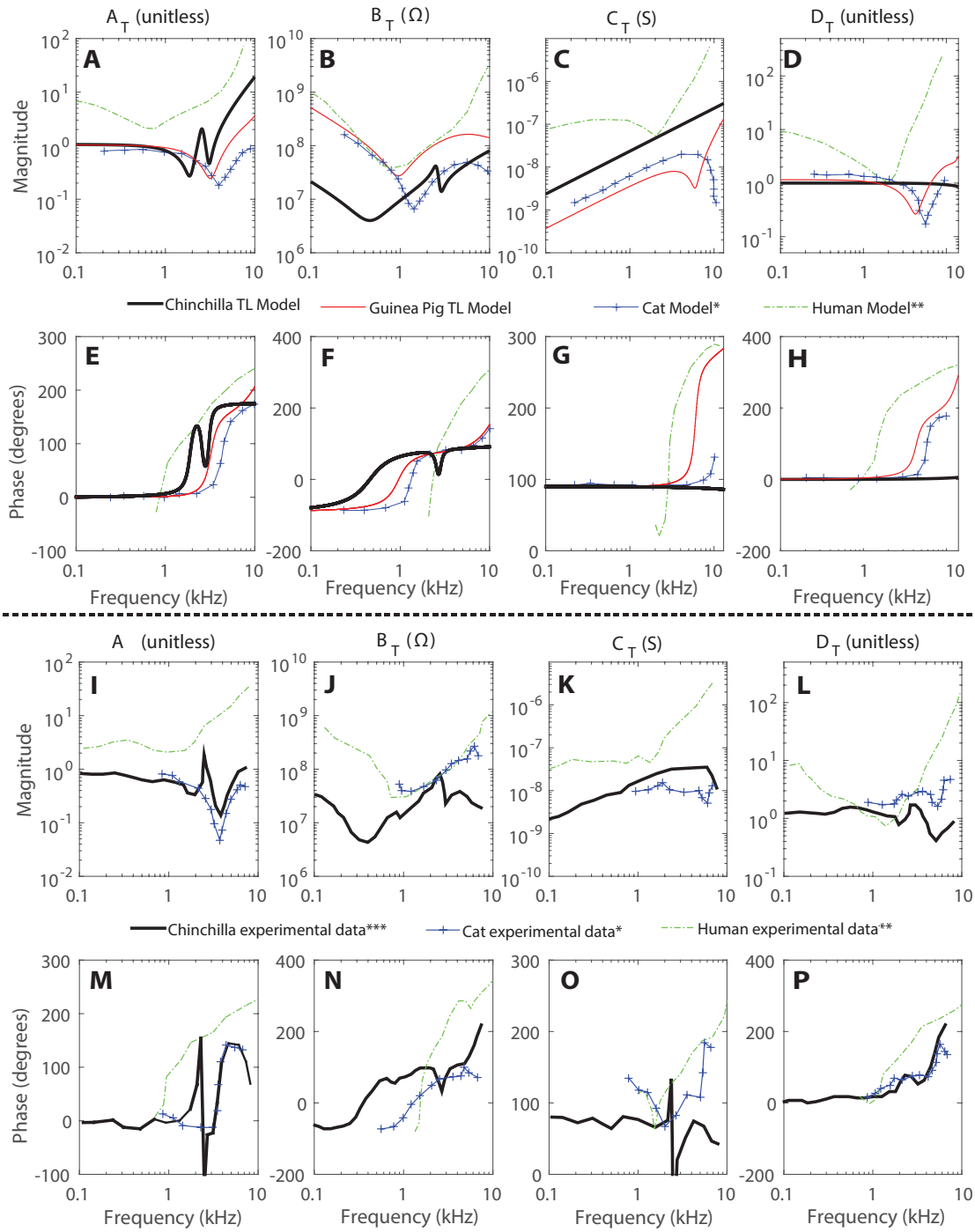

FIGURE 3.9. (Color online) A_T, B_T, C_T, and D_T results from middle-ear circuit models and experimental data. In subplots A though H, circuit model A_T, B_T, C_T, and D_T results for the human, cat, guinea pig, and chinchilla are compared. In subplots I through P, experimental A_T, B_T, C_T, and D_T data for human, cat, and chinchilla middle ears are compared. Here, * indicates cat experimental data (for cat 58) and model results[15], ** indicates human experimental data and model results[16], and *** indicates chinchilla experimental data[10]. For both the human model results and human experimental data, the phase of A provided in[16] was multiplied by -1 as the published values appeared to be erroneous.

TABLE 3.4. Area and lever ratio values used to find A_T, B_T, C_T, and D_T for the human, cat, guinea pig, and chinchilla

Animal	$A_{ed}(m^2)$	$A_{fp}(m^2)$	N_{lr} **(unitless)**	**Ref.**
Human	6.0×10^{-5}	3.1×10^{-6}	1.3	Ref. 18
Cat	4.1×10^{-5}	1.3×10^{-6}	2.0	Ref. 8
Guinea Pig	2.5×10^{-5}	1.0×10^{-6}	1.8	TL model
Chinchilla	8.0×10^{-5}	2.0×10^{-6}	3.7	TL model

3.7 Summary of Contributions & Conclusions

The circuit model described in this chapter is the first published circuit model of the chinchilla middle ear (which was first published in Ref. 61). The chinchilla middle-ear models discussed in this chapter were developed using a manual fitting procedure based on analytical expressions which directly relate model parameters to the inputs and outputs of the middle ear. With these relations, two-port transmission matrix data was used to provide insight into the stiffness, damping, and inertial properties of individual elements of the middle ear. Specifically, in this study, these expressions were used to compare the compliance of the middle-ears of several mammalian species using published two-port transmission matrix experimental data. It was found that the ratio of the (1) malleus stiffness to joint stiffness and (2) the annular ligament stiffness to joint stiffness is much higher in the human than in the chinchilla, guinea pig, and cat.

The small computational cost of the models described in this chapter would allow either model to be easily coupled with a model of the inner ear. Reasonably accurate representation of middle ear mechanics at little computational cost is valuable to researchers in computational hearing mechanics as a middle-ear model is necessary in order to compare their model results with experimental data collected in the ear canal. If the computational model of the ear is of a species other than the chinchilla is desired, the manual fitting procedure developed in this chapter could be used to quickly develop lumped parameter models for other species with similarly structured middle ears.

Chapter 4

Investigation of the slow-wave dynamics of the bullfrog eardrum

4.1 Chapter Overview

Previous studies have hypothesized that a slow, inward traveling wave is the source of a significant fraction of an extremely long group delay observed through the bullfrog middle ear[23]. However, the mechanical basis behind this slow, inward traveling wave is not understood. In this chapter, I use a simple model of the eardrum in order to elucidate the underlying mechanics of the long group delay observed in the eardrums of bullfrogs. I aim to (1) determine if this traveling wave is a likely explanation for the long group delay and (2) clarify which features of the bullfrog eardrum make possible this slow, inward traveling wave.

4.2 Introduction

In the previous chapter, a model of the eardrum which includes significant delay was found to be necessary to capture the phase of the middle-ear pressure gain at high frequencies (between 10-20 kHz). In other words, the eardrum contributes significantly to the group delay through the middle ear in the models presented in this thesis. Indeed, previous studies of the gerbil middle ear have reported that it takes $\approx 25\mu$s for sound to travel from the ear canal to the stapes footplate (within the scala vestibuli)[85]. The majority of this delay was measured between the ear canal and the umbo at frequencies below 17 kHz (and along the ossicles at higher frequencies)[86]. Significant group delay through the middle ear is not unique to the mammalian middle ear. Group delays of ≈ 0.7 ms have been observed through the bullfrog middle ear[22], approximately an order of magnitude larger than the delays measured in the gerbil middle ear. While the morphology of the amphibian middle ear is quite different than the mammalian middle ear, the area of the bullfrog eardrum[23,17] ($\approx 30 - 200mm^2$) is quite similar to that of the human eardrum[87] ($\approx 70mm^2$). Furthermore, the

hearing range of bullfrogs ($\approx 0.5 - 2$ kHz) falls within the hearing range of humans ($0.2 - 20$ kHz).

Bergevin et al. investigated the basis for this lag by examining the velocity profile across the surface of the bullfrog eardrum[23]; significant group delay through the eardrum was found. This long delay was attributed to slow, inward-traveling waves observed on these eardrums. These slow, inward-traveling waves were observed both on eardrums in normal condition and those disarticulated from the rest of the middle ear. The fact that the long group delay was observed regardless of the condition of the rest of the middle ear strongly suggests that the eardrum alone is responsible for a substantial fraction of the relatively long group delays previously reported in the bullfrog ear.

However, since the biomechanical basis for the relatively long delays of the bullfrog eardrum is not understood, the source of the long group delay through the eardrum remains unclear. In this study, the underlying mechanics behind the long group delay of the bullfrog eardrum are explored by modeling the eardrum as a flat, viscoelastic membrane with spatially dependent thickness. Clarifying the source of the long group delay through the bullfrog eardrum might help to elucidate which of the properties of the bullfrog eardrum cause its motion to differ from that of the mammalian eardrum.

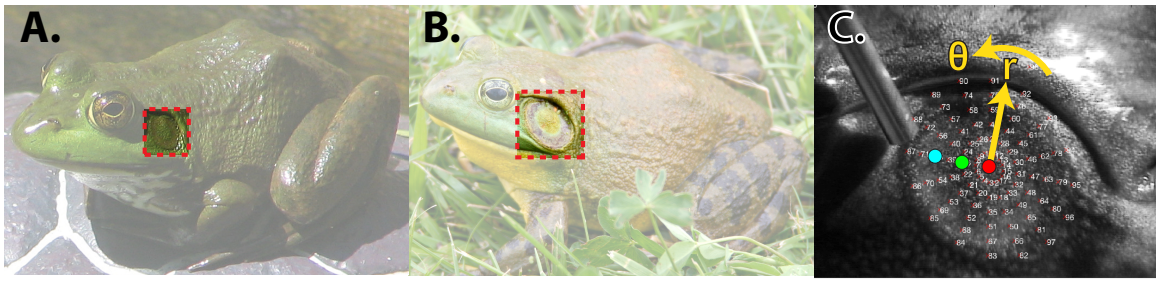

FIGURE 4.1. American Bullfrog, *Rana catesbeiana*. A. Female bullfrog (note that the area of the eardrum is small relative to the frog's eye): modified from photograph by Derek Ramsey. B. Male bullfrog (note here that the eadrum is larger than eye and center of eardrum is quite pronounced): modified from photograph by Carl D. Howe. Both images are shared under a creative commons license CC BY-SA 2.5. C. Female bullfrog eardrum along with scanning grid used in experimental measurements by our collaborators: each point on the grid is marked with a red "x." The points provided in the experimental data set used to fit the model are marked with colored circles. The red circle is at the center of the membrane ($r = 0$), the green circle is at a point between the center and the edge of the membrane ($r = 1.2$ mm), and the cyan circle is a point located towards the edge of the membrane ($r = 2.3$ mm). The microphone is visible, placed 1-2 mm away from eardrum. Experimental velocity measurements (for one representative data set) and model results (fit to the aforementioned data set) are plotted for these three points in Figure 4.5

4.3 Methods

4.3.1 Experimental Methods of Collaborators

Measurements were conducted by C. Bergevin, S.W.F. Meenderink, M. van der Heijden, and P.M. Narins. Details of the experimental methodology are outlined in Ref. 23. Briefly, three female and one male American bullfrogs (*Rana catesbeiana*) were used to record vibrations on the eardrum. Acoustic stimulation was delivered via a loudspeaker placed ≈18 cm away from the eardrum (stimulated by flat-voltage frequency sweeps with 700 ms duration where the frequency changed linearly from 0.2 to 8kHz). The resulting vibration was measured using a scanning laser Doppler vibrometer at points marked with red squares in Figure 4.1C. The analysis of the vibration assumed linearity. This process was repeated after disarticultion of the eardrum from the rest of the middle ear. The response for all female frogs was fairly similar regardless of the connection to the middle ear and significant phase accumulation was observed all eardrums, male or female, with either a disarticulated or intact middle ear. Experimental data for one representative, female disarticulated eardrum was used to fit the model (given on Figure 4.5). Additionally, experimental data for one male disarticulated eardrum is provided in order to help interpret model results (given on Figure 4.10).

4.3.2 Modeling the bullfrog eardrum

4.3.2.1 Bullfrog eardrum overview

The structure of the bullfrog eardrum is significantly simpler than that of a mammalian eardrum[88]. While the mammalian eardrum, seen in Figure 3.1, is conical and somewhat oval shaped, the eardrum of the American bullfrog is relatively flat and nearly perfectly round, as seen in Figure 4.1. The circular shape and relative thinness of the bullfrog eardrum (compared to the radius) might suggest that the eardrum's motion could be expressed using an analytical solution of a circular membrane under uniform, harmonic loading. However, in an undamped circular membrane, the presence of both forward and reverse waves will cause standing waves where (1) nodes will be present and (2) areas of the eardrum will simply be in or out of phase. In other words, an inward traveling wave will not be visible.

Although the response over the entire area of the bullfrog eardrum is not shown here (and was

not provided for the disarticulated eardrums), at frequencies below 2.5kHz, no nodes (areas with very little displacement) are observed in the experimental displacement measurements (given in Ref. 23). At frequencies between 800Hz and 3 kHz, significant phase accumulation (>0.25 cycles) is observed progressing from the outer rim of eardrum towards the center (i.e. the slope of the phase gets progressively steeper at points towards the center), seen in Figure 4.5B. This is indicative of a delay between the outer edge of the eardrum and the center, suggestive of a slow inward-traveling wave. A perfectly elastic circular membrane cannot capture these phenomena. However, with few small additions to this simple model, it could be possible to capture certain qualitative features observed in the data: the significant phase accumulation between the acoustic source and the center point of the membrane's displacement and the phase accumulation observed between the outer edge of the membrane and the center point.

Two additional features to a model of the circular membrane are proposed: (1) A non-uniform areal density due to non-uniform thickness of the eardrum and (2) significant damping due to the mucosal nature of the frog eardrum. The bullfrog eardrum is non-uniform in its thickness: the central patch (the central portion of the membrane) is thicker than the laminar annulus (the outer portion of the membrane)[89]. This non-uniform thickness is particularly pronounced in the eardrums of male bullfrogs, and can be seen on the male bullfrog eardrum in Figure 4.1B. Additionally, the bullfrog is amphibious: it spends its life both in water and on land. As such, bullfrogs have a superficial mucosal nature[23] which could cause these eardrums to act significantly more viscoelastic (and more damped, in particular) than the mammalian eardrum.

4.3.2.2 Model Assumptions & Boundary Value Problem

The membrane used to model the bullfrog eardrum is assumed to be axisymmetric, under uniform, harmonic loading, pinned at the outer rim, and isotropic. These assumptions were made in an attempt to find a simple model which is able to reproduce certain qualitative features seen in the data. In reality, the measured response is not perfectly axisymmetric. Additionally, the pressure at the eardrum is not uniform due to acuostic fluid-structure interaction that is not considered. The material properties of the bullfrog eardrum are unknown; however, it is likely that the eardrums of these frogs would be more accurately described as orthotropic as connective tissue fibers radiate outwards from the center[90]. Finally, the bullfrog eardrum is terminated around its outer perimeter

by an annular cartilage[90] which would possess some stiffness and damping properties itself: thus, the assumption that the outer rim is held perfectly stationary is an oversimplication. With these assumptions, however, a simple model can be constructed which can capture key qualitative features in the experimental data with relatively few free parameters.

The boundary value problem associated with an axisymmetric, circular membrane with spatially dependent properties under uniform, harmonic loading is derived by extending the known equation of a string with nonuniform properties into two dimensions. Morse[91] gives the most general equation of motion for a flexible string under harmonic forcing involving linear density, $\rho_s(x)$, and tension of the string, $T_s(x)$, both of which vary with x as,

$$\frac{\partial}{\partial x}\left(T_s(x)\frac{\partial \eta(x)}{\partial x}\right) + \omega^2 \rho_s(x)\eta(x) = -f_s(x) \tag{4.1}$$

where $\eta(x)$ is the transverse displacement of the string and $f_s(x)$ is the transverse applied force of density per unit length. Samejima and Fukuda[92] extended this equation into two dimensions by adding the derivative of the tension term with respect to y in Eq. 4.1 and extending all variables to functions of both x and y. Samejima and Fukuda converted this equation to cylindrical coordinates and find:

$$\begin{aligned} T_m(r,\theta)&\left(\frac{\partial^2 \zeta(r,\theta)}{\partial r^2}r + \frac{\partial \zeta(r,\theta)}{\partial r} + \frac{1}{r}\frac{\partial^2 \zeta(r,\theta)}{\partial \theta^2}\right) \\ &+ \frac{\partial T_m(r,\theta)}{\partial r}\frac{\partial \zeta(r,\theta)}{\partial r}r + \frac{1}{r}\frac{\partial T_m(r,\theta)}{\partial \theta}\frac{\partial \zeta(r,\theta)}{\partial \theta} \\ &+ \omega^2 r\rho_m(r,\theta)\zeta(r,\theta) = -rP(r,\theta) \end{aligned} \tag{4.2}$$

where $\rho_m(r,\theta)$ is the spatially varying areal density, $T_m(r,\theta)$ [N/m] is the spatially varying tension of the membrane, $\zeta(r,\theta)$ is the transverse displacement of the membrane, and $P(r,\theta)$ is the transversely applied pressure.

If axisymmetry is assumed, then $\frac{\partial \zeta}{\partial \theta} = \frac{\partial^2 \zeta}{\partial \theta^2} = 0$. Additionally, due to axisymmetry and the absence of a concentrated load at the center of the membrane, the slope at the center should be equal to zero, such that the boundary condition at $r = 0$ becomes $\frac{\partial \zeta}{\partial r}|_{r=0} = 0$. The boundary condition at the outer rim is enforced by setting the displacement at $r = R$ equal to zero, $\zeta(r)|_{r=R} = 0$. If

uniform pressure is assumed, then $P(r,\theta) = P$. Finally, $T_m(r)$ is replaced by a complex, uniform tension T_m^*, where the imaginary part of the complex tension represents the damping effects of the membrane. With these assumptions, the following boundary value problem is obtained:

$$\begin{aligned} T_m^* \left(\frac{\partial^2 \zeta(r)}{\partial r^2} r + \frac{\partial \zeta(r)}{\partial r} \right) + \omega^2 r \rho_m(r) \zeta(r) &= -Pr \\ \zeta(r)|_{r=R} &= 0 \\ \frac{\partial \zeta(r)}{\partial r}|_{r=0} &= 0 \end{aligned} \tag{4.3}$$

A finite difference method is used in order to solve the boundary value problem given in Eq. 4.3: this discretization is outlined in Appendix C.

4.3.2.3 Models of spatially-dependent areal density

The areal mass density, $\rho_m(r)$, is a parameter in the ordinary differential equation given in Eq. 4.3. Since the volumetric mass density of the eardrum, ρ, is assumed to be constant (and equal to that of water), $\rho_m(r)$ becomes a measure of the thickness of the eardrum at point r, $\rho_m(r) = \tau(r)\rho$ (where $\tau(r)$ is the eardrum thickness).

As previously mentioned, the thickness of the bullfrog eardrum is spatially dependent. The bullfrog eardrum tends to be thicker at its center and thinner towards the edge. To test whether the spatial-dependence of the eardrum thickness is necessary to capture the response seen in the experimental data, two models are proposed: (1) a model where the thickness is constant and (2) a model where the thickness varies as a piecewise function, shown on Figure 4.2. In Model 2, where the thickness varies as a piecewise function, the thicker portion of the eardrum extends from $r = 0$ to $r = R/2$ (where R is the radius of the eardrum) and the thinner portion of the eardrum consists of the region from $r = R/2$ to $r = R$. In the actual eardrum, the thickness is not distributed exactly as a piecewise function and the thickness distribution varies between frogs (although the central region is consistently and clearly thicker than the edge). The choice of $r = R/2$ is an estimation suggested by one of our collaborators, Peter Narins (based on his personal observations and extensive background in hearing mechanics in frogs).

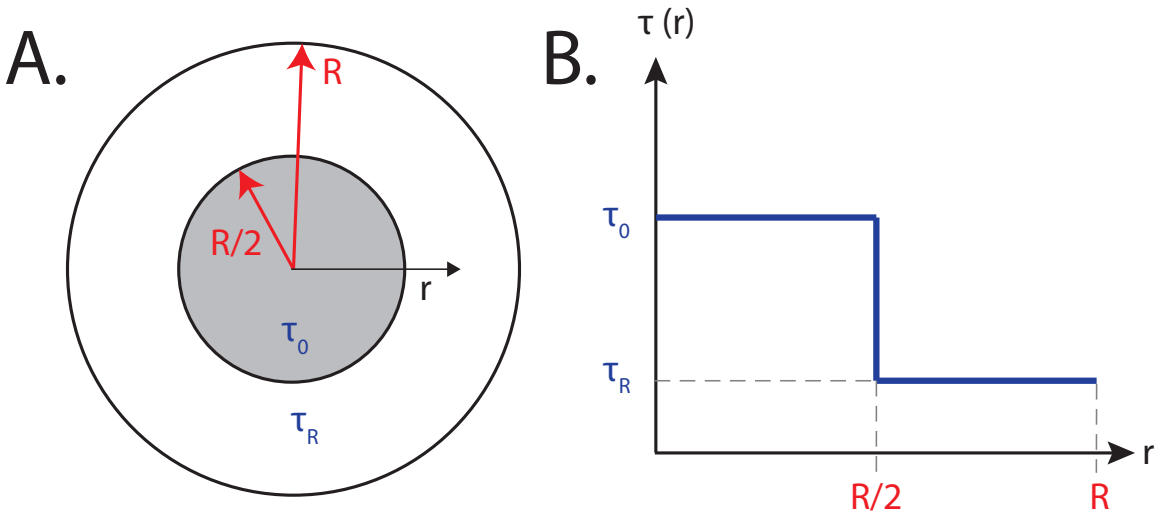

FIGURE 4.2. A. Schematic of spatially-varying, piecewise model of eardrum thickness (Model 2). B. Model of spatially-varying eardrum thickness plotted vs. r. In both panels, r is the radial dimension, as on Figure 4.1C, R is the radius of the eardrum, τ_0 is the thickness of the center portion of the membrane, and τ_R is the thickness of the outer portion of the membrane ($\tau_R = \gamma\tau_0$).

4.3.2.4 Models of eardrum damping

The damping of the eardrum is included by introducing complex tension, $T_m^*(\omega) = T_m'(\omega) + iT_m''(\omega)$, as in Ref. 93. The frequency-dependent nature of the complex tension is unknown. Three models for the relationship between the complex tension and frequency were proposed, as seen on Figure 4.3: (A) structural damping, (B) Kelvin–Voigt viscoelasticity, and (C) Maxwell viscoelasticity. In all three models, two free parameters are introduced: T_0 and $\tan\delta_{min}$ (the smallest loss tangent within the examined frequency range). Note that for structural damping, the ratio of the real and imaginary portions of the complex stiffness, referred to here as the loss tangent ($\tan\delta$), is equivalent to the structural damping factor as defined in Ref. 94. In structural damping, both the real and imaginary portions of the material are constant with frequency and thus T_0 represents the constant real portion of the stiffness at all frequencies and $\tan\delta_{min} = \tan\delta$ at all frequencies. In a Kelvin–Voigt material, the complex tension is written as,

$$T_m^*(\omega) = T_0 + i\omega\eta \tag{4.4}$$

And thus, the real portion of the tension is simply T_0 which is constant with frequency. The loss tangent can be written as,

$$\tan\delta(\omega) = \omega\eta/T_0 \tag{4.5}$$

Thus, the loss tangent increases linearly with frequency in Kelvin-Voigt materials. In a Maxwell material, the complex tension is written as,

$$T_m^*(\omega) = \frac{T_0 i\omega\eta}{i\omega\eta + T_0} \tag{4.6}$$

With the above equation, the loss tangent can be expressed as,

$$\tan\delta(\omega) = T_0/\eta\omega \tag{4.7}$$

Thus, in Maxwell materials, the loss tangent decreases with frequency.

4.3.3 Testing the necessity of spatially-dependent thickness and frequency-dependent damping

In order to determine (1) if spatially-dependent thickness is necessary to fit the experimental data and (2) how to describe the frequency-dependence of the damping, each of the two thickness models and three damping models were used to fit the experimental data. The combination of models is described in Figure 4.3.

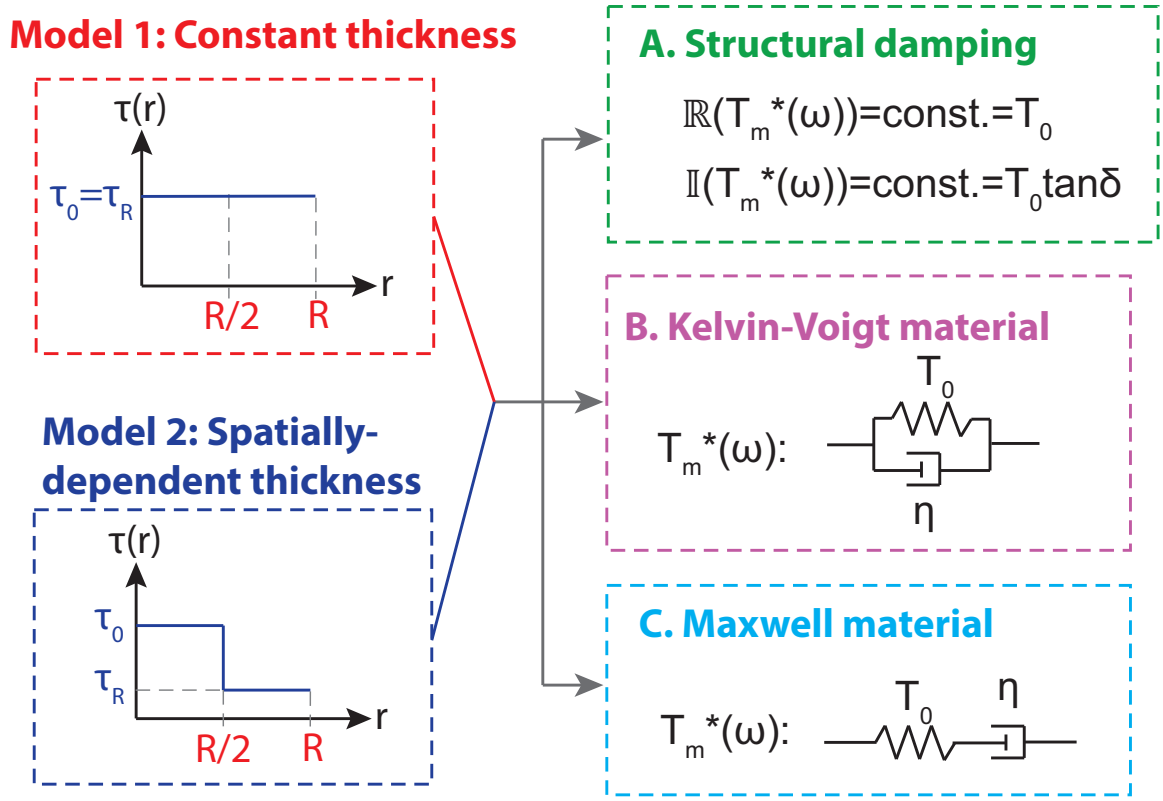

FIGURE 4.3. Combinations of thickness models (1-2) and damping models (A-C) tested. Values for the parameters ($\gamma = \tau_R/\tau_0$ (for Model 2), T_0, and $\tan\delta_{min}$) for each model combination were found using an automated fitting algorithm. It was found that a model with spatially dependent thickness and Maxwell viscoelasticity best fit the experimental data, Model 2C.

In all models, the total mass of the eardrum is fixed to an experimentally measured value of a female bullfrog eardrum from Werner et al.[17] (of 18.7 mg). All models contain two free parameters associated with the complex tension, T_0 and $\tan\delta_{min}$. For models with spatially dependent thickness (Model 2 on Figure 4.3), an additional free parameter, $\gamma = \tau_R/\tau_0$ (the ratio between the center and edge membrane thickness) is introduced.

An automated fitting algorithm was used to find the values of these parameters for each model. The allowed parameter values, the upper and lower parameter values, are given in Table C.1 in Appendix C. The fitting algorithm aims to find the values of the free parameters which best capture the phase of the experimental data at the three points indicated on Figure 4.1C ($r = 0$, $r = 1.2$ mm, and $r = 2.3$ mm) across the frequency range from 900 Hz to 3 kHz (the frequency range of the available experimental data excluding lower frequencies where the data tends to be less robust). Note that the objective function does not take the magnitude of the model response into consideration:

this due to the significant spatial (particularly in the radial direction) and frequency variation of the magnitude. If any model assumption causes the resonance frequency or mode shapes to be slightly different than in the experimental data, the error is large, even if the model appears to qualitatively fit the data. Thus, the magnitude of the response is used only for model validation after fitting the parameters.

The algorithm minimizes the value of ϵ, defined as,

$$\epsilon = \frac{1}{N_r N_\omega \phi_{ref}} \sum_{j=1}^{N_\omega} \sum_{i=1}^{N_r} (\phi_{model}(r_i, \omega_j) - \phi_{data}(r_i, \omega_j))^2 \tag{4.8}$$

where N_r is the number of spatial points examined. 3 spatial points are examined: $r = 0$, $r = 1.2$ mm, and $r = 2.3$ mm. N_ω is the number of discrete frequency points examined: 100 discrete frequencies are examined within the frequency range of 900 Hz to 3 kHz. $\phi_{model}(r_i, \omega_j)$ and $\phi_{data}(r_i, \omega_j)$ are the phase of the model velocity and the experimentally measured velocity, respectively. ϕ_{ref} is defined as,

$$\phi_{ref} = \max_{\omega, r} \left(\phi^2_{data}(r, \omega) \right) \tag{4.9}$$

where ω and r extend over the frequency and spatial points examined in Eq. 4.8.

Different functions were tested: since this particular objective function produced a smaller error when the model appeared to capture the data fairly well and a larger error when the model clearly did not look like the data, this function was deemed adequate for the study.

Note that the velocities of the model and the data are given relative to the value of the center point at 500 Hz. Thus, the magnitude of the center point at 500Hz is equal to 0dB and the phase of this point at 500Hz is equal to 0 cycles. This normalization will be employed in all data and model results shown in this chapter and in Appendix C.

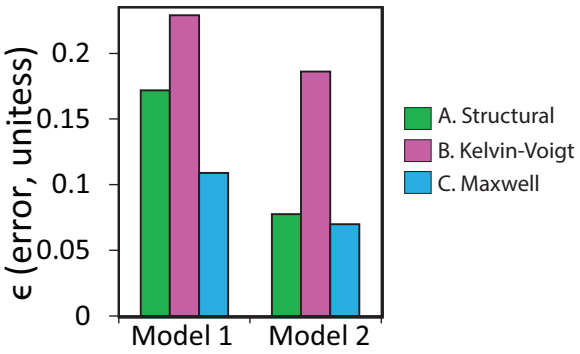

FIGURE 4.4. Error values, ϵ (defined in Eq. 4.8) found with each model combination detailed in Figure 4.3. Two different models of thickness and three different models of damping were tested. In Model 1, the thickness is constant throughout the membrane. In Model 2, the thickness varies as a Piecewise function, shown in Figure 4.2. In damping model A, the real and imaginary portions of the complex tension are constant with frequency (structural damipng). In damping model B, a Kelvin-Voigt viscoelastic material is implemented. In damping model C, a Maxwell viscoelastic material is used. In both models of thickness, using a Maxwell material produces the lowest value of ϵ. For each damping model, spatially-varying thickness produces the best fit to the data.

The error value found for the best fit of each model (detailed in Figure 4.3) is given in Figure 4.4. For both constant thickness (Model 1) and spatially varying thickness (Model 2), the lowest error is obtained using a Maxwell viscoelastic model. Additionally, for each model of damping, using spatially varying thickness (Model 2) produced the lowest error. Thus, a model with spatially-dependent thickness and Maxwell viscoelasticity will be discussed throughout the remainder of the chapter. The resulting best fit for each model combination is given in Figure C.1 in Appendix C. As discussed in Appendix C, Model 2C (a model with spatially-dependent thickness and Maxwell viscoelasticity) appears to visibly fit the data the best of any other model combination.

4.4 Results

4.4.1 Bullfrog model fit to experimental data

The model with the lowest error, Model 2C (a model with spatially varying density and Maxwell viscoelasticity) is compared to experimental data from one representative female frog in Figure 4.5. Note that for this frog, the eardrum had been disarticulated from the rest of the middle ear: this data, rather than a data set with an intact middle ear, was used in order to reduce the number of free parameters in the system (no middle-ear model is necessary to capture the response of this system).

As seen in Figure 4.5, the model captures the phase of the response at $r = 0$, $r = 1.2$ mm, and $r = 2.3$ mm very well, particularly at frequencies above 1.2 kHz. Notably, the model is able to capture the significant phase accumulation between points closer to the edge and points closer to the center seen in the experimental data. Additionally, the model captures the significant group delay through the eardrum very well (i.e. the slope of the phase at $r = 0$ is very similar to that seen in the experimental data). While the objective function does not consider the model's magnitude response, the model's magnitude response captures certain qualitative features seen in the data. For example, the model response at $r = 0$ contains small peaks and troughs, as in the experimental data, and is relatively broadband.

The model does not capture the phase at $r = 2.3$ mm at frequencies below 1.2 kHz very well. In addition, the model struggles to quantitatively fit the magnitude of the experimental data at all frequencies, particularly at $r = 1.2$ mm. These limitations were found regardless of the objective function implemented, even when the magnitude response was considered in the error definition. Thus, the model itself appears limited in its ability to fully represent the motion of the actual bullfrog eardrum. Were certain assumptions of the model loosened or additional parameters introduced (e.g. if axisymmetry was not assumed, if spatially-dependent damping were introduced, or if the geometry of the eardrum were imported from a scan of the actual system), it is possible that the model would be able to capture the experimental data with much better accuracy. However, the goal of the study was not necessarily to develop a model which can best reproduce the motion of a bullfrog eardrum. Rather, this chapter seeks a simple explanation of the long group delay though the bullfrog eardrum. With the model described in this section, which captures the experimental data with reasonable accuracy, all free parameters can be tested to examine which are responsible for the long group delay, discussed in the following subsections.

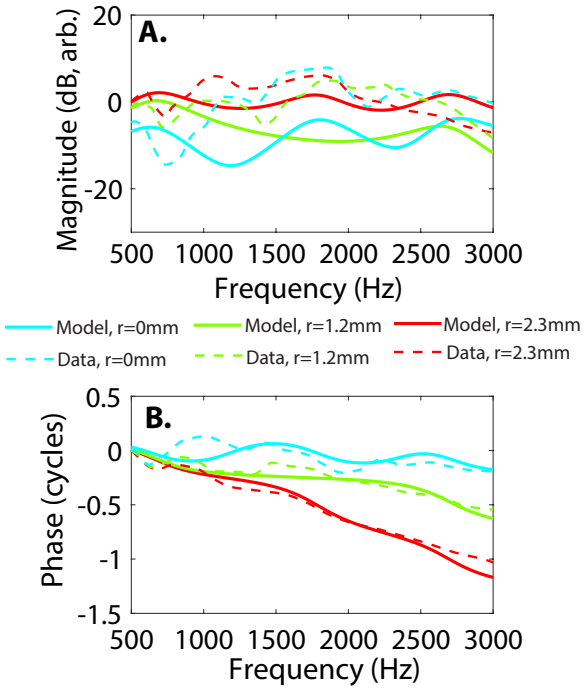

FIGURE 4.5. Comparison of the predicted model velocity at $r = 0.1$ mm, $r = 1.2$ mm, and $r = 2.3$ mm (plotted in solid lines) with the experimentally measured model velocity at $r = 0$, $r = 1.2$ mm, and $r = 2.3$ mm (plotted in dashed lines). Note that all points are normalized to the response at 500 Hz. A. Velocity magnitude in dB. B. Phase of the velocity. The experimental data is from one representative eardrum of a female frog. This eardrum had been disarticulated from the rest of the middle ear.

4.4.2 Parametric studies: effects of varying thickness ratio, damping, and mass

4.4.2.1 Spatially-varying thickness is required to capture eardrum response near edge

Here, the ratio of the thickness at the center of the membrane to the thickness at the edge of the membrane, $\gamma = \tau_R/\tau_0$ is varied and the resulting model responses are compared in order to examine how spatially-varying thickness affects the model response. The model results after varying γ while while holding the model radius, the total mass of the eardrum, and the complex tension constant (set equal to the best fit value discussed in the previous sections) are compared on Figure 4.6.

Examining Figure 4.6E-G, it can be seen that the largest effect of adjusting γ appears to be the phase of the membrane near its edge. By increasing γ from an extremely inhomogeneous case (where the thickness at the edge is only 4% of that at the edge) to the case where the thickness is uniform ($\gamma = 1$), it can be seen that the average slope of the phase at $r = 2.3$ mm goes from being nearly zero to a non-zero, negative value. This can be seen most clearly by examining the

value of the phase at $r = 2.3$ mm at 3 kHz for all three cases (indicated with a magenta asterisk in Figures 4.6E-G): this value drops from ≈ 0.4 cycles when $\gamma = 0.04$ (seen on Figure 4.6E) to nearly -0.5 cycles when $\gamma = 1$ (seen on Figure 4.6G). At the fit value (of $\gamma = 0.43$), the phase of the edge point matches the data quite well throughout the frequency range. Interestingly, the phase at the center point, $r = 0$, does not change significantly regardless of the value chosen for γ. This suggests that despite the necessity of spatially-varying thickness to capture the eardrum's motion at its edge, spatially-varying thickness is not necessary to capture the long group delay through the eardrum.

Altering the value of γ also appears to change the magnitude of the model's response. By setting $\gamma = 0.04$, the magnitude at all three points ($r = 0$, $r = 1.2$ mm, and $r = 2.3$ mm), seen in Figure 4.6B, is slightly lower than that of the fit value, seen in 4.6C. By introducing uniform thickness, $\gamma = 1$, as seen in 4.6D, the magnitude of the center point becomes more bandpass-like and looks quite a bit like the data. However, the magnitude of the model at $r = 2.3$ mm starts to look significantly different than the data; specifically, only one local minimum is seen at 1.8 kHz.

Thus, in order best capture the response near the edge of the membrane, the thickness near the edge of the membrane must be smaller than that at the center, as in the actual eardrum of the bullfrog[89].

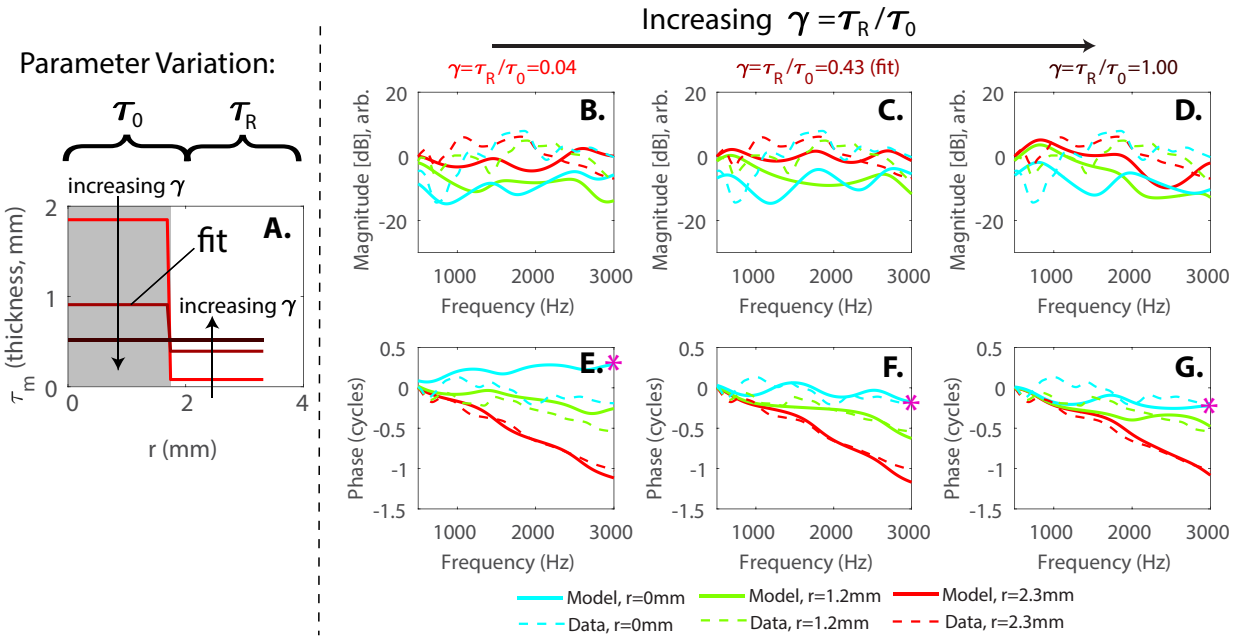

FIGURE 4.6. Model results after varying $\gamma = \tau_R/\tau_0$ while holding R, the total mass of the eardrum, and T_m^* constant (from fit value). A. The values of the thickness vs. radial position after varying $\gamma = \tau_R/\tau_0$. On the right portion of the figure, the magnitude (B-D) and phase (E-G) of the model response at $r = 0$, $r = 1.2$ mm, and $r = 2.3$ mm after varying γ is compared to the experimentally measured motion at the same points. The magenta asterisk plotted at 3kHz on E-G is to help visualize the affect of γ on the model's phase response near the edge.

4.4.2.2 Significant damping is necessary to capture traveling wave and response magnitude

In this subsection, the minimum loss tangent seen over the frequency range examined in this study, $\tan\delta_{min}$, is varied while keeping T_0 and $\gamma = \tau_R/\tau_0$ constant in order to examine the effects of high or low damping on the model response. Note that by changing $\tan\delta_{min}$, the values of both $\tan\delta(\omega)$ and $\Re(T_m^*)$ are changed as well. For Maxwell materials, $\tan\delta_{min} = \tan\delta(\omega_{max}) = T_0/(\eta\omega_{max})$ where ω_{max} is simply the largest frequency examined. Thus, $\tan\delta$ can be written in terms of $\tan\delta_{min}$ as,

$$\tan\delta(\omega) = \frac{\tan\delta_{min}\omega_{max}}{\omega} \tag{4.10}$$

The portion of the tension is written in terms of $\tan\delta_{min}$ as,

$$\Re(T_m^*) = \frac{T_0}{1 + \tan\delta_{min}^2\omega_{max}^2/\omega^2} \tag{4.11}$$

In Figure 4.7A-B, $\tan\delta_{min}$ is varied and the resulting $\tan\delta(\omega)$ and $\Re(T_m^*)$ are given. The model

results after varying $\tan\delta_{min}$ while while holding the values of R, T_0, $\gamma = \tau_R/\tau_0$, and the total mass of the eardrum constant (set equal to the best fit value discussed in the previous sections) are compared on Figure 4.7C-H. Examining panels C-E, it is clear that the largest effect of varying $\tan\delta_{min}$ is the large change in damping: while the frequencies of the peaks and troughs remain roughly the same (where they can be seen, Panels C-D), the sharpness of the peaks and troughs decreases dramatically as $\tan\delta_{min}$ is increased. This can be seen clearly by examining the effect of $\tan\delta_{min}$ on the second peak seen in the magnitude of the response at $r = 0$, marked with a blue asterisk on Panels C-D. Increasing $\tan\delta_{min}$ from 0.03 to 0.17, the location of the peak remains at approximately 1.8 kHz; however, the magnitude drops from approximately 18 dB to 2 dB. When $\tan\delta_{min}$ is increased to 0.33, no local minima are clearly visible across the frequency range near the center of the membrane.

Examining Figures 4.7F-H, it can be seen that changing the value of $\tan\delta_{min}$ also has a noticeable effect on the phase of the response. When the loss tangent is quite low, as in Figure 4.7F, there are many jumps in the phase seen at all spatial points on the membrane and throughout the frequency range. These phase jumps indicate standing waves: in other words, regions of the membrane simply move in or out of phase, no traveling wave is present. As $\tan\delta_{min}$ is increased, the phase of the response at all spatial points vs. frequency appears nearly linear where the phase of the slope becomes more steep towards the membrane center, indicative of a traveling wave moving from the edge to the center. Thus, significant damping is necessary in order for a traveling wave to appear on these membranes.

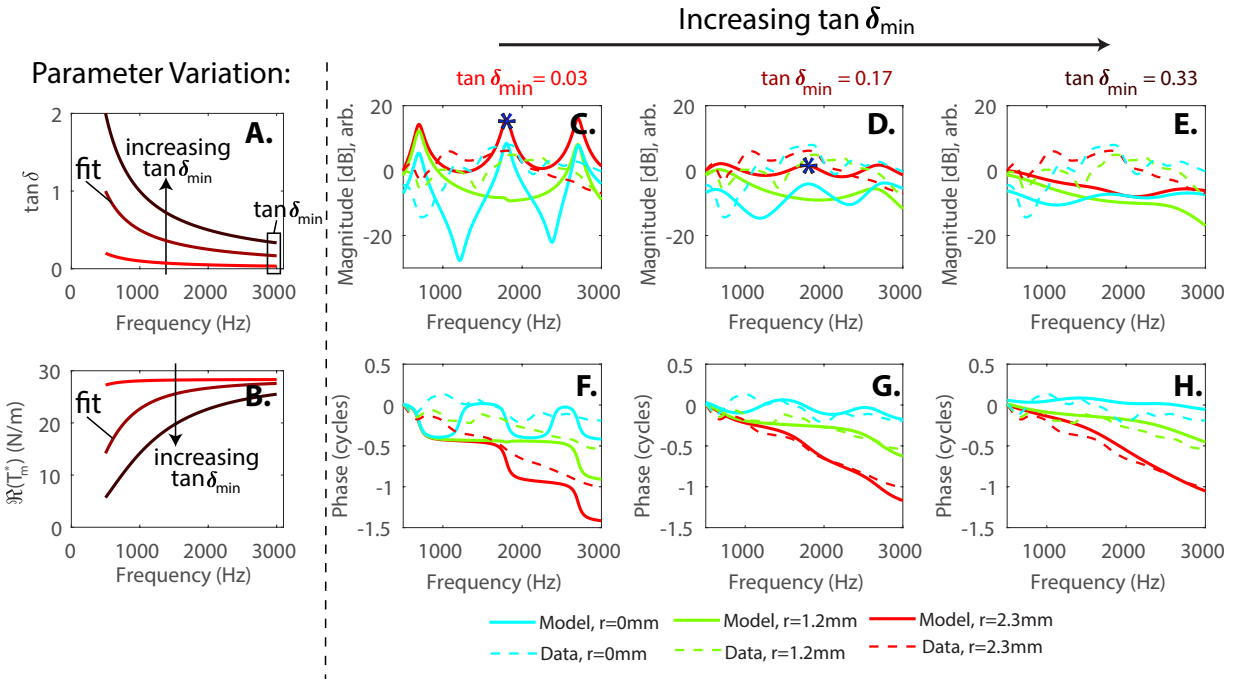

FIGURE 4.7. Model results after varying $\tan\delta_{min}$ ($= \tan\delta(\omega_{max})$ where ω_{max} is the largest frequency within the range explored here). In this study, R, $\gamma = \tau_0/\tau_R$, and T_0 are held constant. A-B. The values of $\tan\delta(\omega)$ (A) and $\Re(T_m^*)$ (B) vs. frequency after varying $\tan\delta_{min}$. On the right portion of the figure, the magnitude (C-E) and phase (F-H) of the model response at $r = 0$, $r = 1.2$ mm, and $r = 2.3$ mm after varying $\tan\delta_{min}$ is compared to the experimentally measured motion at the same points. The blue asterisk seen on Panels C-D marks the location of the second peak in order to aid in visualization of the effect of altering $\tan\delta_{min}$ on the height of the peaks.

4.4.2.3 Altering membrane thickness drastically changes group delay through eardrum

Here, the effect of the model's thickness on its response is examined. The values of τ_0, τ_R are varied uniformly (thereby increasing the mass of the membrane) while the values of $\gamma = \tau_0/\tau_R$, the radius, and the complex tension are held constant (and set equal to the best fit model value). The resulting spatial variations of the thickness for the three values of τ_0 (and thereby τ_R) examined are given on Figure 4.8A. The model results after varying the model thickness are given on Figures 4.8B-G: as seen in these figures, varying the thickness of the membrane drastically alters both the magnitude and phase of the response at all three points examined.

As seen on Figures 4.8B-C, by decreasing the model thickness, the frequency of the first peak is shifted to a higher frequency and all other peaks are now outside of the examined frequency range. By increasing the thickness, as seen on Figures 4.8C-D, the peaks appear to have shifted downwards and the magnitude at the center point ($r = 0$) becomes more lowpass-like. Additionally,

by increasing the model thickness, the average slope of the phase for the model response at $r = 0$ increases significantly between 1.5-3 kHz indicating a large increase in the group delay though the eardrum.

Combined with the results from the previous subsection, it is clear that a combination of significant damping and large thickness is largely responsible for the slow-inward traveling wave on the eardrum. Note that, as discussed in the next section, the model's tension and thickness are both directly linked to its wave speed. Thus, a parametric study of T_0 (which changes the real portion of the complex tension) is not provided in this chapter, since increasing T_0 affects the model's results in the same manner as decreasing the model's thickness.

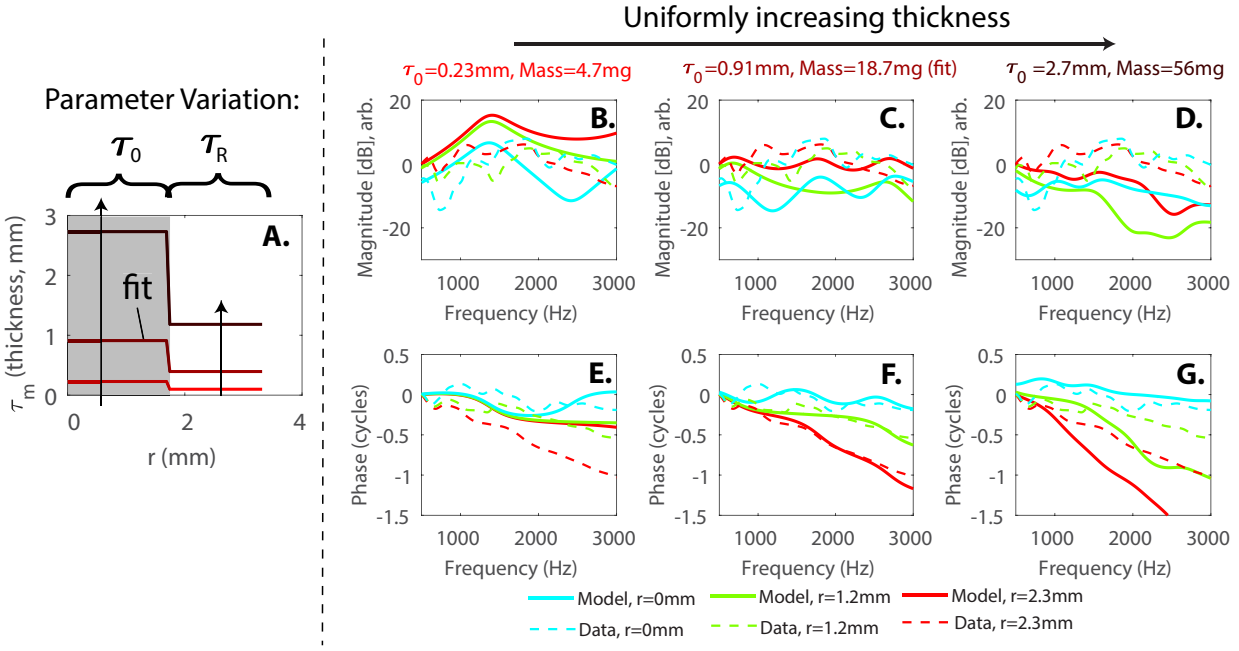

FIGURE 4.8. Model results after varying τ_0 and τ_R while holding R, $\gamma = \tau_0/\tau_R$, and T_m^* constant. A. The values of the thickness vs. radial position after varying τ_0 and τ_R. On the right portion of the figure, the magnitude (B-D) and phase (E-G) of the model response at $r = 0.1$ mm, $r = 1.2$ mm, and $r = 2.3$ mm after varying the model thickness is compared to the experimentally measured motion at the same points.

4.5 Interpretation of model results

4.5.1 Traveling wave explains long group delay through middle ear

If a traveling wave is responsible for the group delay observed in the model results, then by either (1) changing the radius while keeping the wave speed constant or (2) altering the wave speed, a predictable change in the group delay will occur. If reflections at any point of the membrane are assumed to be minimal, the delay of a wave traveling from the edge of the membrane to the center can be estimated as,

$$\Delta t = \frac{R}{2}\left(\frac{1}{c_0} + \frac{1}{c_R}\right) \tag{4.12}$$

where R is the radius of the membrane whose thickness is spatially dependent as described in Figure 4.3, c_0 is the wave speed from $r = 0$ to $r = R/2$ (where the membrane is thickest) and c_R is the wave speed from $r = R/2$ to $r = R$ (where the membrane is thin). Noting that the complex wave number, k^*, of a membrane with complex tension is written as[93] $k^* = \omega\sqrt{\rho_m/T_m^*}$, the wave speed is found using $c = \omega/\Re(k^*)$:

$$c(r,\omega) = \Re\left(\sqrt{\frac{T_m^*(\omega)}{\rho\tau(r)}}\right) \tag{4.13}$$

In the remainder of this study, $c(r,\omega)$ is found at frequencies above 1.5 kHz where the real portion of the complex tension is approximately constant and the imaginary portion of the complex tension is small ($\tan\delta < 0.3$).

In Figure 4.9, the validity of the expression for the group delay given in Eq. 4.12 is tested: values found for Δt using Eq. 4.12 are compared to the group delay predicted by the model after varying R or τ_0 and τ_R (while holding $\gamma = \tau_R/\tau_0$, $\tan\delta_{min}$, and T_0 constant). The model group delay is found by fitting a line to the phase of the response of the center point from the frequency of the first peak to the end of the frequency range (at 3 kHz).

The results of uniformly varying the membrane thickness (τ_0 and τ_R) while holding R constant are seen in Figure 4.9A: it is clear that by changing the model thickness, the wave speed is altered and the resulting changes to the model group delay can be accurately captured by Eq. 4.12.

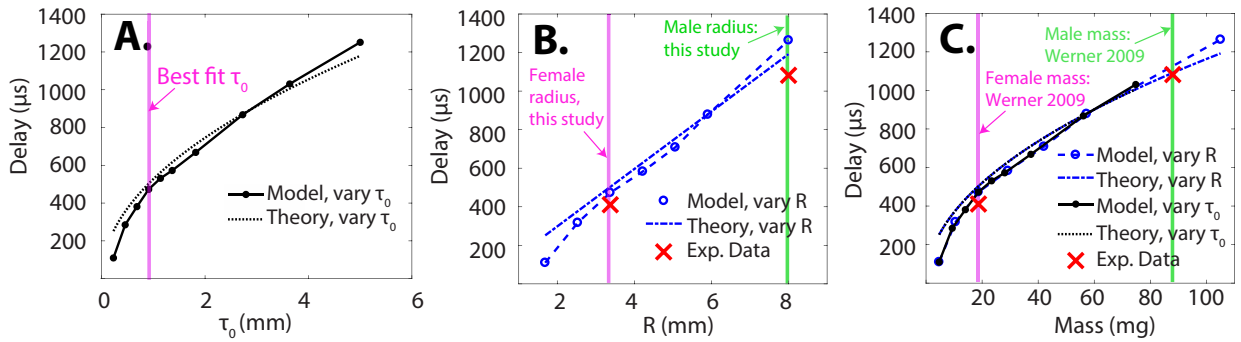

FIGURE 4.9. A study of the group delay predicted by the model compared with theoretical estimations found using Eq. 4.12 and the group delay calculated from experimental data from one male and one female disarticulated eardrum. Note the group delay found from model results and experimental data is calculated by fitting a line from the first peak in the experimental data to the end of the frequency range. A. Model group delay calculated on a female model eardrum after uniformly varying the model thickness (τ_0 and τ_R) is compared to estimates using Eq. 4.12. B. Model group delay calculated using female material and thickness values and varying the model radius is compared to theoretical group delay estimates found using Eq. 4.12 and to the delay found for one male and one female eardrum. C. Group delays calculated from model results found either by changing the thickness or the radius of the model are compared to theoretical estimates or to experimentally captured group delay (where the mass of the male and female bullfrog are set equal to that found by Werner et al.[17]).

In Figure 4.9B, the resulting model group delay found by holding c_0 and c_R constant while varying R is compared to the estimated group delay calculated using Eq. 4.12. Comparing the two curves, it is seen that the group delay found using Eq. 4.12 provides an accurate estimate of the group delay of the model, particularly at larger values of R where reflection at the center of the membrane is negligible. Additionally, the group delay found using experimental measurements of the response of one female eardrum (where $R = 3.4$ mm) and one male eardrum (where $R = 8.0$ mm) (via fitting a line to the phase of the response) are plotted in order to understand if the increased diameter in male frogs could explain the longer group delays seen in these frogs. It appears that that this is indeed the case: while other factors may influence the group delay (such differing thickness between male and female frogs), the larger radius alone is enough to explain the longer group delay observed in these frogs.

As further evidence that the larger radius is the primary difference between the male and female bullfrog eardrums used in this study, the radius of the best fit eardrum (fit to female data) is increased to that of the male eardrum while the eardrum thickness and all other model parameters (T_0, $\gamma = \tau_0/\tau_R$, and $\tan\delta_{min}$) are held constant and set equal to that of the best fit model. The

resulting model response is compared to measurements of a male bullfrog eardrum in Figure 4.10. As seen on Figure 4.10A, using the values of T_m^* and $\gamma = \tau_0/\tau_R$ found for the best fit female model but inserting a male-sized radius, the model captures the broadband nature of the magnitude of the response seen in the male data quite well, particularly at frequencies lower than 2 kHz. It is also reproduces the local minimum seen in the center point magnitude ($r = 0$) at around 2 kHz seen on Figure 4.10A (seen at around 1.8 kHz in the model, marked with a magenta star and around 2.3 kHz in the data, marked with a blue rectangle). Additionally, as seen on Figure 4.10B, it can be seen that by increasing the radius of the model to that measured for male eardrums, the model is able to capture the phase of the measured male bullfrog velocity very well; as such, the longer group delay seen in the male bullfrog is reproduced by the model.

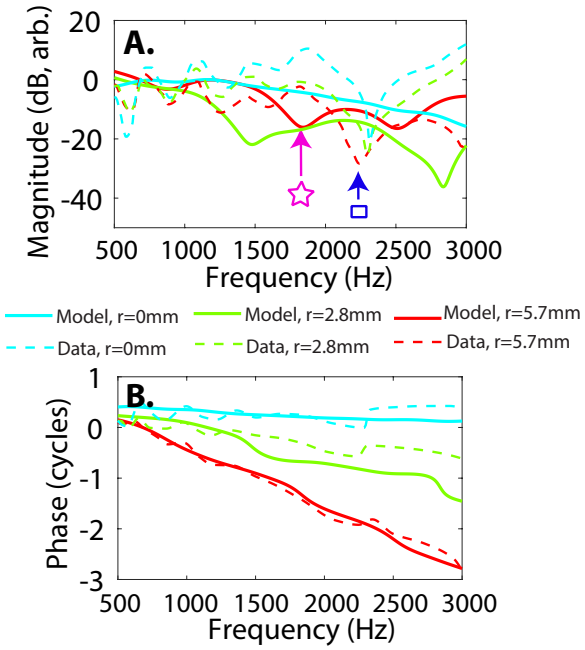

FIGURE 4.10. Comparison of model velocity response (after changing the radius of the model to that of the radius of the male in the experimental data) to experimentally measured velocity of a disarticulated male eardrum. All free parameters of the model (the thickness, thickness ratio, and complex tension) are equal to that found for the female bullfrog eardrum. A. The magnitude of the velocity (in arbitrary dB units, normalized to a value at 700Hz). B. The phase of the velocity.

By changing either the model thickness or the model radius, the mass of the eardrum is altered. By plotting the group delay vs. the mass, the results on 4.9A-B can be directly compared and the results found by varying the model's thickness can be compared to experimental data. The group delay found for both the male and the female bullfrog eardrums in this study are plotted vs.

the mean mass value found for male and female eardrums by Werner et al.[17]. As seen on 4.9C, regardless of whether the radius or the thickness is being altered, the group delay is nearly the same; in all cases, the resulting model group delay is very similar to that found by Eq. 4.12. Additionally, the group delay calculated from the experimental measurements are very similar to that found by using the model and by Eq. 4.12.

Thus, since altering the distance over which the wave travels or altering the wave speed both predictably change the group delay through the eardrum, it appears that a traveling wave is indeed the source of the large group delay seen in the eardrums of bullfrogs.

4.5.2 Long group delay through bullfrog eardrum due to large thickness and significant damping relative to mammalian eardrum

While the eardrums of bullfrogs ($A_{ed} = 30 - 200$ mm^2 in this study) and humans[87] ($A_{ed} \approx 70$ mm^2) are similar in surface area, the group delay of the center point of human eardrums is significantly shorter than that in the bullfrog. At midrange frequencies (1-11 kHz), the delay through the human middle ear is $\approx 130\mu$s (calculated using data from Ref. 18), while the group delays calculated from the experimental data for male and female bullfrog eardrums were found to be $\approx 990\mu$s and $\approx 470\mu$s, respectively. Since there are many differences in the eardrums of bullfrogs and humans, it is difficult to make any firm conclusions as to why the delays are so much shorter in human eardrums.

However, there are known differences between the eardrums of these species which, if all else is equal, would shorten the delays predicted by the model dramatically. Most significantly, the thickness of the bullfrog eardrum is very large relative to the human eardrum. The results of the model fitting procedure suggest that the thickness of the female bullfrog eardrum ranges from ≈ 0.4mm towards to the edge to ≈ 0.9 mm near the center of the membrane: this is roughly similar to the thickness of an adult male bullfrog eardrum (of ≈ 0.3mm towards the edge and ≈ 2mm at the center) found using images from Horowitz and Simmons[95]. The thickness of the human eardrum is 0.04-0.12 mm[96], an order of magnitude smaller than that seen in the bullfrog. As seen on Figure 4.9A, if the real portion of the tension is held constant, when the center thickness is reduced to 0.2 mm, the group delay predicted by the model is $\approx 150\mu$s, similar to that calculated through the human eardrum. However, the differences in the tension between species are unknown, so interpretation of the differences in wave speed between species in this manner is, again, limited.

Another feature which might contribute to the long group delay through the bullfrog eardrum relative to mammals is its superficial mucosal nature which might cause the eardrums of these frogs to be relatively damped. It was found that significant damping is necessary for an inward-traveling wave to be present: otherwise, standing waves appear and there is very little delay at any given frequency. It is possible that the mammalian eardrum is not nearly as damped, and thus, any group delay would be unrelated to an inward-traveling wave.

Furthermore, the geometry of the mammalian eardrum is more complex than that of the frog. Most noticeably, the mammalian eardrum is more conically shaped, as seen in Figure 3.1A-B of the previous chapter, whereas the frog eardrum is relatively flat, as seen in Figure 4.1. Using a mathematical model, Fay et al. investigated the effects of several features of the human eardrum on its ability to transmit sound[97]. Two features produced noticeable changes to the phase between the input and the umbo: the depth of the conical shape and the degree of orthotropy of the eardrum. Changing the depth of the human eardrum model produced a clear trend between the frequencies of 700 Hz and 6 kHz: as the depth of the model was reduced, the average group delay within in this frequency range increased (the flat model's delay was ≈ 1.3 times larger than the model with large depth). Fay et al. also found that extreme orthotropy causes a larger average group delay at frequencies below 2 kHz[97]: however, whether the bullfrog eardrum is more anisotropic than the human eardrum is unknown.

4.6 Summary of Contributions & Conclusions

In this study, an isotropic, viscoelastic circular membrane was used to model the displacement of bullfrog eardrum in response to harmonic, uniform pressure. Using this simple model, I found that viscoelasticity and slow wave speed are both necessary to reproduce the phase response seen in the experimental data. These two properties, when combined, produce the observed slow traveling waves observed in previous measurements of bullfrog eardrum: significant damping reduces the presence of outward-traveling such that inward-traveling waves are dominate in the response of the eardrum. The large thickness of these eardrums contributes to the slow wave speed. By adjusting either the wave speed (by adjusting the thickness of the membrane) or the distance over which the wave travels (by adjusting the eardrum radius), the group delay is altered predictably which

demonstrates that the source of the group delay in these eardrums is, in fact, a traveling wave. This hypothesis was tested by looking at the group delay though male bullfrog eardrums where the radius is nearly twice as large as that of the female eardrum: in these eardrums, as predicted by the model simulations and by assuming an inward-traveling wave with no reflection, the group delay is approximately twice as long as that observed on female bullfrog eardrums.

Chapter 5

Conclusion

5.1 Summary of contributions

This thesis investigated the mechanics of the mouse tectorial membrane, the chinchilla middle ear, and the bullfrog eardrum.

In the second chapter of this thesis, I characterized, for the first time, the anisotropic, viscoelastic material properties of the TMs of wild-type and transgenic mice at auditory frequencies. These material properties were found using an inverse fitting algorithm which sought the material parameters of finite element models which best capture experimentally measured displacements of isolated TM segments provided by our collaborators. I was able to uncover statistically significant changes in the anisotropic, dynamic material properties of the TM due to the $Tectb^{-/-}$ mutation. Finally, a parameter study was conducted in order to determine the influence of the TM's material parameters, width, and fiber orientation on its motion. The results of this analysis suggest that at auditory frequencies, the material properties of the TMs of humans are different than in mice. A study which considers the finite width and anisotropy of the TM, as was done in this thesis, is needed to quantify these differences in material properties.

In this third chapter of this thesis, for the first time, a circuit model of the chinchilla middle ear was developed[61]. The chinchilla middle-ear models discussed in this thesis were developed using a manual fitting procedure based on analytical expressions which directly relate model parameters to the inputs and outputs of the middle ear. With these relations, two-port transmission matrix data was used to provide insight into the stiffness, damping, and inertial properties of individual elements of the middle ear. These expressions were used to compare the ossicular chain compliance of several mammalian species using published two-port transmission matrix experimental data. It was found that the ratio of the (1) malleus stiffness to joint stiffness and (2) the annular ligament

stiffness to joint stiffness is much higher in the human than in the chinchilla, guinea pig, and cat.

The delay through the middle ear of bullfrogs is nearly an order of magnitude larger than that seen in mammals. A large portion of this large group delay through the bullfrog middle ear had previously been attributed to the eardrum[23,22]; however, prior to this study, the mechanics which allow for a slow-inward traveling wave were not well understood. An isotropic, viscoelastic circular membrane was used to model the displacement of bullfrog eardrum in response to harmonic, uniform pressure. Using this simple model, I found that viscoelasticity and slow wave speed are both necessary to reproduce the phase response seen in the experimental data. Significant damping reduces the presence of outward-traveling such that inward-traveling waves are dominate in the response of the eardrum. In addition, the relatively large thickness (compared to the mammalian eardrum) contributes to the slow speed of the waves on these eardrums. By adjusting either the wave speed or the distance over which the wave travels (by adjusting the eardrum radius), the group delay is altered predictably, which demonstrates that the source of the group delay in these eardrums is, in fact, a traveling wave.

5.2 Opportunities for future work

In a future study, the anisotropic, visceolastic material properties found for wild-type and $Tectb^{-/-}$ mice, discussed in Chapter 2, could be inserted into existing computational models of the cochlea[1,98,99,100] which would allow (1) for more realistic modeling of the TM and (2) the consequences of the $Tectb^{-/-}$ mutation on cochlear mechanics to be evaluated. In addition, the inverse fitting algorithm could be applied to experimental measurements of isolated TM segments of other genetically modified mice (such as the $Tecta^{Y1870C/+}$ mutation[20]) or of other species, such as human TMs, should the data become available. Repeating the analysis conducted in this thesis on a mutant where the TM's collagen fibers, rather than its striated sheet matrix, are greatly disrupted (such as in $Col11a2^{-/-}$ mice, previously studied by our collaborators using shear impedance measurements[37]), would particularly interesting, as the anisotropy introduced by collagen fibers was hypothesized to play a large role on the motion of isolated TM segments. Furthermore, while the fluid surrounding the TM was ignored in this study, the addition of a viscous boundary layer into the model would introduce an inertial load and additional damping onto the TM: the addition of extra damping due

to the fluid might help the model capture the actual loss tangent of the TM material. Exploring the effect of a viscous boundary layer on the motion of the TM would be an excellent next step prior to evaluating the material properties of other transgenic mice since reduced damping is thought to be the main material difference between the TMs of wild-type and some transgenic mice, such as $Tecta^{Y1870C/+}$ mice.

The small computational cost of the chinchilla middle-ear models described in the third chapter of this thesis would allow either model to be easily coupled with a model of the inner ear. Reasonably accurate representation of middle ear mechanics at little computational cost is valuable to researchers in computational hearing mechanics as a middle-ear model is necessary in order to compare their model results with experimental data collected in the ear canal. If the computational model of the ear of a species other than the chinchilla is desired, the manual fitting procedure developed in Chapter 3 could be used to quickly develop lumped parameter models for other species with similarly structured middle ears, should the experimental data become available.

Finally, in the fourth chapter of this thesis, the slow speed of the inward-traveling waves of the bullfrog eardrum was attributed to the relative thickness of these eardrums. This hypothesis could be experimentally tested by adding mass to bullfrog eardrums (e.g. by attaching a soft, thin, dense film to the eardrum) and repeating the study. A similar test was conducted (although not discussed in this thesis) where the eardrum was allowed to dry and the experimental measurements were repeated. However, since several variables are changed during this experiment (the damping is decreased, the mass is decreased, and the stiffness is likely increased), all of which would reduce the group delay, it is difficult to analyze which factor is responsible for the altered response.

Appendix A: Tectorial membrane mechanics supplemental information

A.1 Statistical analysis of material property differences

In order to better understand if the differences in material properties found between WT and WT and $Tectb^{-/-}$ TMs are representative of the differences seen between the average wild-type and $Tectb^{-/-}$ TMs, at each frequency examined in the study, the 95% confidence interval for each material property is calculated.

As seen on Figures A.1A-B, throughout the entire frequency range, there is no overlap between the confidence intervals found for wild-type and $Tectb^{-/-}$ values for E_t and G_{tf}. Thus, it appears that the average wild-type TM is likely significantly stiffer than the average $Tectb^{-/-}$ TM in the transverse direction and in shear. In the fiber-direction, there is significant overlap in the confidence intervals found for E_f: thus, it is remains unclear if the $Tectb^{-/-}$ mutation affects the fiber-direction stiffness. The significant difference in E_t between phenotypes causes the TMs of $Tectb^{-/-}$ mice to be significantly more anisotropic than WT TMs, as no overlap in $\Gamma(\omega) = E_f/E_t(\omega)$ is seen throughout the frequency range. Additionally, for both phenotypes, throughout the frequency range, the confidence interval for Γ remains above one indicating that the average TM is likely to be significantly anisotropic.

As seen on Figures A.2, there is significant overlap in all damping parameters. Therefore, it remains unclear if the $Tectb^{-/-}$ mutation affects TM damping.

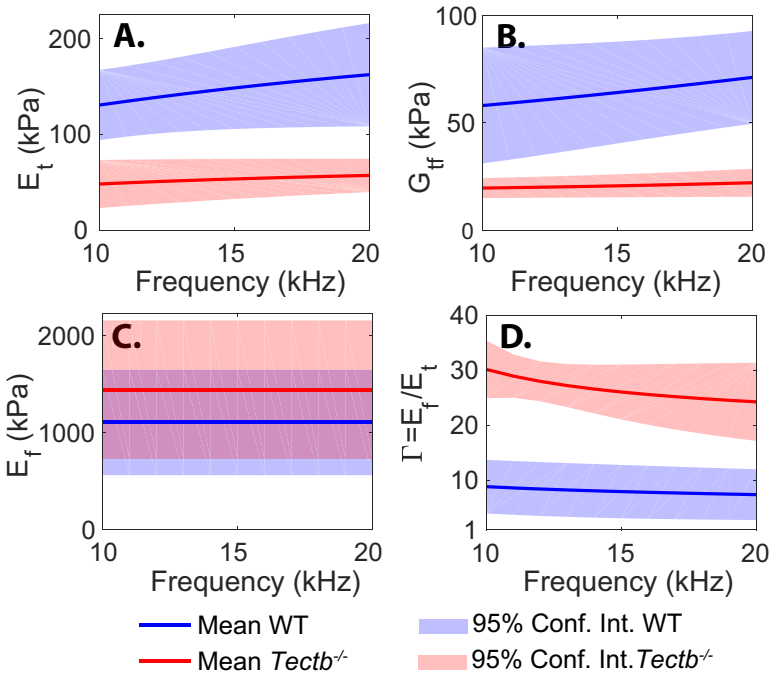

FIGURE A.1. Effect of $Tectb^{-/-}$ mutation on anisotropic stiffness properties: the Young's moduli in the transverse (A) and fiber (C) directions, the in-plane shear moduli (B), and the anisotropy ratio (D). Mean anisotropic storage moduli values found for wild-type (n=6) and $Tectb^{-/-}$ (n=5) mice TMs are plotted using solid lines. Shading indicates the 95% confidence interval in this study for each phenotype calculated at each frequency.

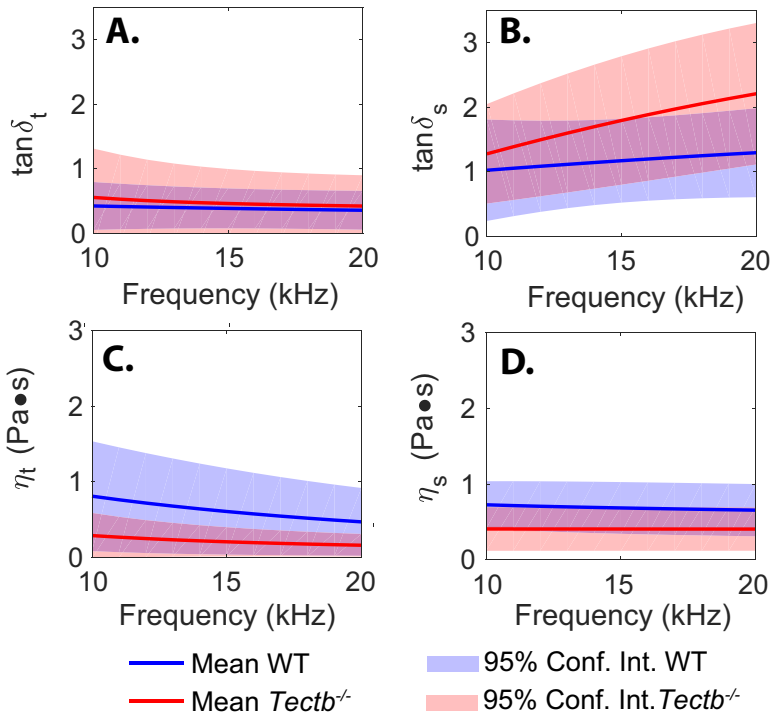

FIGURE A.2. Effect of $Tectb^{-/-}$ mutation on anisotropic damping properties: the loss tangent in the transverse direction (A), the loss tangent in shear (C), the transverse direction viscosity (C), and the shear viscosity (D). Mean material loss tangent (A-B) and viscosity (C-D) values found for wild-type (n=6) and $Tectb^{-/-}$ (n=5) mice TMs are plotted with solid lines. Shading indicates the 95% confidence interval of material properties found in this study for each phenotype.

To further analyze whether the difference in E_t and G_{tf} found between phenotypes is statistically meaningful, a two-sample t-test was conducted. In this test, the two populations are assumed to be normally distributed. The variances of the values found for WT and those found for $Tectb^{-/-}$ are not assumed to be equal (the Behrens-Fisher problem); since the variances are not assumed to be equal, the Welch-Satterthwaite equation is used to estimate the effective degrees of freedom. The null hypotheses tested and the results of each test are given in Table A.1. From Table A.1, it can be seen that the null hypotheses stating that the TMs of $Tectb^{-/-}$ are of equal or greater stiffness than the TMs of WT mice (in the transverse direction or in shear) can be rejected at a 5% significance level, while the null hypothesis stating that the TMs of WT mice are stiffer than those of $Tectb^{-/-}$ mice can not be rejected.

TABLE A.1. Results of a two-sample t-test at a 5% significance level for parameters whose 95% confidence intervals do not overlap in Figure A.1, E_t and G_{tf}. In this table, $(\bar{\bullet})$ indicates a mean value. Each test was repeated at each frequency examined in this study (10-20 kHz), ω_i. For all tests, the same results were found at all frequencies.

	Null Hypothesis	Can be rejected @ 5% significance level at any frequency ω_i?
$\bar{E}_t$	$\bar{E}_t^{WT}(\omega_i) = \bar{E}_t^{TB}(\omega_i)$	Yes
	$\bar{E}_t^{WT}(\omega_i) < \bar{E}_t^{TB}(\omega_i)$	Yes
	$\bar{E}_t^{WT}(\omega_i) > \bar{E}_t^{TB}(\omega_i)$	No
$\bar{G}_{tf}$	$\bar{G}_{tf}^{WT}(\omega_i) = \bar{G}_{tf}^{TB}(\omega_i)$	Yes
	$\bar{G}_{tf}^{WT}(\omega_i) < \bar{G}_{tf}^{TB}(\omega_i)$	Yes
	$\bar{G}_{tf}^{WT}(\omega_i) > \bar{G}_{tf}^{TB}(\omega_i)$	No

A.2 Influence of the value of E_f and fiber-direction damping on model fit

In the study discussed in Chapter 2, the values of the transversely isotropic material parameters were found by assuming that E_f was elastic. In the actual TM, some damping in the fiber direction would be present and the value of the loss tangent in the fiber direction, $\tan\delta_f$, would likely lie somewhere between 0 and $\tan\delta_t$. Introduction of the two additional free parameters needed to represent the fiber-direction stiffness using a standard linear solid (E_{f1} and η_{f1}, as in Eq. 3 in the main body of the text) would significantly increase the computational time necessary to complete the fitting process (which takes approximately two days with seven free parameters). Thus, to

ensure that our assumption regarding the viscoelasticity of the fiber direction and our algorithm's inability to precisely capture the value of E_f do not affect the values found for other parameters, all TMs were fit using three different E_f assumptions:

1. E_f is elastic (i.e. $\tan\delta_f = 0$), as in Chapter 2
2. E_f is set viscoelastic with $\tan\delta_f = \tan\delta_t$
3. E_f is elastic and fixed to a constant value (of 700kPa)

The median parameter values at 20kHz found in each case are compared in Figure A.3. The values for E_t and G_{tf} are consistent regardless of the model chosen for E_f (shown on Figures A.3A-B). As seen on Figure A.3C, when E_f is modeled as viscoelastic, for both phenotypes, the median real portion of E_f remains very similar to the median value found using an elastic model of E_f. In all cases, the TM remains significantly anisotropic ($\Gamma > 3$) and more anisotropic in $Tectb^{-/-}$ TMs than in wild-type TMs (even in the case where E_f is fixed to a value at the low end of the range of values found for the wild-type TM). While in all cases, the algorithm struggles to find the precise value of the loss tangents, $\tan\delta_t$ and $\tan\delta_s$, the effect of the E_f model appears to be negligible.

A.3 Justification for Parameter Constraints

In an effort to limit the parameter space, constraints were placed on the values of E_f, E_t, G_{tf}, $\tan\delta_t$, and $\tan\delta_s$, given in Table A.2. The parameter constraints were chosen based on previously reported values from Refs. 3, 4 and physical considerations based on a micro-mechanics model of a fiber-reinforced material. The justification for these constraints is described in more detail below.

TABLE A.2. Constraints placed on parameter values

Parameter	Lower Bound	Upper Bound	Additional Constraints
E_f	0 kPa	2000 kPa	$E_f/E_t \geq 1$
E_t	0 kPa	330 kPa	$1 \leq E_t/G_{tf} \leq 3$
G_{tf}	0 kPa	160 kPa	
$\tan\delta_t$	0	3.3	$\tan\delta_t \leq \tan\delta_s$
$\tan\delta_s$	0	3.3	

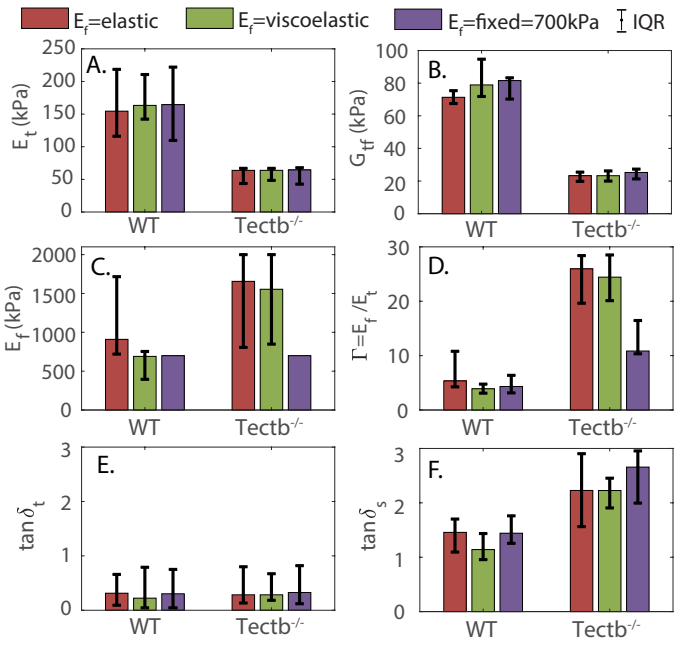

FIGURE A.3. Comparison of material properties at 20kHz found using different assumptions about E_f using a transversely isotropic constitutive model where: E_f is elastic (i.e. $tan\delta_f = 0$) (plotted in red), E_f is viscoelastic with $tan\delta_f = tan\delta_t$ (plotted in green), and where E_f is elastic and fixed to a constant value of 700kPa (plotted in purple)

A.3.1 Justification of parameter bounds

For all parameters, the lower bound was set to zero. The upper bounds for the two loss tangents were set slightly higher (20% larger) than maximum value of the loss tangent calculated from values found by Sellon et al.[3], $\tan\delta^{max} = \omega\eta^{max}/G_{tf}^{min} = 2.77$. The upper bound for G_{tf} was set as twice the highest value found for G_{tf} at 20kHz (=80 kPa by Jones et al.[4]). The upper bound of E_t was chosen arbitrarily as a value slightly higher than three times the max value found for G_{tf}: although this bound is arbitrary, no solution approached this bound. The upper bound of E_f was chosen arbitrarily as approximately ten times higher than the largest static Young's modulus value reported for a basal mouse TM (=210 kPa measured by Gueta et al.[32]): two solutions found a value of E_f at the upper bound.

A.3.2 Justification of $E_f \geq E_t$ constraint

The constraint that $E_f \geq E_t$ was motivated by the presence of collagen fibers aligned within a striated sheet matrix within the TM[35,36,21]: it was assumed that the collagen fibers are stiffer than

the matrix.

A.3.3 Justification of $3 \leq E_t/G_{tf} \leq 1$ constraint

An approximation of G_{tf} based on the micromechanics approach is given in the main body of the text in Eq. 11. Assuming that the matrix is an isotropic, incompressible material (such that $E_M = 3G_M$), we find that

$$\frac{E_t^{MM}}{G_{tf}^{MM}} = 3 \tag{5.1}$$

This value, $E_t^{MM}/G_{tf}^{MM} = 3$, was set as the upper bound of the parameter constraint. However, several assumptions of this approach render the micromechanics description of E_t and G_{tf} too simplistic. One such oversimplification is the assumption of contiguity of the matrix; i.e. all fibers are parallel and are not in contact with one another. From ultrastructural studies of the mammalian TM, it appears that the collagen fibers are not perfectly parallel, are distributed unevenly, and are sometimes in physical contact with one another[101]. Thus, to obtain a constraint between E_t and G_{tf}, an elasticity approach in which the contiguity of the fibers is considered[102,103] is used. With this approach, E_t and G_{tf} are expressed as,

$$\begin{aligned} E_t^{EA} =& 2\left(1 - \nu_{col} + (\nu_{col} - \nu_{mat})V_{mat}\right)\left[(1-C)\frac{K_{col}(2K_{mat} + G_{mat}) - G_{mat}(K_{col} - K_{mat})V_{mat}}{(2K_{mat} + G_{mat}) + 2(K_{col} - K_{mat})V_{mat}}\right. \\ &\left. + C\frac{K_{col}(2K_{mat} + G_{col}) + G_{col}(K_{mat} - K_{col})V_{mat}}{(2K_{mat} + G_{col}) - 2(K_{mat} - K_{col})V_{mat}}\right] \end{aligned} \tag{5.2}$$

and,

$$\begin{aligned} G_{tf}^{EA} =& (1-C)G_{mat}\frac{2G_{col} - (G_{col} - G_{mat})V_{mat}}{2G_{mat} + (G_{col} - G_{mat})V_{mat}} \\ &+ CG_{col}\frac{(G_{col} + G_{mat}) - (G_{col} - G_{mat})V_{mat}}{(G_{col} + G_{mat}) + (G_{col} - G_{mat})V_{mat}} \end{aligned} \tag{5.3}$$

where the superscript $(\bullet)^{EA}$ indicates a value found using the elasticity approach given in Refs.[102,103], a subscript $(\bullet)_{col}$ indicates a property of the collagen fibers, and a subscript $(\bullet)_{mat}$ indicates a property of the matrix. In the above equations, C denotes the degree of contiguity (where $C = 0$ corresponds to isolated fibers and $C = 1$ corresponds to the condition where all fibers are contact),

$K_\bullet$ indicates a bulk modulus, $\nu_\bullet$ indicates a Poisson's ratio, and k is the fiber misalignment factor. K_{mat}, K_{col}, G_{mat}, and G_{col} are written as,

$$\begin{aligned} K_{mat} &= \frac{E_{mat}}{2(1-\nu_{mat})} \\ K_{col} &= \frac{E_{col}}{2(1-\nu_{col})} \\ G_{mat} &= \frac{E_{mat}}{2(1+\nu_{mat})} \\ G_{col} &= \frac{E_{col}}{2(1+\nu_{col})} \end{aligned} \tag{5.4}$$

To find the upper and lower bounds of the ratio between E_t and G_{tf}, E_{col} was set to the upper bound of the Young's modulus measured for single collagen fibril, $E_{col} = 0.8$ GPa[57]. E_{mat} was set to $E_{mat} = 3G_{tf} = 140$kPa where the value for G_{tf} was taken from from Ref.[3]. The matrix itself was assumed to be incompressible, $\nu_{mat} = 0.5$, and ν_{col} was set arbitrarily to 0.33 (as the Poisson's ratio of collagen is unknown[58]). With these values and assumptions, V_{col} is varied between 0.05% and 2%. The results for E_t^{EA}/G_{tf}^{EA} are plotted on Figure A.4. Even quite low levels of contiguity ($C < 0.2$), E_t/G_{tf} can vary from approximately 1 to 3; thus, E_t/G_{tf} was constrained from 1 to 3 in our models.

A.3.4 Justification of $\tan\delta_t \leq \tan\delta_s$ constraint

Using a micromechanics model of a unidirectional fiber-reinforced matrix where the fiber material is assumed to be much stiffer than the matrix and where the volume fraction of the fibers is much smaller than that of the matrix, as in Eq. 11 in main body of text, it can be seen that the properties of the shear modulus and transverse Young's modulus depend primarily on the values of the Young's modulus of the matrix. If the matrix of the material is modeled as an isotropic, homogeneous, linear solid viscoelastic material, previous studies have shown that the loss component of the bulk modulus is significantly higher than that of the shear modulus[104]; i.e., isotropic, viscoelastic materials tend to be more lossy due to deformation in shear than in compression. Thus, the parameter space was limited by setting the loss tangent in the transverse direction smaller than that in shear, $\tan\delta_t \leq \tan\delta_s$.

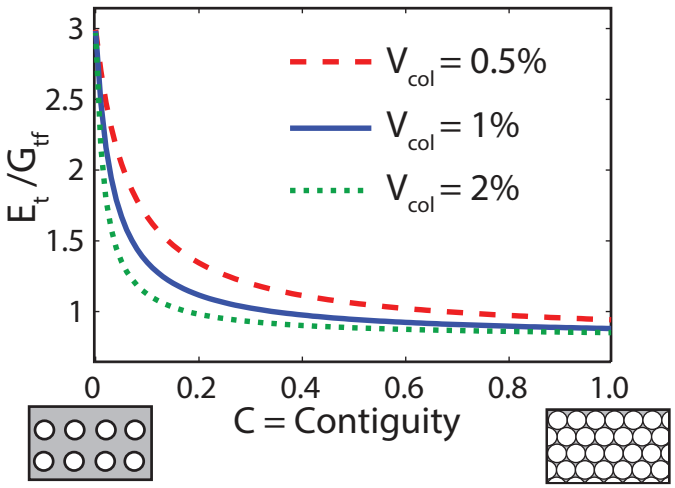

FIGURE A.4. Exploration of effect of the assumption of contiguity of the matrix on the ratio between E_t and E_f. The degree of contiguity of the matrix is varied from 0 (where the fibers do not make physical contact with one another) to 1 (where the fibers are perfectly contiguous). To test this assumption, $E_{col} = 0.8$ GPa, $E_{mat} = 140$kPa, $\nu_{mat} = 0.5$, and $\nu_{col} = 0.33$: the volume fraction of the collagen fibers is varied from 0.5%-2%. As seen here, even quite low levels of contiguity ($C < 0.2$), E_t/G_{tf} can vary from approximately 1 to 3.

Appendix B: Middle-ear mechanics supplemental information

B.1 Derivation of two-port transmission matrix parameters in terms of lumped parameter impedances

In Eq. (3.1), the two-port transmission matrix parameters, A, B, C, and D, relate the pressure and volume velocity in the ear canal at the TM to the pressure and volume velocity at the stapes footplate. Similarly, in Eq. (3.6), the transformed two-port transmission matrix parameters, A_T, B_T, C_T, and D_T relate the pressure and volume velocity in the ear canal at the TM to the transformed effective pressure and volume velocity at the stapes footplate. The equations for the transformed pressure and volume velocity at the stapes footplate are given in Figure B.1. Thus, the difference between the two-port transmission matrix parameters in Eq. (3.1) and Eq. (3.6) is simply scaling in order to remove the effects of the geometry of the ear.

In order to express Eq. (3.6) in terms of the lumped parameter matrix elements, the forces and velocities in the lumped parameter model seen in Figure B.1A are converted to transformed pressures and volume velocities, seen in Figure B.1B; Kirchoff's current and voltage laws are employed to find:

$$\begin{aligned} P_{ed} &= (Z_{MEC} + Z_{mT} + Z_{isjT})U_{tm} - Z_{isjT}U_{sT} \\ P_{sT} &= Z_{isjT}U_{tm} - (Z_{sT} + Z_{isjT})U_{sT} \end{aligned} \tag{5.5}$$

Rearranging it is found that

$$U_{tm} = \frac{P_{sT}}{Z_{isjT}} + \frac{Z_{sT} + Z_{isjT}}{Z_{isjT}}U_{sT} \tag{5.6}$$

Such that,

$$P_{ed} = \left[\frac{Z_{mT} + Z_{MEC}}{Z_{isjT}} + 1\right] P_{sT} + \left[\frac{(Z_{MEC} + Z_{mT})Z_{sT}}{Z_{isjT}} + Z_{mT} + Z_{MEC} + Z_{sT}\right] U_{sT} \tag{5.7}$$

Eqs. (5.6) and (5.7) can be directly equated to Eq. (3.6) in order to find expressions for A_T, B_T, C_T, and D_T given in Eq. (3.7).

A. Original Circuit Diagram

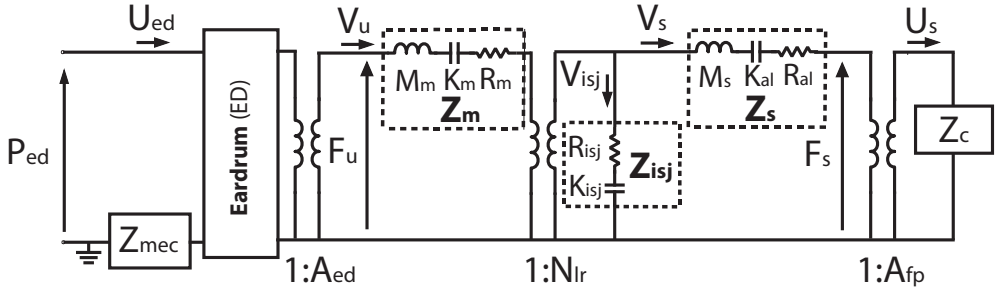

B. Equivalent "Transformed" Circuit Diagram with Redefined Variables

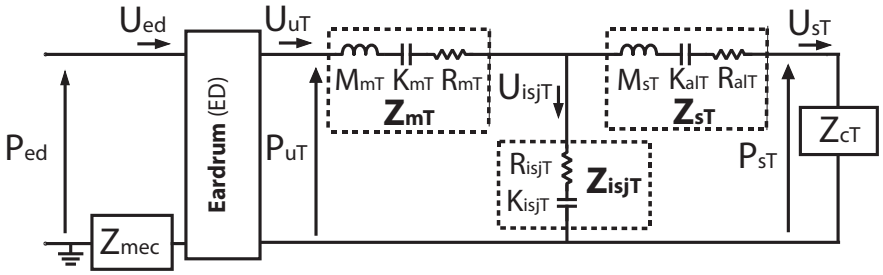

Relationships between transformed and untransformed values:

$$P_{uT} = F_u / A_{ed} \qquad P_{sT} = P_s A_{fp} / (A_{ed} N_{lr})$$

$$U_{uT} = V_u A_{ed} \qquad U_{isjT} = V_{isj} A_{ed} N_{lr} \qquad U_{sT} = U_s A_{ed} N_{lr} / A_{fp}$$

$$Z_{mT} = Z_m / A_{ed}^2 \qquad Z_{isjT} = Z_{isj} / (A_{ed} N_{lr})^2 \qquad Z_{sT} = Z_s / (A_{ed} N_{lr})^2 \qquad Z_{cT} = Z_c A_{fp}^2 / (A_{ed} N_{lr})^2$$

FIGURE B.1. Original and "transformed" middle-ear models used in model comparison. A. The original middle-ear circuit model, as seen in Figures 3.3 and 3.4 (the model variables are defined in the captions of these figures). B. An alternate version of the circuit model where the transformers have been "removed" from the model such that all variables are represented by their acoustic equivalents as seen from the left of the three transformers, as was done by O'Connor and Puria in a circuit model of the human middle ear[18]. Transformed variables are noted with a "T" appended to their subscripts: the relationships between the transformed and untransformed versions of the variables are given below subfigure (B). As mentioned by O'Connor and Puria[18], by redefining model variables in this manner, it is possible to make quantitative comparisons between variables that were previously on opposite sides of the transformers.

B.2 Guinea pig model with transmission line model of the TM

In Section Chapter 3, the guinea pig model published in Ref. 1 was coupled with the transmission line model of the TM outlined in Section 3.3. After inserting the TL model, parameters were adjusted in order to best match the group delay at high frequencies and to reduce peaks in G_{MEf}. The parameters used for the comparison are listed in Table B.1.

TABLE B.1. Guinea pig model parameter values from the Meaud and Lemons noTL model[1] and the adjusted parameters for the TL model used in the interspecies comparison. Ossicular chain and middle ear cavity model parameters are defined identically to those given in Figure 3.4. T_{ed} and Z_{ed} are the TM delay and characteristic impedance, respectively. All parameter values are in MKS mechanical units (kg for mass parameters, N/m for stiffness parameters, and $N-s/m$ for damping parameters) unless noted with an "a" in the superscript in which case the parameter values are in MKS acoustical units (s for the delay parameter, kg/m^4 for the mass parameters, N/m^5 for the stiffness parameters, and $N-s/m^5$ for damping and impedance parameters).

Parameter	**NoTL model values**[1]	**Adjusted TL model values**
M_m	6.0×10^{-7}	1.6×10^{-7}
K_m	30	50
R_m	0.0004	0.02
K_{isj}	340	2.8×10^{3}
R_{isj}	0.03	3.0×10^{-4}
M_s	1.5×10^{-7}	6.0×10^{-7}
K_{al}	5	200
R_{al}	0.016	0.016
T^a_{ed}	–	1.45×10^{-5}
Z^a_{ed}	–	1.15×10^{-8}
N_{lr}	2	1.75

Appendix C: Bullfrog eardrum mechanics supplemental information

C.1 Discretization of differential equation

Eq. 4.3 can be expressed as

$$A(r)\zeta'' + B(r)\zeta' + C(r)\zeta = g(r) \tag{5.8}$$

where

$$\begin{aligned} A(r) &= r \\ B(r) &= 1 \\ C(r) &= \frac{r\omega^2\rho_m(r)}{T_m^*} \\ g(r) &= \frac{-Pr}{T_m^*} \end{aligned} \tag{5.9}$$

Discretizing r into n points and using central difference approximations for ζ'' and ζ',

$$\begin{aligned} r_i &= ih, i = 0, 1, ...n \\ h &= \frac{R}{n} \\ \zeta_i &= \zeta(r_i) \\ A_i &= A(r_i) \\ B_i &= B(r_i) \\ C_i &= C(r_i) \\ g_i &= g(r_i) \\ \zeta'' &= \frac{\zeta_{i+1} - 2\zeta_i + \zeta_{i-1}}{h^2} \\ \zeta' &= \frac{\zeta_{i+1} - \zeta_{i-1}}{2h} \end{aligned} \tag{5.10}$$

And simplifying (as in Ref. 105), it is found that,

$$\left(A_i + \frac{1}{2}hB_i\right)\zeta_{i+1} + \left(-2A_i + h^2C_i\right)\zeta_i + \left(A_i - \frac{1}{2}hB_i\right)\zeta_{i-1} = h^2 g_i \tag{5.11}$$

Looping through $i = 1, 2, ...n-1$ a row in a sparse matrix, A, is found:

$$[\mathcal{A}]\{\zeta\} = h^2\{g\} \tag{5.12}$$

Where the components of A are found easily using Eq. 5.11, except for at the boundaries, where the process is outlined below. Setting the slope at $r = 0$ equal to zero, it is found that at $i = 0$:

$$\zeta_{i-1} = \zeta_{i+1} \tag{5.13}$$

In order for the membrane to be continuously differentiable at $r = 0$, $\zeta_0 = \zeta_1 = \zeta_{-1}$. Thus, for the first row, $(i = 1)$,

$$\begin{aligned} \mathcal{A}_{0,1} &= A_i + \frac{1}{2}hB_i \\ \mathcal{A}_{0,0} &= -A_i - \frac{1}{2}hB_i + h^2C_i \end{aligned} \tag{5.14}$$

For the last row $(i = n-1)$:

$$\zeta_{i+1} = 0 \tag{5.15}$$

So that,

$$\begin{aligned} \mathcal{A}_{n-1,n-1} &= -2A_i + h^2C_i \\ \mathcal{A}_{n-1,n-2} &= A_i - \frac{1}{2}hB_i \end{aligned} \tag{5.16}$$

C.2 Constraints placed on bullfrog parameters

The upper and lower bounds placed on the bullfrog model parameters in the inverse fitting algorithm are given in Table C.1.

TABLE C.1. Lower and upper bounds placed on bullfrog eardrum model.

Parameter	Lower Bound (LB)	Upper Bound (UB)	Justification
$\gamma = \tau_0/\tau_R$	0.1	1	LB is arbitrary, UB = uniform
T_0	0	100	Trial & error
$\tan\delta_{min}$	0.05	$\omega_{min}/\omega_{max} = 1$	UB set such that $\max(\tan\delta(\omega)) = 1$

C.3 Best fit for each combination of thickness and damping models

In this section, the resulting best fit for each model combination described in Figure 4.3 is given in Figure C.1. The error for each model combination is given on Figure 4.4: the lowest error is found by using spatially-dependent thickness and Kelvin-Voigt material (Model 2C). As seen in Figures 4.4 and C.1, the worst error for both thickness models is found by using a Maxwell material: the damping must be significant at low frequencies or large peaks appear in the magnitude which are not seen in the experimental data. Models 1A and 1C capture the magnitude and phase of the center point fairly well, but struggle to capture the response at the edge of the membrane. Model 2A captures the phase of all three points fairly well, but does not capture the peaks and troughs seen in the magnitude of the response at each point: the loss tangent for this model is constant across the frequency range and thus, must be large to avoid large peaks within the magnitude, as in Models 1B and 2B. This large loss tangent value would then cause the model to struggle to capture the small peaks and troughs at high frequencies. In Model 2C, the response captures both the small peaks and troughs seen in the center point magnitude and the phase of the response of all three points. While the model struggles to precisely capture the magnitude at $r = 1.2$mm and $r = 2.3$mm, it does a very good job at capturing qualitative features we seek to reproduce: specifically, the broadband nature of the eardrum and the long group delay through the ear.

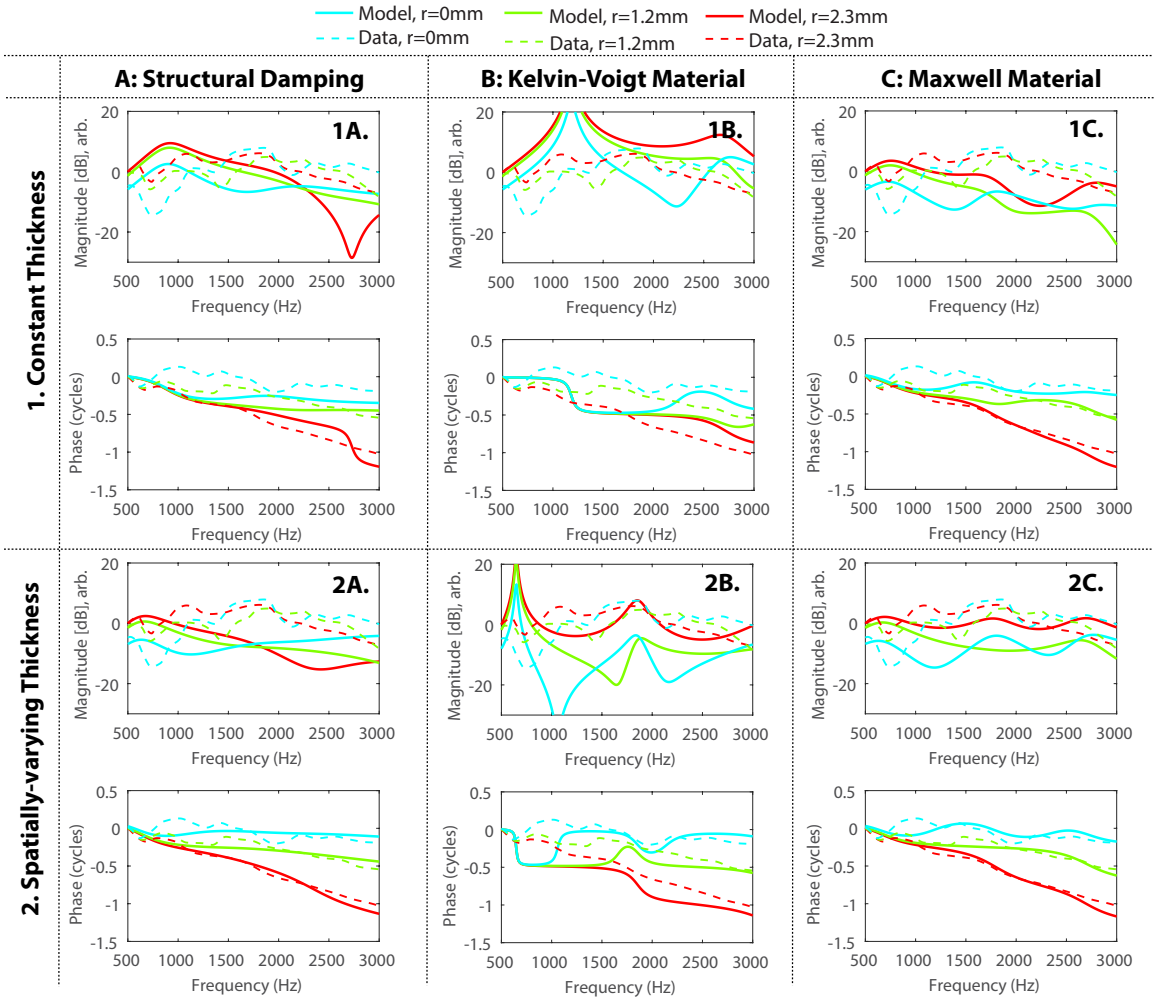

FIGURE C.1. The best fit found by minimizing model parameters using fitting algorithm described in Chapter 4 Section 4.3.3. Each model combination is described in Figure 4.3. The error for each model combination is given in Figure 4.4.

References

[1] J. Meaud and C. Lemons, "Nonlinear response to a click in a time-domain model of the mammalian ear," *J. Acoust. Soc. Am.*, 2015.

[2] P. la Cour III., *Tidents naturaere (Nature of time).* Fr. Bagges Bogtrykkeri, 1903.

[3] J. Sellon, R. Ghaffari, S. Farrahi, G. Richardson, and D. Freeman, "Porosity controls spread of excitation in tectorial membrane traveling waves," *Biophysical journal*, vol. 106, no. 6, pp. 1406–1413, 2014.

[4] G. Jones, S. Elliott, I. Russell, and A. Lukashkin, "Modified protein expression in the tectorial membrane of the cochlea reveals roles for the striated sheet matrix," *Biophysical journal*, vol. 108, no. 1, pp. 203–210, 2015.

[5] J. A. Buytaert, W. H. Salih, M. Dierick, P. Jacobs, and J. J. Dirckx, "Realistic 3d computer model of the gerbil middle ear, featuring accurate morphology of bone and soft tissue structures," *Journal of the Association for Research in Otolaryngology*, vol. 12, no. 6, pp. 681–696, 2011.

[6] J. E. Songer and J. J. Rosowski, "The effect of superior-canal opening on middle-ear input admittance and air-conducted stapes velocity in chinchilla," *The Journal of the Acoustical Society of America*, vol. 120, no. 1, pp. 258–269, 2006.

[7] J. J. Rosowski, M. E. Ravicz, and J. E. Songer, "Structures that contribute to middle-ear admittance in chinchilla," *Journal of Comparative Physiology A*, vol. 192, no. 12, pp. 1287–1311, 2006.

[8] S. Puria and J. B. Allen, "Measurements and model of the cat middle ear: Evidence of tympanic membrane acoustic delay," *The Journal of the Acoustical Society of America*, vol. 104, no. 6, pp. 3463–3481, 1998.

[9] M. C. Slama, M. E. Ravicz, and J. J. Rosowski, "Middle ear function and cochlear input impedance in chinchilla," *The Journal of the Acoustical Society of America*, vol. 127, no. 3, pp. 1397–1410, 2010.

[10] J. E. Songer and J. J. Rosowski, "Transmission matrix analysis of the chinchilla middle ear," *The Journal of the Acoustical Society of America*, vol. 122, no. 2, pp. 932–942, 2007.

[11] L. Décory, R. B. Franke, and A. L. Dancer, "Measurement of the middle ear transfer function in cat, chinchilla and guinea pig," in *The Mechanics and Biophysics of Hearing*, pp. 270–277, Springer, 1990.

[12] D. Chhan, C. Röösli, M. L. McKinnon, and J. J. Rosowski, "Evidence of inner ear contribution in bone conduction in chinchilla," *Hearing research*, vol. 301, pp. 66–71, 2013.

[13] D. Chhan, P. Bowers, M. L. McKinnon, and J. J. Rosowski, "Middle-ear and inner-ear contribution to bone conduction in chinchilla: The development of carhart's notch," *Hearing research*, 2016.

[14] M. E. Ravicz and J. J. Rosowski, "Inner-ear sound pressures near the base of the cochlea in chinchilla: further investigation," *The Journal of the Acoustical Society of America*, vol. 133, no. 4, pp. 2208–2223, 2013.

[15] S. E. Voss and C. A. Shera, "Simultaneous measurement of middle-ear input impedance and forward/reverse transmission in cat," *The Journal of the Acoustical Society of America*, vol. 116, no. 4, pp. 2187–2198, 2004.

[16] S. Puria, "Middle-ear two-port measurements in human cadaveric temporal bones: comparison with models," in *Proceedings of the 3rd Symposium on Middle Ear Mechanics in Research and Otology*, pp. 43–50, World Scientific, 2003.

[17] Y. Werner, J. Pylka, H. Schneider, M. Seifan, W. Walkowiak, and U. Werner-Reiss, "Function of the sexually dimorphic ear of the american bullfrog, rana catesbeiana: brief review and new insight," *Journal of Experimental Biology*, vol. 212, no. 14, pp. 2204–2214, 2009.

[18] K. N. O'Connor and S. Puria, "Middle-ear circuit model parameters based on a population of human ears," *The Journal of the Acoustical Society of America*, vol. 123, no. 1, pp. 197–211, 2008.

[19] L. Kinsler and A. Frey, *Fundamentals of Acoustics*. J. Wiley & Sons, 4 ed., 2000.

[20] P. K. Legan, V. A. Lukashkina, R. J. Goodyear, A. N. Lukashkin, K. Verhoeven, G. Van Camp, I. J. Russell, and G. P. Richardson, "A deafness mutation isolates a second role for the tectorial membrane in hearing," *Nat. Neurosci.*, vol. 8, pp. 1035–1042, August 2005.

[21] I. Russell, P. Legan, V. Lukashkina, A. Lukashkin, R. Goodyear, and G. Richardson, "Sharpened cochlear tuning in a mouse with a genetically modified tectorial membrane," *Nature neuroscience*, vol. 10, no. 2, p. 215, 2007.

[22] P. Van Dijk, M. J. Mason, R. L. Schoffelen, P. M. Narins, and S. W. Meenderink, "Mechanics of the frog ear," *Hearing research*, vol. 273, no. 1-2, pp. 46–58, 2011.

[23] C. Bergevin, S. W. Meenderink, M. Van Der Heijden, and P. M. Narins, "Slow dynamics of the amphibian tympanic membrane," in *AIP Conference Proceedings*, vol. 1703, p. 060001, AIP Publishing, 2015.

[24] G. von Bekesy, *Experiments in Hearing*. New York: McGraw–Hill, 1960.

[25] A. Hudspeth, "The cellular basis of hearing: the biophysics of hair cells," *Science*, vol. 230, pp. 745–752, 1985.

[26] P. K. Legan, V. A. Lukashkina, R. J. Goodyear, M. Kossl, I. J. Russell, and G. P. Richardson,

"A targeted deletion in alpha-tectorin reveals that the tectorial membrane is required for the gain and timing of cochlear feedback," *Neuron*, vol. 28, no. 1, pp. 273–285, 2000.

[27] M. Cheatham, R. Goodyear, K. Homma, P. Legan, J. Korchagina, S. Naskar, J. Siegel, P. Dallos, J. Zheng, and G. Richardson, "Loss of the tectorial membrane protein ceacam16 enhances spontaneous, stimulus-frequency, and transiently evoked otoacoustic emissions," *Journal of Neuroscience*, vol. 34, no. 31, pp. 10325–10338, 2014.

[28] M. Cheatham, A. Ahmad, A. Dallos, and G. Richardson, "$tecta^{Y1870C/+}$ with alterations in the strucure and porosity of the tectorial membrane display large numbers of spontaneous emissions.," in *To the Ear and Back Again-Advances in Auditory Biophysics Proceedings of the 13th Mechanics of Hearing Workshop*, p. 1965:040001, AIP, 2017.

[29] H. Lee, P. Raphael, J. Park, A. Ellerbee, B. Applegate, and J. Oghalai, "Noninvasive in vivo imaging reveals differences between tectorial membrane and basilar membrane traveling waves in the mouse cochlea," *Proceedings of the National Academy of Sciences*, p. 201500038, 2015.

[30] A. W. Monreal, B. M. Ferguson, D. J. Headon, S. L. Street, P. A. Overbeek, and J. Zonana, "Mutations in the human homologue of mouse dl cause autosomal recessive and dominant hypohidrotic ectodermal dysplasia," *Nature genetics*, vol. 22, no. 4, p. 366, 1999.

[31] B. Shoelson, E. Dimitriadis, H. Cai, B. Kachar, and R. Chadwick, "Evidence and implications of inhomogeneity in tectorial membrane elasticity," *Biophysical journal*, vol. 87, no. 4, pp. 2768–2777, 2004.

[32] R. Gueta, D. Barlam, R. Shneck, and I. Rousso, "Measurement of the mechanical properties of isolated tectorial membrane using atomic force microscopy," *Proceedings of the National Academy of Sciences*, vol. 103, no. 40, pp. 14790–14795, 2006.

[33] C. Richter, G. Emadi, G. Getnick, A. Quesnel, and P. Dallos, "Tectorial membrane stiffness gradients," *Biophysical journal*, vol. 93, no. 6, pp. 2265–2276, 2007.

[34] R. Gueta, E. Tal, Y. Silberberg, and I. Rousso, "The 3d structure of the tectorial membrane determined by second-harmonic imaging microscopy," *Journal of structural biology*, vol. 159, no. 1, pp. 103–110, 2007.

[35] J. Hasko and G. Richardson, "The ultrastructural organization and properties of the mouse tectorial membrane matrix," *Hearing research*, vol. 35, no. 1, pp. 21–38, 1988.

[36] A. Kronester-Frei, "Ultrastructure of the different zones of the tectorial membrane," *Cell and tissue research*, vol. 193, no. 1, pp. 11–23, 1978.

[37] K. Masaki, J. Gu, R. Ghaffari, G. Chan, R. Smith, D. Freeman, and A. Aranyosi, "Col11a2 deletion reveals the molecular basis for tectorial membrane mechanical anisotropy," *Biophysical journal*, vol. 96, no. 11, pp. 4717–4724, 2009.

[38] N. Gavara and R. Chadwick, "Collagen-based mechanical anisotropy of the tectorial membrane: implications for inter-row coupling of outer hair cell bundles," *PLoS One*, vol. 4, no. 3, p. e4877, 2009.

[39] J. Zwislocki and L. Cefaratti, "Tectorial membrane ii: Stiffness measurements in vivo," *Hearing research*, vol. 42, no. 2-3, pp. 211–227, 1989.

[40] J. Gu, W. Hemmert, D. Freeman, and A. Aranyosi, "Frequency-dependent shear impedance of the tectorial membrane," *Biophysical journal*, vol. 95, no. 5, pp. 2529–2538, 2008.

[41] R. Gueta, D. Barlam, R. Shneck, and I. Rousso, "Sound-evoked deflections of outer hair cell stereocilia arise from tectorial membrane anisotropy," *Biophysical journal*, vol. 94, no. 11, pp. 4570–4576, 2008.

[42] G. Jones, V. Lukashkina, I. Russell, S. Elliott, and A. Lukashkin, "Frequency-dependent properties of the tectorial membrane facilitate energy transmission and amplification in the cochlea," *Biophysical journal*, vol. 104, no. 6, pp. 1357–1366, 2013.

[43] R. Ghaffari, A. Aranyosi, and D. Freeman, "Longitudinally propagating traveling waves of the mammalian tectorial membrane," *Proceedings of the National Academy of Sciences*, vol. 104, no. 42, pp. 16510–16515, 2007.

[44] J. Meaud and K. Grosh, "The effect of tectorial membrane and basilar membrane longitudinal coupling in cochlear mechanics," *The Journal of the Acoustical Society of America*, vol. 127, no. 3, pp. 1411–1421, 2010.

[45] D. Shah, D. Freeman, and T. Weiss, "The osmotic response of the isolated, unfixed mouse tectorial membrane to isosmotic solutions: effect of na+, k+, and ca2+ concentration," *Hearing research*, vol. 87, no. 1-2, pp. 187–207, 1995.

[46] C. Lemons, J. Sellon, E. Boatti, D. Filizzola, D. Freeman, and J. Meaud, "Anisotropic material properties of wild-type and tectb-/- tectorial membranes (under review)," *Biophysical Journal*, vol. TBD, no. TBD, p. TBD, 2018.

[47] D. Systèmes, "Abaqus/standard user's manual, version 6.14," *Abaqus/Standard*, 2014.

[48] S. Farrahi, R. Ghaffari, J. Sellon, H. Nakajima, and D. Freeman, "Cochlear tuning... of mice and men," in *To the Ear and Back Again-Advances in Auditory Biophysics Proceedings of the 13th Mechanics of Hearing Workshop*, p. 1965:040003, AIP, 2017.

[49] R. Lakes and R. Lakes, *Viscoelastic materials*. Cambridge University Press, 2009.

[50] R. Hooke and T. Jeeves, ""direct search" solution of numerical and statistical problems," *Journal of the ACM*, vol. 8, no. 2, pp. 212–229, 1961.

[51] S. Farrahi, R. Ghaffari, J. B. Sellon, H. H. Nakajima, and D. M. Freeman, "Tectorial membrane traveling waves underlie sharp auditory tuning in humans," *Biophysical journal*, vol. 111, no. 5, pp. 921–924, 2016.

[52] S. Farrahi, *Human tectorial membrane waves*. PhD thesis, Massachusetts Institute of Technology, 2013.

[53] N. Cooper, A. Vavakou, and M. van der Heijden, "Vibration hotspots reveal longitudinal funneling of sound-evoked motion in the mammalian cochlea," *Nature communications*, vol. 9, no. 1,

p. 3054, 2018.

[54] W. Hemmert, H. P. Zenner, and A. W. Gummer, "Three-dimensional motion of the organ of corti," *Biophys. J.*, vol. 78, no. 5, pp. 2285–2297, 2000.

[55] I. Teudt and C. Richter, "Basilar membrane and tectorial membrane stiffness in the cba/caj mouse," *Journal of the Association for Research in Otolaryngology*, pp. 1–20, 2014.

[56] J. Reddy, *Mechanics of Laminated Composite Plates and Shells: Theory and Analysis*. CRC Press, 2004.

[57] J. van der Rijt, K. van der Werf, M. Bennink, P. Dijkstra, and J. Feijen, "Micromechanical testing of individual collagen fibrils," *Macromolecular Bioscience*, vol. 6, no. 9, pp. 697–702, 2006.

[58] M. Wenger, L. Bozec, M. Horton, and P. Mesquida, "Mechanical properties of collagen fibrils," *Biophysical Journal*, vol. 93, no. 4, pp. 1255–1263, 2007.

[59] A. Hudspeth, "Extracellular current flow and the site of transduction by vertebrate hair cells," *Journal of Neuroscience*, vol. 2, no. 1, pp. 1–10, 1982.

[60] X. Wang and R. Z. Gan, "3d finite element model of the chinchilla ear for characterizing middle ear functions," *Biomechanics and modeling in mechanobiology*, pp. 1–15, 2016.

[61] C. Lemons and J. Meaud, "Middle-ear function in the chinchilla: Circuit models and comparison with other mammalian species," *The Journal of the Acoustical Society of America*, vol. 140, no. 4, pp. 2735–2753, 2016.

[62] D. Kemp, *Otoacoustic Emissions: Concepts and Origins.*, ch. 1, pp. 1–38. Springer Science and Business Media, 2008.

[63] N. M. W.R.J. Funnell and W. Decraemer, *Modeling of Middle Ear Mechanics*, ch. 7, pp. 171–210. Springer Handbook of Auditory Research, Springer Science & Business Media, 2013.

[64] S. Puria and C. Steele, "Tympanic-membrane and malleus–incus-complex co-adaptations for high-frequency hearing in mammals," *Hearing research*, vol. 263, no. 1, pp. 183–190, 2010.

[65] J. J. Rosowski, J. T. Cheng, M. E. Ravicz, N. Hulli, M. Hernandez-Montes, E. Harrington, and C. Furlong, "Computer-assisted time-averaged holograms of the motion of the surface of the mammalian tympanic membrane with sound stimuli of 0.4–25khz," *Hearing research*, vol. 253, no. 1, pp. 83–96, 2009.

[66] J. T. Cheng, M. Hamade, S. N. Merchant, J. J. Rosowski, E. Harrington, and C. Furlong, "Wave motion on the surface of the human tympanic membrane: holographic measurement and modeling analysis," *The Journal of the Acoustical Society of America*, vol. 133, no. 2, pp. 918–937, 2013.

[67] Y. W. Liu and S. T. Neely, "Distortion product emissions from a cochlear model with nonlinear mechanoelectrical transduction in outer hair cells," *The Journal of the Acoustical Society of America*, vol. 127, no. 4, pp. 2420–2432, 2010.

[68] P. A. Vrettakos, S. P. Dear, and J. C. Saunders, "Middle ear structure in the chinchilla: a quantitative study," *American journal of otolaryngology*, vol. 9, no. 2, pp. 58–67, 1988.

[69] R. S. Heffner and H. E. Heffner, "Behavioral hearing range of the chinchilla," *Hearing research*, vol. 52, no. 1, pp. 13–16, 1991.

[70] S. Nummela, "Scaling of the mammalian middle ear," *Hearing research*, vol. 85, no. 1, pp. 18–30, 1995.

[71] M. E. Ravicz, M. C. Slama, and J. J. Rosowski, "Middle-ear pressure gain and cochlear partition differential pressure in chinchilla," *Hearing research*, vol. 263, no. 1, pp. 16–25, 2010.

[72] S. Puria, "Measurements of human middle ear forward and reverse acoustics: Implications for otoacoustic emissions," *The Journal of the Acoustical Society of America*, vol. 113, no. 5, pp. 2773–2789, 2003.

[73] C. A. Shera and G. Zweig, "Middle-ear phenomenology: The view from the three windows," *The Journal of the Acoustical Society of America*, vol. 92, no. 3, pp. 1356–1370, 1992.

[74] J. Roswoski, *Outer and Middle Ears*, ch. 6, pp. 172–247. Springer-Ver, 1994.

[75] W. Decraemer, O. de La Rochefoucauld, W. Dong, S. Khanna, J. Dirckx, and E. Olson, "Scala vestibuli pressure and three-dimensional stapes velocity measured in direct succession in gerbil," *The Journal of the Acoustical Society of America*, vol. 121, no. 5, pp. 2774–2791, 2007.

[76] M. Mason, "Middle ear structures in fossorial mammals: a comparison with non-fossorial species," *Journal of Zoology*, vol. 255, no. 4, pp. 467–486, 2001.

[77] S. Dear, *Impedance and sound transmission in the auditory periphery of the chinchilla.* PhD thesis, University of Pennsylvania, 1987.

[78] M. Ruggero, N. Rich, L. Robles, and B. Shivapuja, "Middle ear response in the chinchilla and its relationship to mechanics at the base of the cochlea," *Journal of the Acoustical Society of America*, vol. 87, no. 4, pp. 1612–1629, 1990.

[79] G. A. Manley and B. M. Johnstone, "Middle-ear function in the guinea pig," *The Journal of the Acoustical Society of America*, vol. 56, no. 2, pp. 571–576, 1974.

[80] S. Amin and A. S. Tucker, "Joint formation in the middle ear: lessons from the mouse and guinea pig," *Developmental dynamics*, vol. 235, no. 5, pp. 1326–1333, 2006.

[81] S. M. Khanna and J. Tonndorf, "Tympanic membrane vibrations in cats studied by time-averaged holography," *The Journal of the Acoustical Society of America*, vol. 51, no. 6B, pp. 1904–1920, 1972.

[82] J. Guinan Jr and W. Peake, "Middle-ear characteristics of anesthetized cats," *The Journal of the Acoustical Society of America*, vol. 41, no. 5, pp. 1237–1261, 1967.

[83] A. H. U.B. Willi, M.A. Ferrazzini, "Experimental ossicular fixations and the middle ear's response to sound: Evidence for a flexible ossicular chain," *Hearing Research*, vol. 204, pp. 60–779,

2005.

[84] H. Nakajima, M. Ravicz, S. Merchant, W. Peake, and J. Rosowski, "The incudo-malleolar joint and sound transmission losses," *Hearing Research*, vol. 174, pp. 32–44, 2005.

[85] E. Olson, "Observing middle and inner ear mechanics with novel intracochlear pressure sensors," *The Journal of the Acoustical Society of America*, vol. 103, pp. 3445–3463, 1998.

[86] O. de La Rochefoucauld, P. Kachroo, and E. S. Olson, "Ossicular motion related to middle ear transmission delay in gerbil," *Hearing research*, vol. 270, no. 1, pp. 158–172, 2010.

[87] E. G. Wever and M. Lawrence, *Physiological acoustics.* Princeton University Press, 1954.

[88] S.-H. Chung, A. Pettigrew, and M. Anson, "Hearing in the frog: dynamics of the middle ear," *Proc. R. Soc. Lond. B*, vol. 212, no. 1189, pp. 459–485, 1981.

[89] A. Purgue, "Tympanic sound radiation in the bullfrog rana catesbeiana," *Journal of Comparative Physiology A*, vol. 181, no. 5, pp. 438–445, 1997.

[90] P. M. Narins, A. S. Feng, and R. R. Fay, *Hearing and sound communication in amphibians*, vol. 28. Springer Science & Business Media, 2006.

[91] P. Morse, *Vibration and Sound.* Acoustical Society of America through AIP, 1981.

[92] T. Samejima and R. Fukuda, "Vibration analysis of a musical drum head under nonuniform density and tension using a spectral method," *Acoust. Sci. & Tech.*, vol. 37, no. 6, pp. 295–302, 2016.

[93] J. Snowdon, "Forced vibration of damped circular and annular membranes," *Transactions of the Society of Rheology*, vol. 15, no. 4, pp. 685–707, 1971.

[94] L. Meirovitch, *Fundamentals of vibrations.* Waveland Press, 2010.

[95] S. S. Horowitz, A. M. Simmons, and D. R. Ketten, "Optical and tomographic imaging of a middle ear malformation in the bullfrog (rana catesbeiana)," *The Journal of the Acoustical Society of America*, vol. 118, no. 2, pp. 1166–1171, 2005.

[96] L. C. Kuypers, W. F. Decraemer, and J. J. Dirckx, "Thickness distribution of fresh and preserved human eardrums measured with confocal microscopy," *Otology & Neurotology*, vol. 27, no. 2, pp. 256–264, 2006.

[97] J. P. Fay, S. Puria, and C. R. Steele, "The discordant eardrum," *Proceedings of the National Academy of Sciences*, vol. 103, no. 52, pp. 19743–19748, 2006.

[98] T. Bowling and J. Meaud, "Forward and reverse waves: Modeling distortion products in the intracochlear fluid pressure," *Biophysical journal*, vol. 114, no. 3, pp. 747–757, 2018.

[99] J. Cormack, Y. Liu, J.-H. Nam, and S. M. Gracewski, "Two-compartment passive frequency domain cochlea model allowing independent fluid coupling to the tectorial and basilar membranes," *The Journal of the Acoustical Society of America*, vol. 137, no. 3, pp. 1117–1125, 2015.

[100] S. J. Elliott, E. M. Ku, and B. Lineton, "A state space model for cochlear mechanics," *The Journal of the Acoustical Society of America*, vol. 122, no. 5, pp. 2759–2771, 2007.

[101] V. Tsuprun and P. Santi, "Ultrastructural organization of proteoglycans and fibrillar matrix of the tectorial membrane," *Hearing research*, vol. 110, no. 1-2, pp. 107–118, 1997.

[102] S. Tsai, "Structural behavior of composite materials," tech. rep., Philco Corp Newport Beach CA Space and Re-Entry Systems, 1964.

[103] R. Jones, *Mechanics of Composite Materials*. Taylor and Francis, Inc., 1998.

[104] T. Pritz, "Relation of bulk to shear loss factor of solid viscoelastic materials," *Journal of sound and vibration*, vol. 324, pp. 514—-519, 2009.

[105] D. Zill and W. Wright, *Advanced Engineering Mathematics, 4e*. Jones and Bartlett Publishers, 2011.